

# High Speed Deformation and Break-Up of Shaped Charge Jets.

**B S Welsh. BEng.(Hons)**

Thesis submitted to the University of Nottingham  
for the degree of Doctor of Philosophy.

August 1993



## IMAGING SERVICES NORTH

Boston Spa, Wetherby

West Yorkshire, LS23 7BQ

[www.bl.uk](http://www.bl.uk)

CONTAINS  
PULLOUTS

## Abstract

Jets resulting from shaped charges which contain metal liners are able to penetrate hard or armoured targets. Their penetration performance is related to the density of the jet and target material and also the length to which the jet can elongate. Models that describe the processes involved have generally assumed hydrodynamic fluid flow and as such have been very successful in most cases. However, the break-up of jets has proved to be inconsistent with the fluid flow models and cannot be accurately described. Break-up is important since it is the final **phenomenon** in tensile deformation and therefore represents the limiting extent of jet elongation. Additionally, following break-up the jet fragments are particularly susceptible to lateral velocities and tumbling which dissipate the jets energy and further reduce its penetration performance.

Research by Hunting Engineering Limited has indicated that mechanical properties are related to the jet break-up phenomena. However, the deformation and break-up of shaped charge jets is not well understood from a metallurgical point of view. It is essential that the jet is in the solid state for jet break-up phenomena to be related to the mechanical properties of the liner material. This has been demonstrated here by theoretical analysis and more directly by observation of in-flight and captured jet fragments.

A series of experiments have been carried out in order to measure and analyse the deformation and attempt to put forward models for the break-up mechanisms in shaped charge jets. These were based upon a series of selected aluminium and aluminium alloys which were processed and heat treated to produce a range of mechanical properties. The properties under consideration are those which describe the materials strength, elongation and work hardening characteristics at intermediate strain rates under laboratory conditions. These have been used to relate metallurgical details to the nature of jet break-up. The better materials for shaped charge jets would appear to be high purity metals which exhibit large ductility through to fracture.

# Contents

<b>1</b>	<b>Introduction</b>	<b>1</b>
1.1	Historical Development of the Shaped Charge . . . . .	1
1.1.1	The Munroe Effect . . . . .	3
1.2	Deformation and Break-Up of Shaped Charge Jets . . . . .	4
1.3	Structure and Aims of this Thesis . . . . .	6
<b>2</b>	<b>Literature Survey</b>	<b>9</b>
2.1	Introduction . . . . .	9
2.2	Modelling of Jetting Processes . . . . .	9
2.2.1	Liner Collapse . . . . .	10
2.2.1.1	The Gurney Formula . . . . .	10
2.2.1.2	The Taylor Formula . . . . .	12
2.2.2	Jet Formation . . . . .	12
2.2.3	Jet Break-Up . . . . .	13
2.2.3.1	Incoherency . . . . .	15
2.2.3.2	Empirical Modelling of Break-Up . . . . .	15
2.2.4	Penetration . . . . .	16
2.2.4.1	Penetrating Rods . . . . .	17
2.2.4.2	Particulated Jets . . . . .	17

2.2.5	Hydrocode Modelling . . . . .	19
2.2.5.1	Materials Modelling in Hydrocodes . . . . .	20
2.2.5.2	Numerical Modelling of Break-Up . . . . .	21
2.3	Current Knowledge of Deformation Mechanisms . . . . .	22
2.3.1	Diffusion Based Processes . . . . .	24
2.3.1.1	Coble and Nabarro - Herring Creep . . . . .	24
2.3.1.2	Superplasticity . . . . .	26
2.3.1.3	Dislocation Creep . . . . .	27
2.3.2	Dislocation Based Deformation . . . . .	27
2.3.2.1	Dislocation Glide . . . . .	29
2.3.2.2	Dislocation Cells . . . . .	29
2.3.3	Twins . . . . .	31
2.4	Testing and Characterisation of Materials . . . . .	32
2.4.1	High Strain Rate Testing . . . . .	32
2.4.1.1	Shock Loaded Material . . . . .	33
2.4.2	Studies made on Jet Material . . . . .	35
2.4.3	Jetting Characteristics . . . . .	36
2.4.3.1	Classical Jets . . . . .	37
2.4.3.2	Fractured Jets . . . . .	39
2.4.3.3	Vaporous Jets . . . . .	39
2.4.4	Materials Properties . . . . .	41
2.4.4.1	Copper . . . . .	41
2.4.4.2	Brasses . . . . .	43
2.4.4.3	Zinc - Aluminium . . . . .	43

2.4.4.4	Aluminium . . . . .	44
<b>3</b>	<b>Investigation of Liner Materials</b>	<b>46</b>
3.1	Introduction . . . . .	46
3.1.1	Experiments With Aluminium Liners . . . . .	46
3.1.2	Experiments With Copper Liners . . . . .	47
3.1.3	Experimental Data . . . . .	47
3.2	Commercially Pure Aluminium . . . . .	50
3.2.1	Experimental Details . . . . .	50
3.2.2	Material for the Manufacture of Liners . . . . .	50
3.2.3	The Shaped Charge Liners . . . . .	50
3.2.4	Firing Conditions . . . . .	51
3.3	Non Heat Treatable Aluminium Alloys . . . . .	55
3.3.1	Experimental Details . . . . .	55
3.3.2	Material for the Manufacture of Liners . . . . .	55
3.3.3	The Shaped Charge Liners . . . . .	56
3.3.4	Firing Conditions . . . . .	56
3.4	Precipitate Strengthened Aluminium Alloys . . . . .	57
3.4.1	Experimental Details . . . . .	57
3.4.2	Material for the Manufacture of Liners . . . . .	57
3.4.3	The Shaped Charge Liners . . . . .	57
3.4.4	Firing Conditions . . . . .	59
3.5	Commercially Pure Copper . . . . .	60
3.5.1	Experimental Details . . . . .	60
3.5.2	Material for the Manufacture of Liners . . . . .	60

3.5.3	The Shaped Charge Liners . . . . .	60
3.5.4	Design of the Warhead Assembly . . . . .	61
3.5.5	Firing Conditions . . . . .	61
<b>4</b>	<b>Results</b>	<b>62</b>
4.1	Introduction . . . . .	62
4.2	Commercially Pure Aluminium . . . . .	63
4.3	Non Heat Treatable Aluminium Alloys . . . . .	75
4.4	Precipitate Strengthened Aluminium Alloys . . . . .	90
4.5	Commercially Pure Copper . . . . .	100
<b>5</b>	<b>Capture of Jet Fragments</b>	<b>108</b>
5.1	Introduction . . . . .	108
5.2	Experimental Details . . . . .	108
5.2.1	The Liner and Warhead Assembly . . . . .	108
5.2.2	The Soft Recovery Pack . . . . .	109
5.3	Laboratory Analysis of Recovered Jet Fragments . . . . .	109
5.3.1	Observed Features . . . . .	111
5.3.1.1	Fragment Size . . . . .	111
5.3.1.2	Surface Features . . . . .	112
5.3.1.3	Fracture Surfaces . . . . .	112
5.3.1.4	Grain Size . . . . .	112
5.3.1.5	Other Features . . . . .	114
5.3.2	X-Ray Diffraction . . . . .	114
5.3.3	Electron Microscopy . . . . .	120

<b>6</b>	<b>Target penetration</b>	<b>121</b>
6.1	Introduction . . . . .	121
6.1.1	Design of Charge . . . . .	121
6.1.2	The Target Stack . . . . .	123
6.1.3	Trials Instrumentation . . . . .	123
6.1.3.1	X-Rays . . . . .	123
6.1.3.2	Trip screens . . . . .	124
6.2	Results . . . . .	124
6.2.1	Volumetric Measurements . . . . .	124
6.2.1.1	Internal inspection . . . . .	124
6.2.1.2	Plate mass . . . . .	125
6.2.1.3	Plate volume . . . . .	125
6.2.1.4	Hole volume . . . . .	125
6.2.2	Metrology of target plates . . . . .	126
6.2.3	Microhardness Testing . . . . .	127
6.2.4	Metallography . . . . .	129
<b>7</b>	<b>Measurement of Jet Fragments In Flight</b>	<b>131</b>
7.1	Limitations of X-ray Photographic Imaging . . . . .	131
7.2	Analogue Measurement of Jet Fragments . . . . .	132
7.3	Digital Image Analysis . . . . .	132
7.4	Velocity Gradients . . . . .	135
7.5	Quantification of Jet Break-Up . . . . .	136
7.5.1	Jet Fragment Volume and Mass . . . . .	137
7.5.2	A Quantitative Jet Parameter . . . . .	137

<b>8</b>	<b>Lateral Velocity Induced by Shear</b>	<b>143</b>
<b>9</b>	<b>Discussion</b>	<b>146</b>
9.1	Introduction . . . . .	146
9.2	Materials Properties in Relation to Jet Break-Up . . . .	146
9.2.1	Ultimate Tensile Strength and Proof Stress . . . . .	147
9.2.2	The Grain Size Effect . . . . .	149
9.2.3	Work Hardening . . . . .	153
9.2.3.1	Effect of the Coefficient of Work Hardening . . . . .	154
9.2.3.2	Relationships between Work Hardening Characteristics and Jet Break-Up . . . . .	157
9.2.3.3	Stacking Fault Energy . . . . .	159
9.2.4	Elongation . . . . .	164
9.2.5	Deformation Energy . . . . .	169
9.3	Break-Up Mechanisms . . . . .	172
9.3.1	Validation of Deformation by Dislocation Motion at Very High Rates of Strain . . . . .	172
9.3.2	A Hypothesis for Shaped Charge Jet Break-Up . . . . .	175
<b>10</b>	<b>Conclusions and Recommendations for Further Work</b>	<b>179</b>
10.1	Shaped Charge Jets in the Solid State . . . . .	179
10.2	Jet Break-Up in Relation to the Quasi-Static Properties of Liner Materials . . . . .	180
10.3	Recommendations for Further Work . . . . .	182
10.3.1	Additional Materials . . . . .	182
10.3.2	Experimental Technique . . . . .	183

<b>A</b>	<b>Design of the Warhead Assembly</b>	<b>184</b>
<b>B</b>	<b>Laboratory Testing of Liner Material</b>	<b>193</b>
B.1	Tensile Testing . . . . .	193
B.1.1	Specimen Dimensions . . . . .	193
B.1.2	Commercially Pure Aluminium . . . . .	193
B.1.3	Aluminium Alloys . . . . .	193
B.1.4	Commercially Pure Copper . . . . .	194
B.1.5	Data Collection and Analysis . . . . .	194
B.2	Metallography . . . . .	194
B.2.1	Grainsize Analysis . . . . .	195
	<b>Acknowledgments</b>	<b>196</b>
	<b>References</b>	<b>197</b>

# List of Figures

1.1	The geometry of a shaped charge . . . . .	1
1.2	Liner collapse and jet formation . . . . .	2
1.3	Representation of the Munroe effect . . . . .	4
2.1	Schematic diagram for liner collapse . . . . .	14
2.2	Schematic diagram for jet penetration . . . . .	18
2.3	A simplified Ashby deformation map . . . . .	23
2.4	Effects of strain rate on the stress - strain response of aluminium under torsional loading . . . . .	33
2.5	Detail from the radiograph of a “Classical” pure aluminium jet . . . . .	38
2.6	Detail from the radiograph of a “Fractured” aluminium alloy jet . . . . .	40
2.7	Detail from the radiograph of a “Vaporous” tungsten particle, copper matrix powder metal jet . . . . .	42
3.1	Schematic of experimental set-up for vertical firings . . . . .	53
3.2	Experimental set-up for firing reference Al- $\perp$ . . . . .	54
4.1	Micrograph of as-manufactured pure aluminium . . . . .	65
4.2	Micrograph of annealed pure aluminium . . . . .	66

4.3	Stress versus strain for extruded commercially pure aluminium . . . . .	67
4.4	Stress versus strain for different orientations of extruded commercially pure aluminium in the as-manufactured condition . . . . .	68
4.5	Digitised image of aluminium jet "Al-M" . . . . .	69
4.6	Digitised image of aluminium jet "Al-O" . . . . .	69
4.7	Digitised image of aluminium jet "Al-⊥" . . . . .	70
4.8	Digitised image of aluminium jet "Al-  " . . . . .	70
4.9	Radiograph of aluminium jet "Al-M" . . . . .	71
4.10	Radiograph of aluminium jet "Al-O" . . . . .	72
4.11	Radiograph of aluminium jet "Al-⊥" . . . . .	73
4.12	Radiograph of aluminium jet "Al-  " . . . . .	74
4.13	Fracture surfaces of aluminium - magnesium alloys . . .	77
4.14	Stress versus strain for aluminium - magnesium alloys . .	78
4.15	Micrograph of 5251, Al ~ 2wt%Mg alloy . . . . .	80
4.16	Micrograph of 5154, Al 3.24wt%Mg alloy . . . . .	81
4.17	Micrograph of 5154, Al 3.45wt%Mg alloy . . . . .	82
4.18	Micrograph of 5083, Al ~ 4.5wt%Mg alloy . . . . .	83
4.19	Digitised image of jet from 5251 alloy (~ 2wt%Mg) . . .	84
4.20	Digitised image of jet from 5154 alloy (3.24wt%Mg) . . .	84
4.21	Digitised image of jet from 5154 alloy (3.45wt%Mg) . . .	85
4.22	Digitised image of jet from 5083 alloy (~ 4.5wt%Mg) . .	85
4.23	Radiograph of jet from 5251 alloy (~ 2wt%Mg) . . . . .	86
4.24	Radiograph of jet from 5154 alloy (3.25wt%Mg) . . . . .	87

4.25	Radiograph of jet from 5154 alloy (3.45wt%Mg) . . . . .	88
4.26	Radiograph of jet from 5083 alloy (~ 4.5wt%Mg) . . . . .	89
4.27	Stress versus strain for aluminium - copper - magnesium alloy of composition 2014 . . . . .	93
4.28	Micrograph of 2014 alloy, L168-T6511 . . . . .	94
4.29	Digitised image of jet from 2014 alloy, L168-T6511 . . . . .	94
4.30	Micrograph of 2014 alloy, As quenched . . . . .	95
4.31	Digitised image of jet from 2014 alloy, As quenched . . . . .	95
4.32	Micrograph of 2014 alloy, Naturally aged . . . . .	96
4.33	Digitised image of jet from 2014 alloy, Naturally aged . . . . .	96
4.34	Micrograph of 2014 alloy, Slow cooled . . . . .	97
4.35	Digitised image of jet from 2014, Slow cooled . . . . .	97
4.36	Radiograph of jet from 2014 alloy, As quenched . . . . .	98
4.37	Radiograph of jet from 2014 alloy, L168-T6511 . . . . .	98
4.38	Radiograph of jet from 2014 alloy, Naturally aged . . . . .	99
4.39	Radiograph of jet from 2014 alloy, Slow cooled . . . . .	99
4.40	Stress versus strain for copper in the as-manufactured and partially annealed conditions . . . . .	102
4.41	Micrograph of copper, C106-M . . . . .	103
4.42	Micrograph of partially annealed copper, C106-O . . . . .	104
4.43	Digitised image of copper jet "Cu-M" . . . . .	105
4.44	Digitised image of partially annealed copper jet "Cu-O" . . . . .	105
4.45	Radiograph of as-manufactured copper jet "Cu-M" . . . . .	106
4.46	Radiograph of partially annealed copper jet "Cu-O" . . . . .	107

5.1	The experimental set-up for soft recovery of jet fragments in liquid fire fighting foam . . . . .	110
5.2	Fragments passing through a solid foam target . . . . .	111
5.3	Micrograph of a captured jet fragment that indicates the crescent shape attributed to the soft capture technique . . . . .	113
5.4	Detail of microstructure in Figure 5.3 . . . . .	113
5.5	Section through recovered slug that exhibits a central “pipe” . . . . .	114
5.6	X-ray diffraction of liner material, as-manufactured . . . . .	115
5.7	X-ray diffraction of liner material, cold rolled 50% . . . . .	116
5.8	X-ray diffraction of liner material, cold rolled and then annealed . . . . .	116
5.9	X-ray diffraction of captured jet fragment . . . . .	117
5.10	X-ray diffraction of captured jet fragment . . . . .	117
6.1	Section through multi-laminate target stack after penetration . . . . .	122
6.2	Schematic diagram of hardness versus distance from the hole resulting from jet penetration . . . . .	128
6.3	Micrograph of shocked steel taken some distance from the hole . . . . .	130
6.4	Micrograph of heavily shocked steel taken adjacent to the hole . . . . .	130
7.1	Jet fragment length resulting from pure aluminium and copper liners . . . . .	133
7.2	Jet fragment length resulting from aluminium - magnesium alloy liners . . . . .	133
7.3	Jet fragment length resulting from aluminium - copper - magnesium - alloy liners . . . . .	134

7.4	Velocity gradients for copper, aluminium and aluminium - magnesium alloy jets . . . . .	136
7.5	Fragment mass distribution along pure aluminium and copper jets . . . . .	138
7.6	Fragment mass distribution along aluminium - magnesium alloy jets . . . . .	138
7.7	Fragment mass distribution along aluminium - copper - magnesium alloy jets . . . . .	140
7.8	Fragment volume distribution along pure aluminium and copper jets . . . . .	142
9.1	Fragment mass versus ultimate tensile strength . . . . .	151
9.2	Fragment mass versus proof stress . . . . .	152
9.3	Model true stress versus true strain curves with different values of work hardening coefficient . . . . .	155
9.4	Fragment mass versus coefficient of work hardening . . . . .	161
9.5	Fragment mass versus $\sigma_0$ . . . . .	162
9.6	Fragment mass versus rate of work hardening . . . . .	163
9.7	Fragment mass versus strain to failure . . . . .	166
9.8	Fragment mass versus strain to ultimate tensile stress . . . . .	167
9.9	Fragment mass versus the difference between the strain to the UTS and the strain to failure . . . . .	168
9.10	Fragment mass versus deformation energy per unity mass . . . . .	171
9.11	Schematic diagram of the effect of break-up on the jets velocity gradient . . . . .	176
A.1	Case for explosive warhead . . . . .	185
A.2	Liner dummy, for casting of explosives . . . . .	186

A.3	Locking ring for aluminium liners . . . . .	187
A.4	Liner blank used for heat treating aluminium alloys. . . .	188
A.5	Liner, final machined and heat treated form . . . . .	189
A.6	Firing condition, the assembled warhead ready for firing.	190
A.7	Modified locking ring for copper liners . . . . .	191
A.8	Copper liner, final machined and heat treated form . . .	192

# List of Tables

2.1	Illustration of the magnitude of strain rates resulting from Nabarro - Herring diffusion creep . . . . .	25
2.2	Illustration of the grain size required to maintain very high strain rates by Coble grain boundary diffusion creep . . .	26
2.3	Typical stacking fault energies for pure face centre cubic metals . . . . .	30
2.4	Qualitative classification of jet break-up . . . . .	37
3.1	Materials used for investigation of shaped charge liners .	48
3.2	Time delays for radiograph images relative to initiation of detonation . . . . .	49
3.3	Nominal chemical composition of E1B M/1050 A aluminium.	51
3.4	Chemical composition of non heat treatable aluminium alloys . . . . .	55
3.5	Nominal composition of precipitate strengthened 2014 - L168-T6511 aluminium alloy . . . . .	58
3.6	Nominal chemical composition of C106 copper. . . . .	60
4.1	Tensile properties of extruded pure aluminium . . . . .	64
4.2	Tensile properties measured for aluminium - magnesium alloys . . . . .	79
4.3	Tensile properties measured for aluminium - copper - magnesium alloys . . . . .	92

4.4	Tensile properties measured for copper . . . . .	101
5.1	Normalised peak intensity values for copper international standard . . . . .	118
5.2	Normalised peak intensities for the five materials tested by X-ray diffraction . . . . .	119
5.3	Peak intensities relative to the international standard for copper . . . . .	119
6.1	Materials and plate thickness for components of the target stack . . . . .	124
6.2	Calculated and measured plate masses . . . . .	126
6.3	Calculated and measured hole volumes . . . . .	127
7.1	Calculated average mass of jet fragments . . . . .	139
8.1	Values used to illustrate the effect of ultimate tensile stress (UTS) on lateral velocity . . . . .	145
9.1	Coefficient of work hardening and true strain values . . .	154

## CHAPTER 1

# Introduction

### 1.1 Historical Development of the Shaped Charge

Over the past fifty years a great deal of research effort has been directed into the development of shaped charges. This is a precision explosive device with both military and civil applications. It can be used in any situation that requires an accurately directed, concentration of explosive energy.

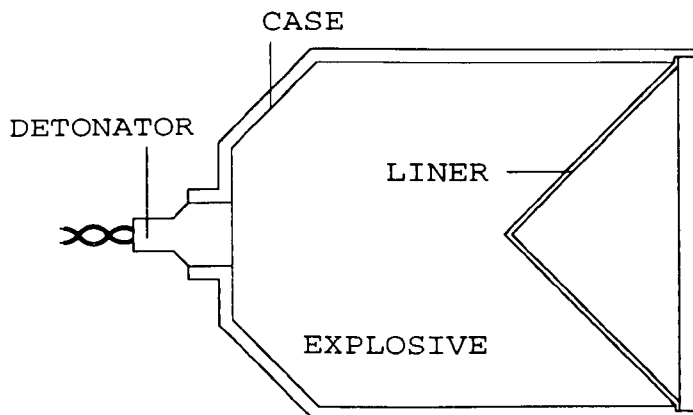


Figure 1.1: The geometry of a shaped charge

The basic geometry of a shaped charge jet is shown in Figure 1.1. The component features are: the liner, an explosive filling, a case and the detonating system. All features of a shaped charge jet can vary in geometry, however most critical to its performance is the liner configuration. Changes in the liners thickness, its angle, the mechanical properties

and microstructure of the liner material greatly effect the resulting jet.

The principle of shaped charges is relatively simple. A charge of explosives is used as a high energy driving force to act upon a metallic liner which is recessed into the charge. The energy thus transferred to the liner causes it to collapse towards its axis. From the point of collision a jet of liner material is projected forward with a very high velocity.

Figure 1.2 represents the initial stages of the jetting process. The first frame shows the detonated explosives exerting pressure on the liner. The second frame shows a partially collapsed liner ejecting a jet of material away to the right.

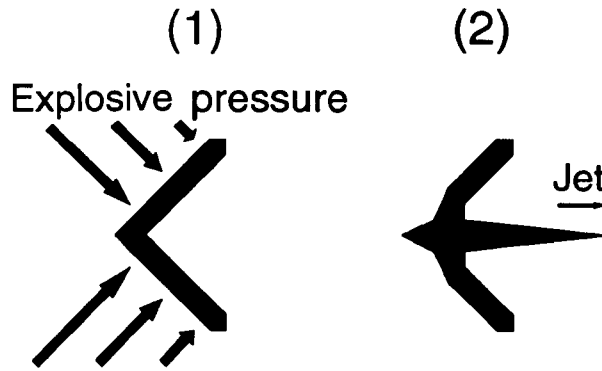


Figure 1.2: Liner collapse and jet formation

When the jet strikes a target the pressures induced are very large in comparison to the targets strength. As a result the jet penetrates the target, moving target material out of its path. The rod like geometry of the jet results in the formation of a deep narrow hole. A shaped charge jet is a mechanical device for focusing explosive energy onto a small area.

To a first approximation the strengths and viscosities of the jet and target materials can be neglected. This allows the use of the hydrodynamic assumption of incompressible, inviscid fluid flow. Therefore, the depth of penetration into a target is proportional to the length of the jet. The other materials properties of significance are the density of the jet material and the density of the target material. The expression which relates the depth of penetration to the properties of the jet and the target is given by Equation 1.1.  $\rho$  is the term for density and  $L$  refers to the

length of the jet - note that this length is the length of jet material and not necessarily the distance between the jets tip and its tail.

$$P_{\text{penetration}} = \sqrt{\frac{\rho_{\text{jet}}}{\rho_{\text{target}}}} L_{\text{jet}} \quad (1.1)$$

The performance of a shaped charge is measured by its ability to penetrate a target. To maximise this the jet is required to have a high length to diameter ratio.

Due to the progressive nature of the liners collapse, the velocity of the jet decreases from its tip to its tail. This velocity difference causes the jet to stretch in free flight. Were necking and subsequent break-up of the jet not to occur, then a long thin jet could be produced by allowing sufficient distance between the charge and target for the jet to elongate. However, the break-up phenomenon puts a finite limit on the amount of elongation that can occur.

### 1.1.1 The Munroe Effect

The detonation of explosives against a large block of metal creates an impression due to the pressure of the blast. The damage is not inconsequential but only a small proportion of the energy released has been absorbed by deformation of the metal. In 1888 Munroe [1] published a paper entitled “Modern Explosives”. In it he described the effect whereby an indent in the surface of the explosives is reproduced in negative in the adjacent surface of a steel plate. This became known as the “Munroe Effect” and the charge used as a “Shaped Charge”. In his paper Munroe puts forward a theory to describe how a mirror image indentation came to be produced in the metal targets.

*We have offered as an hypothesis to explain this phenomenon, that, where spaces exist between the gun-cotton <sup>1</sup> and the iron, portions of the undetonated gun-cotton, or of the products of the explosion, are projected through this space just as shot are from a gun, and that the indentations are produced by the impact of these moving particles.*

---

<sup>1</sup>Gun-cotton was the explosive used by Munroe in his experiments.

Figure 1.3 shows graphic representations of the impressions found in metal plates after the detonation of explosives (the explosives, however, have been represented as undetonated). (1) Shows the case for an unconstrained block of explosive. This has produced subsurface cavitation in the target material. (2) Shows the “Munroe Effect”, and (3) shows the effect of a metallic liner in the shaped charge cavity.

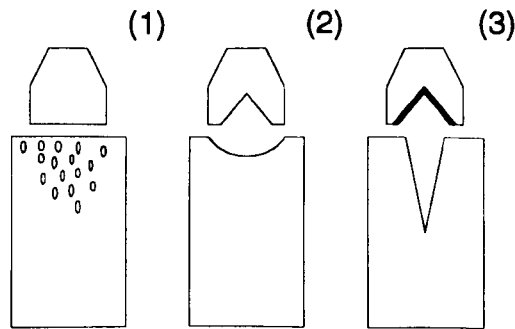


Figure 1.3: Representation of the Munroe effect

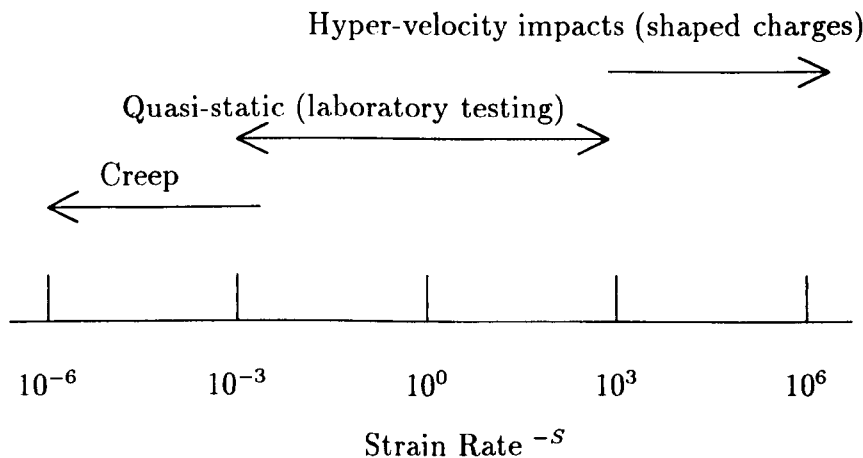
The Munroe effect was significantly improved upon when a metallic liner was added to the indent in the explosives. Further improvement resulted when a stand off was included, *ie.* a gap between the explosive charge and the target. Instead of a mirror image impression being formed in the target a narrower and considerably deeper hole was produced. The depth of penetration could be five, or more, times greater than the base diameter of the liner. A typical liner might be a copper, hollow conical shell with a base diameter of around 60mm, therefore the penetration of such a shaped charge might exceed 300mm into steel.

## 1.2 Deformation and Break-Up of Shaped Charge Jets

In the study of shaped charge warheads, there is one area in which there is a distinct lack of understanding: the effect of liner material on the performance of a shaped charge jet. When loaded by an explosive shock wave a shaped charge liner may experience stresses in the region of  $10^4 MPa$ . Compared to the value for the yield strength of most metals,

which is of the order  $10^2 MPa$ , this force is so great that the metal can be considered to have insignificant strength. The models currently available to describe the deformation of a shaped charge liner are based around the assumption that the liner material behaves as a near perfect fluid under these conditions. When these models were first developed it was assumed that the material behaved as a perfect fluid and that hydrodynamic theory could be used, thus numeric models for liner deformation are generally known as “hydrocodes”. Simpler analytical models still assume that the liner behaves as a perfect fluid.

The rates of strain in some parts of the jetting process are estimated to be higher than those for which constitutive equations currently exist. High rates of strain is an ambiguous term which is not specifically defined. The highest rates of strain that can be attained and instrumented with a reasonable degree of accuracy are of the order  $10^3 s^{-1}$ , the highest rates of strain that are believed to occur during the collapse of a shaped charge liner are of the order  $10^6 s^{-1}$ .



Given the conditions under which deformation takes place it was originally thought that the mechanical properties of the liner would not have a significant effect on jet performance. Since the yield strength of the material had been exceeded by such a large amount, a factor of about two orders of magnitude, all microstructural factors would be swamped. However, it was soon found that some metallurgical features could have a profound effect. It was seen that different classes of material, *ie.* pure metals, alloys and sintered powder material behaved in quite different fashions. More subtle differences, such as grain size, were also seen to

effect the jetting characteristics.

Historically the effect of microstructure on pure metals has been most studied. It was found that the materials grain size was related to jet performance, fine equiaxed grains resulted in a jet which elongated and fractured in the most ductile manner. Large grains, grains elongated by mechanical processing and single crystals caused the jets to fracture in a more brittle manner. This research was based on the assumption that the jet deforms plastically rather than by fluid flow. Therefore its deformation and subsequent failure on break-up must be governed by a set of mechanical properties. It had then been assumed that the mechanical properties which govern jet break-up are the same or similar to those which govern the deformation and failure of materials tested under quasi-static laboratory conditions. These assumptions can be substantiated by two considerations;

1. Firstly, materials properties such as grain size are observed to effect jet break-up. This would not be the case if the jet were behaving as a liquid.
2. Secondly, observation of jets shows elongation ceases after break-up. Therefore, although some very high strain rate deformation occurs in the formation of a jet, by the time break-up occurs the rate of deformation will have dramatically reduced.

### **1.3 Structure and Aims of this Thesis**

The literature survey - Chapter 2 - contains a brief history of shaped charges and identifies some of the more important developments in the analytical and numerical models of the jetting process. It is not intended to chronicle all the developments due to the number of people who have made contributions to the work in this field. In addition foreign workers may not have been reported in the literature if their work was considered sensitive. Those accredited with certain theories are therefore the first known in Great Britain, America and, in post war years, Western Europe.

In order to test the effect of materials properties on jet break-up it was decided to conduct a series of experiments where the mechanical properties of the liner could be varied and measured in a controlled manner.

All other test parameters were to be kept as near constant as possible. To achieve this the experiments were carried out using the same design of warhead, containing liners manufactured from different aluminium alloys, these experiments are described in Chapter 3 and the resulting data is presented in Chapter 4. The use of aluminium alloys allowed the mechanical properties to be tested over a wide range of values, while the material remained essentially pure and homogeneous but for a small precipitate content. Small amounts of alloying elements and appropriate heat treatment could result in an order of magnitude difference in some mechanical properties relative to high purity aluminium.

Additional experiments to capture jet fragments and to study the effect of penetration are described in Chapters 5 and 6 respectively. Captured jet fragments were used to study the relationship between the initial microstructure of the shaped charge liner and the resulting microstructure of fragments following break-up. Examination of targets which have been penetrated by shaped charge jets yield information about the effect of high speed deformation on microstructural properties and deformation mechanisms which cannot be observed directly in jet material. These experiments were conducted to provide supporting experimental evidence for theories describing the effect of mechanical properties and microstructure on jet break-up.

In Chapter 7 the analytical methods used to interpret the data in Chapter 4 are discussed. This includes justification of the methodology, discussion of their limitations and the derived numerical values which are used later in the discussion of the relationship between break-up and mechanical properties. Sufficient data is available at this point to conduct a theoretical analysis into the effect of break-up on the jets lateral velocity *ie.* a **phenomenon** which disperses the jet over a greater target area and thus reduces its penetration performance. This analysis is described in Chapter 8.

Qualitatively, the effect on jet characteristics of the materials metallurgical condition is at least recognised if not well known. However, quantitatively there is no established relationship. The aim of this study is to gain an understanding of the relationship between the metallurgical condition of a shaped charge liner and its jetting characteristics, particularly regarding the break-up phenomenon. Chapter 9 discusses the effect

of mechanical properties and microstructure on jet break-up. There is then a theoretical analysis of the dislocation deformation mechanism at very high strain rates which is used in the final section of this chapter to propose a theory for the deformation and break-up of shaped charge jets.

Finally in Chapter 10, the conclusions drawn from the work described in this thesis are presented and some recommendations are made for work to be carried out in the future.

## CHAPTER 2

# Literature Survey

### 2.1 Introduction

The purpose of this chapter is to allow discussion and criticism of existing literature relevant to the work presented in this thesis. This has been divided into three principle sections: Modelling of Jetting Processes, Current Knowledge of Deformation Mechanisms and The Testing and Characterisation of Materials. The first two sections give a detailed background to the theoretical analysis of high strain rate deformation. Firstly, through phenomenological analysis of the jetting process and secondly in the context of process mechanisms. In the final section, practical investigations of material at high strain rates have been discussed and analysed.

A complete history of the developments in shaped charge technology is given by Cook [2]. For an overview of developments since the end of the second world war, Chou and Flis [3] is recommended. The most recent and comprehensive work available on the subject is the book "The Fundamentals of Shaped Charges " written by Walters and Zukas [4]

### 2.2 Modelling of Jetting Processes

The performance of a shaped charge can be optimised by modifying its design parameters. These are comprised of a combination of geometric and material variables. To find the optimum design parameters by empirical testing is expensive and time consuming. Therefore, the ability to model the reaction of a shaped charge to explosive loading is highly desirable. In this section, models for the basic principles required to

describe shaped charge phenomena are presented. These will be considered in four subsections each relating to a specific process; liner collapse, jet formation, break-up, and penetration. These steps form a logical sequence in which to consider the development of jetting theories and the form has been used in the following text.

It is estimated that the first very crude shaped charges were used as much as two hundred years ago. It was known that improved performance was gained from explosives when used with concave blasting caps. However, the actual principles of shaped charges were not understood. In 1888 Munroe [1] investigated the use of unlined shaped charges for creating impressions in metal sheets. In this work, the first theoretical analysis was made on the process of cavity formation. It was not until 1936 that Wood [5] recognised the enhancement obtained from a metal lined shaped charge. Further developments were made during the second world war with many countries independently researching their own shaped charge weapons *ie.* the American “Bazooka” or the German “Pantzerfaust”.

In the early 1940s Taylor [6] and Gurney [7] started to develop theoretical models for the acceleration of material by the impact of a detonation wave. Their original work was on explosive configurations. This was soon modified to describe the implosive geometry of the liner collapse process for shaped charges. By 1948 Birkhoff *et al.* [8] had developed a model for the formation of shaped charge jets. This was based upon the analysis of X-ray images - radiographs - taken shortly after detonation. These revealed a continuous flow of liner material which resulted in the formation of a jet and slug. In 1952 Pugh, Eichelberger and Rostoker [9] reworked the concept developed by Birkhoff *et al.* This became known as the PER theory. This describes the velocity and mass distribution of liner material during the formation of a jet and slug.

## 2.2.1 Liner Collapse

### 2.2.1.1 The Gurney Formula

Gurney’s [7] formula derives a value for  $V_0$ , the velocity of material accelerated by an impinging detonation wave. In its generalised form the

Gurney equation can be expressed as,

$$V_0 = (2E)^{\frac{1}{2}} \mathcal{F}(\mu) \quad (2.1)$$

Where  $E$  is the chemical energy supplied by the explosive - the ‘‘Gurney Energy’’ - and the function  $\mathcal{F}(\mu)$  is the ratio of metal to explosive mass per unit length.

It is assumed in Gurney’s derivation that the expanding gases have a linear velocity distribution. Kennedy [10] correctly identified this as one of the major sources of error and developed a new equation which considered the non uniform change in gas velocity. However, he then showed this version to be considerable more complex and achieved very little overall improvement in accuracy.

A successful development of the Gurney equation was carried out by Chant ret [11]. In this approach - specifically based on the implosive geometry of a shaped charge - a rigid fixed partition is assumed to separate imploding and exploding gases. For any point along the liner, the radius of this boundary,  $R_x$  is found by solving the equation

$$\begin{aligned} R_x^3 + 3R_x \left[ (R_e + R_i) \frac{\rho_0}{\rho_{cj}} \left( \frac{M_e}{C} R_i \right) + R_i R_e \right] \dots \\ \dots - 3(R_i + R_e) R_i R_e \left[ \frac{2}{3} + \frac{\rho_0}{\rho_{cj}} \left( \frac{M_i}{C} + \frac{M_e}{C} \right) \right] = 0 \end{aligned}$$

Where  $R_i$  and  $R_e$  are the internal and external radii of the explosive.  $M_i$  and  $M_e$  are the mass per unit length of the liner and case and  $\rho_0$  and  $\rho_{cj}$  are the initial and Chapman-Jouguet densities of the explosive. The Chapman-Jouguet density is that of the explosive gases after detonation, but before the onset of unsteady flow as they expand. The revised Gurney equation can now be expressed as,

$$V_0 = \left[ \frac{2E}{\left( \frac{R_e^2 - R_i^2}{R_x^2 - R_i^2} \right) \frac{M_i}{C} + \frac{1}{6}} \right]^{\frac{1}{2}} \quad (2.2)$$

It can be seen that this equation still fits the original form of the Gurney formula, Equation 2.1. In its present form it is found to be very reliable for the analysis of shaped charges.

Further refinements can be made if another of Gurney's original assumptions is altered. The liner material has previously been considered to be instantaneously accelerated to its terminal velocity  $V_0$  when acted upon by the detonation wave. Eichelberger [12] developed a model for linearly increasing velocity and Chou *et al.* [13] have suggested the most realistic model yet by giving  $V_0$  a time dependant term.

### 2.2.1.2 The Taylor Formula

Gurney had assumed that explosively loaded materials flowed in a direction normal to their surface. This is not a valid assumption unless the detonation wave strikes the surface at a normal incidence. When the detonation wave strikes at an angle, the direction of material flow is altered. The Taylor [6] theory relates the resultant material velocity,  $V_0$  and the velocity of the detonation wave,  $U$  to give an estimate of this difference in direction. This is expressed as an angle,  $\psi$  which is measured from the normal to the materials surface.

$$\sin \psi = \frac{V_0}{2U} \quad (2.3)$$

The value for  $V_0$  used in this equation can be calculated using the Gurney formula described earlier.

### 2.2.2 Jet Formation

Analysis of the jet formation process was first carried out by Birkhoff *et al.* [8]. Their theory used numerous assumptions to describe local conditions at the point where collapsing material meets on the liner axis. The greatest significance of their theory was to recognise that the reaction of liner material, acted upon by forces many times its own strength, could be described by hydrodynamic theory. The material was treated as a fluid and for this reason, deformation under these conditions is often referred to as "hydrodynamic flow".

Their theory was limited in that it failed to predict one very important phenomenon, *ie.* shaped charge jets elongate. The jets tip travels faster than its tail. This is due to the continuous change in angle of the liner wall relative to its axis during the collapse process - Birkhoff *et al.* had assumed this angle to be constant.

Pugh, Eichelberger and Rostoker, (PER) [9], greatly developed this theory and were able to produce formulae which could reliably predict some of the basic jet characteristics. Walsh [14] considered cases where no jetting occurred and related this to the fact that the liner material is compressible and not a perfect hydrodynamic fluid. Carleone and Chou [15] extended the basic PER theory such that the jets length, radius and strain could be calculated. However, this analysis resulted in a particularly cumbersome expression.

The PER theory describes the velocity and mass distribution of liner elements as they form a jet and slug. Referring to Figure 2.1, the jet velocity,  $V_j$ , is found using the Bernoulli theory and results in an equation of the form

$$V_j = V_0 \left( \operatorname{cosec} \frac{\beta}{2} \right) \cos \left( \alpha + \psi - \frac{\beta}{2} \right) \quad (2.4)$$

The velocity of the slug is found using similar arguments

$$V_s = V_0 \left( \sec \frac{\beta}{2} \right) \sin \left( \alpha + \psi - \frac{\beta}{2} \right) \quad (2.5)$$

$V_0$  is the terminal velocity of the liner element, this may have been derived from a Gurney type formula such as Equation 2.2.  $\alpha$  is the angle between the liner and its axis before firing and  $\beta$  is the angle made between a liner element and the liner axis as that element arrives on axis.  $\psi$  is the angle by which the direction of the materials flow deviates from the normal to its surface. This can be estimated using the Taylor formula, Equation 2.3. The proportion of liner mass entering the jet and slug at any point in time is given by combining equations for conservation of mass and momentum. The equation for the mass proportion of the jet is as follows

$$\frac{dm_{jet}}{dm_{liner}} = \sin^2 \frac{\beta}{2} \quad (2.6)$$

### 2.2.3 Jet Break-Up

This phenomenon is currently the least understood of the jetting processes. It is one of the most difficult effects to model and probably the most dependent upon materials properties. It has been suggested that break-up is affected by such factors as grain size - Lichtenberger *et al.* [16] - or texture, Jamet [17]. Therefore some of the assumptions made

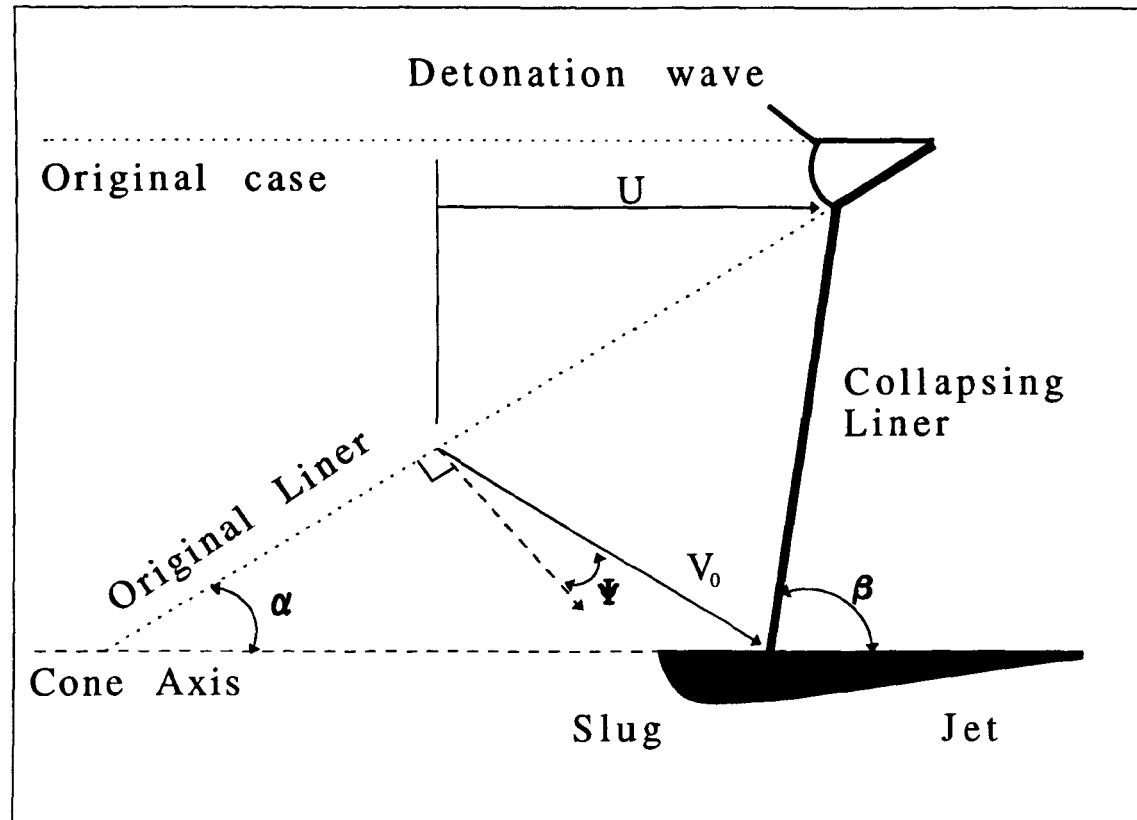


Figure 2.1: Schematic diagram for liner collapse after Pugh *et al.* [9]. The parameters  $\alpha$ ,  $\beta$ ,  $\psi$ ,  $U$  - the detonation velocity - and  $V_0$  - the collapse velocity are components of the Gurney formula - Equation 2.1 - and the Taylor formula - Equation 2.3.

by hydrodynamic theory must be considered as being invalid, at least during the jetting stage. The “fluid” cannot be homogeneous or have isotropic properties as had previously been considered, otherwise parameters such as grain size could not effect the break-up process. The experimental observations on break-up made by Lichtenberger and Jamet will be discussed in Section 2.4.3. In this section theoretical modelling of the phenomenon will be considered.

### 2.2.3.1 Incoherency

Incoherency is a term that will be used frequently in this thesis and which requires an explanation. This phenomenon has been extensively studied by Chou *et al.* [18] [3]. Break-up of a standard jet occurs along its length, the fractures are perpendicular to its axis - see Figure 2.5. When a jet breaks-up in parallel to its axis and material then moves radially outwards the effect is described as incoherency. There are two main causes of incoherency.

When the collapse velocity of the liner exceeds the sonic velocity of the liner material, the jet becomes incoherent. This is due to the complex interactions of shock waves within the material. As the collapse velocity decreases from the liners apex to its base, this phenomena is usually only seen in the leading section of the jet. This is the most common cause of incoherency.

Single crystal liners and liners with a large grain size are seen to exhibit a limited form of incoherency. These jets have a tendency to fracture parallel to their axis. Figure 2.6 shows detail of a jet produced by a single crystal liner. Close examination of the leading few particles show them to exhibit this form of incoherency. “Fractured” jets are discussed further in Section 2.4.3.2.

### 2.2.3.2 Empirical Modelling of Break-Up

The investigation of break-up phenomena has been a recent undertaking. Mott [19] carried out the first analysis of fragmenting shell cases as early as 1947. The first model able to predict break-up with reasonable accuracy was derived by Hirsch [20] [21] who used an empirically calculated constant,  $V_{pt}$  - the “plastic velocity” - to calculate the break-up

time,  $t_b$

$$t_b = \frac{2r_0}{V_{pl}} \quad (2.7)$$

Where  $r_0$  is the jets radius at the time of formation.

The term  $V_{pl}$  is derived from some of the jets characteristics. For a given design of charge, the velocity distribution along the length of the jet is found to be approximately linear. The range of the velocity profile is given by the difference in velocity between the jets tip and its tail. The number of particles into which these jets break-up is approximately constant. The plastic velocity is derived by dividing the velocity range by the number of jet particles.

In most cases this formula gives reasonably accurate values for  $t_b$  the break-up time. It is, however, independent of metallurgical state and therefore of limited value. Haugstad [22] has made an analysis of a theoretical jet from which he obtained an expression for the break-up phenomena: this proved to be of a similar form to that given by the Hirsch model.

All these formulae suffer the same drawbacks in that they are empirical approximations. They are based on assumptions of perfectly plastic, incompressible materials and do not contain data relevant to the metallurgical state of the liner material. As such it is surprising that the models work as well as they do. However, it should be noted that these equations are usually only applied to homogeneous pure metals with a low ultimate tensile strength: other types of material (*eg.* high strength alloys) are much harder to model.

Analytical models predicting the development and break-up of jets have been developed by Hunting Engineering Limited and other organisations. These are based on formulae similar to those mentioned previously and produce quite reliable jetting data [23].

#### **2.2.4 Penetration**

Much penetration theory was developed simultaneously with that for jet formation as the basic principle behind each is the conservation of momentum. The process of penetration is made more complex as the colliding bodies are in different states. The target is cold, solid and

undeformed, while the jet is hot, probably solid and deforming at very high rates. The jet and target may also be entirely different materials.

#### 2.2.4.1 Penetrating Rods

Birkhoff *et al.* [8] used the Bernoulli equation to derive the original penetration equation. This considered a long rod penetrator of density  $\rho_j$  travelling at a constant velocity  $V$ , into a target of density  $\rho_t$ , with a penetration velocity of  $U$  - see Figure 2.2.

$$\rho_j(V - U)^2 = \rho_t(U)^2 \quad (2.8)$$

Integration of the penetration velocity with respect to time for a jet of length  $L$  yields the total depth of penetration.

$$P = \left( \frac{\rho_j}{\rho_t} \right)^{\frac{1}{2}} L \quad (2.9)$$

This relationship, known as the Hill-Mott-Pack equation, indicates the importance attached to high density jets. These can be seen to produce a greater depth of penetration per unit length of jet.

#### 2.2.4.2 Particulated Jets

Pack and Evans [24] modified Birkhoff's equation in order that a non continuous jet could be considered,

$$\lambda\rho_j(V - U)^2 = \rho_t(U)^2 \quad (2.10)$$

$\rho_j$  is now taken as the average density of the jet when the space swept out between elements is included in its volume. The factor  $\lambda$  is taken as unity for a continuous jet and two for a fully particulated jet. This equation predicts the penetration to increase as the jet particulates due to an effect described as "after-flow". The inertia of the target material is said to cause penetration to continue after a jet element has been used up in the penetration process.

This explanation was questioned by Eichelberger [25] who suggested instead that the value of  $\lambda$  did not reach a value of two as after-flow did not occur (except in the special case for exceedingly soft targets

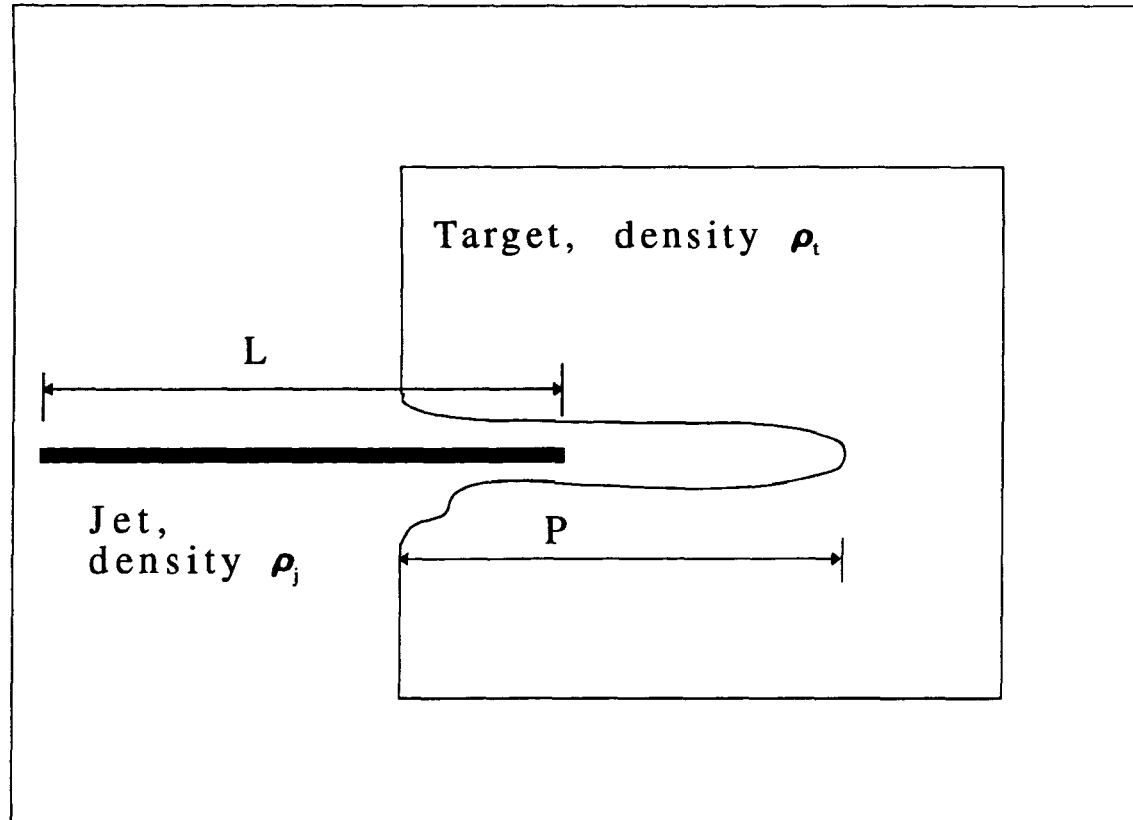


Figure 2.2: Schematic diagram for jet penetration after Birkhoff *et al.* [8]. The total depth of penetration,  $P$  is expressed as a function of the target density  $\rho_t$ , the jet density  $\rho_j$  and the jet length  $L$  - Equation 2.9.

such as lead). In addition, he argued that as the tail end of the jet entered the target its velocity was too low to produce true hydrodynamic penetration and that lateral velocity effects and tumbling prevent the jet elements from reaching the bottom of the hole as they collide with its sides. This reduces the effective length of the jet and therefore the depth of penetration.

### 2.2.5 Hydrocode Modelling

Hydrocodes are a particular kind of computer program used to simulate non-linear, dynamic material responses, *eg.* those induced by explosions or impacts. They solve the conservation equations of motion coupled with materials models which may have varying degrees of complexity. A recent overview of hydrocode modelling capabilities is given by Anderson [26]

The conservation equations are “discretized” using either finite element or finite difference techniques, *ie.* solid bodies are modeled by a numerical grid in which the reaction of each node is described. These equations are generally written using either Eulerian or Lagrangian mathematical descriptions. Each has advantages and disadvantages: Lagrangian codes provide good spatial resolution relative to the number of grid cells needed to describe the problem. They are most easily adaptable to material constitutive modelling in that the grid follows the motion of individual volumes of material. However, severe distortions of the grid sometimes limits the usefulness of Lagrangian codes to low strain conditions. Eulerian codes, with their fixed coordinate systems, can be used to consider problems where higher strains occur. They are, though, not as adaptable to materials modelling as the Lagrangian codes.

Materials modelling can be divided into three areas: the materials response to compressibility - equations of state, its resistance to deformation - constitutive modelling and its reduced ability to carry stress as damage accumulates - failure modelling. Of these only the equations of state are relatively well characterised for metals.

### 2.2.5.1 Materials Modelling in Hydrocodes

The aim of much of the work on testing materials at very high rates of strain is to produce a mechanical equation of state. An equation which can relate stress, strain and strain rate. At present there are no reliable equations to describe materials at very high strain rates. In cases where the material also experiences very high strain to failure, there is no reported data.

The general form of constitutive models in hydrocodes is to modify the yield stress in order to achieve the desired flow characteristics. If the yield stress is set as infinite (or very high) the material can be treated as perfectly elastic. If the yield stress is set to zero then the material can be treated hydrodynamically. With the yield stress set at an intermediate level modelling of an elastic - plastic material is achieved. Strain hardening, strain rate dependency and temperature effects can be modelled by further modification of the yield stress. A problem with this approach to constitutive modelling is that the method of modifying the yield stress is empirically derived or estimated.

Hollomon [27] has developed some equations of state in relatively simple form where the effects of strain rate,  $\dot{\epsilon}$ , and temperature were considered separately. Johnson and Cook [28] combined these variables into a single equation, this was later modified by Lips *et al.* [29] whose final form is given as,

$$\sigma = (A + B\epsilon^n) \left( 1 + C \ln \frac{\dot{\epsilon}}{\dot{\epsilon}_0} \right) (1 - T_H^m) \quad (2.11)$$

Where  $T_H^m$  is the homologous temperature, *ie.* the test temperature of the material divided by the temperature at its melting point.  $\dot{\epsilon}_0 = 1s^{-1}$  is an arbitrary base strain rate and  $A, B, C, m$  and  $n$  are empirical parameters.

It was recognised by Lips *et al.* that the empirical values in their equation should have some physical meaning.  $A$  is often written as  $\sigma_0$  in similar equations and is taken to be the static yield strength.  $B$  and  $n$  describe work hardening,  $C$  represents strain rate sensitivity and  $m$  thermal softening.

Failure modelling in hydrocodes is particularly difficult as it becomes necessary to describe when and how to model breaking of the grids. It

is also difficult to predict what type of failure will occur. Current failure models relate the total accumulated damage to strain through empirical constants. At a predetermined level of damage the material is said to fail. Until a better understanding of deformation at high rates of strain exists it is unlikely that it will be possible to make improved failure predictions.

The results produced by a hydrocode depend upon the material models it contains and also on the numerical scheme of the hydrocode itself. However, although the accuracy of these codes is generally good they take up large amounts of computer memory: the mesh size used is therefore limited. This restricts the ability to model high strain effects without the need for defining a new mesh. The re-meshing process incorporates errors and requires exceptional computer run time.

Analytical models which describe the movement of mass points in a theoretically incompressible fluid are cruder in their predictions of jetting processes, but they are much quicker to run and require much less memory space than the hydrocodes.

#### 2.2.5.2 Numerical Modelling of Break-Up

Various attempts have been made at hydrocode modelling of the break-up phenomena. Chou and Carleone [30] [31] [32] have carried out a comprehensive study using the Lagrangian based hydrocode HEMP. Their results show that variations in the jets yield strength or velocity could cause plastic instabilities to occur. Miller [33] has used the PISCES code and included constitutive models for strain hardening and thermal softening. The occurrence of instabilities was in this case attributed to the point during the deformation process at which thermal softening becomes dominant over strain hardening. These hydrocodes suffer similar criticisms as analytical models. Given some arbitrary initial perturbation, the profiles of necks are predicted to develop in a very similar manner to those seen in radiographs. There is, though, no description included in the model that takes account of the mechanism of deformation.

## 2.3 Current Knowledge of Deformation Mechanisms

At present there is no reliable theory describing the deformation mechanisms involved in the jetting processes. Therefore it is necessary to consider existing theories for deformation mechanisms. These were classified by Ashby [34],

“Firstly, a stress which exceeds the *theoretical shear stress* causes flow even in a defect free crystal; we call this *defectless flow* to distinguish it from all other kinds of plastic deformation, since they require defects to be present. Second, the *glide motion of dislocations* can lead to extensive plastic flow. At high temperatures the ability of dislocations to climb as well as glide introduces a third mechanism: *dislocation creep*.<sup>1</sup> Point defects also permit plastic flow when they move: two independent kinds of *diffusional flow* result from flow of point defects through grains and round their boundaries; these forth and fifth mechanisms are sometimes called *Nabarro - Herring creep* and *Coble creep*, respectively. Finally *twinning* provides a sixth mechanism; unlike the others it can supply only a limited amount of deformation”.

These mechanisms will be discussed in detail. The discussion will aim to identify known deformation mechanisms thought capable of operating at high strain rates and eliminating those unable to satisfy the conditions required for jetting processes. The deformation mechanisms to be considered will be described in ascending order of the strain rates at which they normally occur. This automatically tends to separate the diffusion controlled processes: Coble, Nabarro - Herring and dislocation creep, from the dislocation controlled mechanisms. This is summarised

---

<sup>1</sup>It may be questioned that dislocation glide and dislocation creep are distinguishable, independent mechanisms. The two display different and characteristic, activation energies; and give strain rates which depend on stress in different and characteristic ways. So they are certainly distinguishable mechanisms, both are potentially able to permit steady state deformation. But it is not clear that they are independent. Only alternative independent mechanisms (*ie.* those giving additive strain rates) appear as separate (deformation) fields.

by the Ashby deformation map in Figure 2.3. This schematically shows the relationship between strain rate, applied stress and temperature.

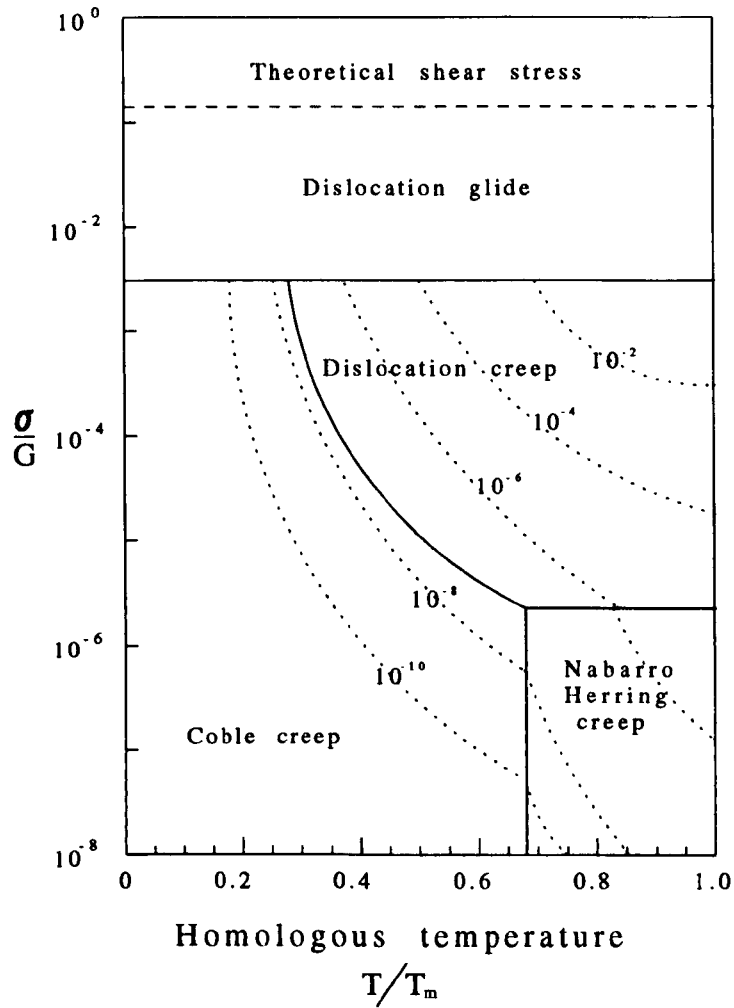


Figure 2.3: A simplified Ashby deformation map which relates the applied stress and temperature to deformation mechanism. Strain rates are indicated by contour lines

### 2.3.1 Diffusion Based Processes

Creep occurs at low stress and preferentially at high temperatures. In the non-perfect crystal structure of most materials, the amount of uninterrupted glide that a dislocation can make is very limited. They can normally be considered to be stationary very shortly after a load has been applied. Deformation can then only occur by diffusion of ions and defects in the crystal lattice. As has been quoted previously there are three mechanisms by which this can occur: Coble creep, Nabarro - Herring creep and dislocation creep.

#### 2.3.1.1 Coble and Nabarro - Herring Creep

These two processes appear to be very similar but have different mechanisms. Nabarro - Herring creep is only dominant at high temperatures when diffusion is able to occur throughout the grains without the need for specific diffusion paths. This mechanism is not able to accommodate high strain rates. The requirement for grains to maintain an ordered lattice structure limits the diffusion rate and it is energetically unfavourable to disrupt an ordered crystal lattice. Coble creep uses grain boundaries as diffusion paths and is limited in its effect to these regions. Diffusion rates are much higher at grain boundaries as the crystals lattice structure naturally breaks down in these regions. The atomic packing density is therefore lower and there is no ordered structure to be maintained.

The diffusion of a metal ion through a lattice requires the presence of vacancies. There are mechanisms by which an ion can diffuse without vacancies, however these are very slow in comparison. The diffusion of vacancies through a material is much faster than that of ions as they are not hindered by their own size. The Nabarro - Herring equation for vacancy creep gives the resultant strain rate,  $\dot{\epsilon}$  as

$$\dot{\epsilon} = \frac{8\sigma\mathbf{b}^3 D_{vac}}{d^2 kT} \quad (2.12)$$

Inserting typical values for the parameters in this equation indicates the magnitude of strain rates controlled by bulk (Nabarro - Herring) diffusion. This is illustrated in Table 2.1. Note,  $\mathbf{b}$  is the materials Burger's vector and  $D_{vac}$  is the coefficient of self diffusion for vacancies. The grain size is  $d$ , temperature  $T$ , and the applied stress is  $\sigma$ .  $k$  is Boltzman's

constant. The strain rate calculated in this example is fourteen orders of magnitude lower than the maximum strain rates experienced in the jetting of shaped charges.

$\underline{\mathbf{b}}^3 = 10^{-29} \text{ m}^3$ $D_{vac} = 10^{-13} \text{ m}^2\text{s}^{-1}$ $d = 10^{-3} \text{ m}$ $T = 750 \text{ K}$ $\sigma = 300 \times 10^6 \text{ Nm}^{-2}$ $k = 1.381 \times 10^{-23} \text{ JK}^{-1}$	<p>Equation 2.12</p> $\dot{\epsilon} = \frac{8\sigma \underline{\mathbf{b}}^3 D_{vac}}{d^2 k T}$
<p>Calculated strain rate, <math>\dot{\epsilon} \simeq 10^{-7} \text{ s}^{-1}</math></p>	

Table 2.1: Illustration of the magnitude of strain rates resulting from Nabarro - Herring diffusion creep

The Coble creep formula - Equation 2.13 - is seen to be of a similar form to that given by Nabarro - Herring - Equation 2.12. This expression for strain rate is given as

$$\dot{\epsilon} = \frac{150\Omega\delta D_{gb}\sigma}{\pi k T d^3} \quad (2.13)$$

Where the grain boundary diffusion coefficient is given by the expression,  $D_{gb} = D_{0gb} \exp(-Q_{gb}/RT)$ .  $D_{0gb}$  is a frequency factor,  $Q_{gb}$  is the activation energy for grain boundary diffusion and  $R$  is the gas constant. In comparison to Equation 2.12,  $D_{gb}$  is similar to  $D_{vac}$  and the value of  $\Omega$  - which represents the atomic volume - is virtually identical to  $\underline{\mathbf{b}}^3$  - the Burgers vector term.  $\delta$  is the thickness of the diffusion path, *ie.* the grain boundary.

This deformation mechanism was examined by Chokshi and Mayers [35]. They investigated the possibility for high strain rate superplasticity. By rearranging Equation 2.13 they found the theoretical grain size required to support diffusional deformation at strain rates of  $\dot{\epsilon} \geq 10^4 \text{ s}^{-1}$ . The values used to illustrate this are given in Table 2.2

$\delta D_{gb} = 5 \times 10^{-15} \times \exp(-104000/RT) \text{ m}^3\text{s}^{-1}$ $\Omega = 1.2 \times 10^{-29} \text{ m}^3$ $\sigma = 300 \times 10^6 \text{ Nm}^{-2}$ $T = 750 \text{ K}$ $\dot{\epsilon} \geq 10^4 \text{ s}^{-1}$ $k = 1.381 \times 10^{-23} \text{ JK}^{-1}$ $R = 8.314 \text{ JK}^{-1} \text{ mol}^{-1}$	A variation on Equation 2.13  $d = \left( \frac{150\Omega\delta D_{gb}\sigma}{\pi kT\dot{\epsilon}} \right)^{\frac{1}{3}}$
Calculated grain size $\leq 0.01 \mu\text{m}$	

Table 2.2: Illustration of the grain size required to maintain very high strain rates by Coble grain boundary diffusion creep

### 2.3.1.2 Superplasticity

Alloys which are superplastic at low rates of strain have been known for some time. They are often binary alloys which utilise a eutectoid or similar feature in their phase equilibrium diagram to develop a fine grain size. This is necessary as superplasticity relies on grain boundary diffusion. A fine grain size increases the area of grain boundary per unit volume material and therefore the amount of deformation possible per unit volume material. Detailed discussion on superplastic deformation is given by Pilling and Ridley [36].

One feature of superplasticity, that the amount of deformation per unit volume of material is increased, may apply to high strain rate deformation. This could be achieved in two ways: the dislocation density in a cell wall could increase - possibly causing a local failure if the material formed an adiabatic shear band - or the cell size could be reduced - thus increasing the overall dislocation density of the material without increasing it greatly in a localised area. Reduced dislocation cell size has been reported in explosively shocked material, Section 2.3.2.2. There is as yet no proof that very small dislocation cells form at the strain rates involved in the jetting processes, however the theory appears plausible.

It has been postulated that the amount of deformation that occurs per unit volume effects the jetting performance. However, this theory is incomplete as it does not explain why jetting performance should be related to grain size. This observation suggests the grain boundaries may be an important source of dislocations required in the formation of either adiabatic shear bands or fine dislocation cell structures. Decreasing the grain size would increase the area of grain boundary per unit volume of material. Therefore, if grain boundaries act as dislocation sources, the number of dislocations generated per unit volume of material would also increase.

Superplastic properties at high rate of strain are not realistic as the ultra fine grain sizes required are not currently attainable. However, it may be useful to consider the process of dynamic recrystallisation. This is a mechanism which is in some respects analogous to that described by superplastic theory if it is considered in the context of the dislocation phenomena for cell formation in Section 2.3.2.2.

#### **2.3.1.3 Dislocation Creep**

The climb of edge dislocations can be brought about by the diffusion of either metal ions or vacancies to the base of the extra half plane. Under explosive loading there may be large vacancy concentrations and sufficient activation energy for rapid diffusion to occur. However, diffusion controlled mechanisms are inevitably unable to result in large strains at high strain rates.

### **2.3.2 Dislocation Based Deformation**

At low stresses a dislocation is not free to glide through a material as its path is blocked by various types of obstacle. As the applied stress is raised the dislocations may become sufficiently energetic to overcome these obstacles.

Screw dislocations can begin to cross slip as the applied stress is raised. This mechanism utilises alternative slip planes which enable the dislocation to avoid obstacles by temporary changes in their direction. At higher stresses Orowan looping can occur. Precipitates or inclusions are be looped by dislocations - which are not required to change their

slip plane - the main body of the dislocation is then able to move on. However, the obstacle is now left surrounded by a dislocation. This then acts in addition to the local strain field of the precipitate or inclusion and further looping by subsequent dislocations is made more difficult. An alternative means for bypassing an obstacle is for it to be sheared or cut by a dislocation. The additional surface area this generates can make this process very energy consuming. Certain incoherent obstacles are therefore very efficient at hindering the movement of dislocations. In some cases, though, cutting of obstacles disperses them into the crystal lattice, thus neutralising their effect against further dislocation movement.

When dislocations interact with each other they may form a sessile dislocation. The combination of two mobile defects can result in the formation of a single defect which is unable to move within the crystal lattice. When large arrays of sessile dislocations form, the resulting forest is a major barrier to all subsequent dislocation motion.

The interaction of dislocations with inclusions, precipitates, solutes and other dislocations increasingly restricts the mobility of other dislocations. These obstacles are associated with a surrounding strain field, this reacts with the strain field of a dislocation in one of two ways: the dislocation can be repelled by a strain field and thus require extra energy to pass the obstacle or it can be attracted in which case additional energy is required to break the dislocation away from the obstacle. The result of either interaction is that the dislocation movement is impeded and the material's yield stress is increased. This is the process of work hardening.

The Work hardening effect is reduced as the strain fields relax due to the availability of thermal energy. This effect is known as thermal softening. The thermal energy results from friction caused by the resistance to dislocation motion through the crystal lattice. Hence work hardening increases the rate of thermal softening and thermal softening decreases the rate of work hardening. For most cases of tensile deformation the two effects operate simultaneously and tend towards a state of dynamic equilibrium. Uniform deformation cannot continue past this point as the rate of thermal softening exceeds the rate of work hardening, the deformation becomes unstable and necking is initiated. The necked region acts as a

stress concentrator due to its reduced cross sectional area. Deformation occurs predominantly in this region and the material subsequently fails: this is geometric softening.

Failure occurs in a perfectly plastic material when the reduction in area of the necked region is 100% *ie.* the material has drawn to a perfect point. Defects in real materials prevent this due to the formation of voids or cracks. Where many dislocations pile up at an obstacle, the sum effect of their strain fields may result in brittle fracture or in the plastic deformation of more ductile materials - this results in the formation of a void around the obstacle. Both these effects can occur during uniform deformation, prior to the onset on necking. The formation of cracks may lead to catastrophic failure before the materials potential for uniform deformation is reached. Void formation is more likely to induce geometric softening and reduce the elongation to failure. Voids in pure metals can also initiate and grow along dislocation cell walls. Therefore materials with small dislocation cells are likely to contain a fine dispersion of small voids. In contrast, materials with a large dislocation cell size may develop large voids, the presence of which will result in geometric softening and reduced ductility.

At low strain rates other failure modes may operate due to vacancy migration. This is not considered potentially significant at high strain rates due to the limited rate for diffusion.

#### 2.3.2.1 Dislocation Glide

The most significant deformation mechanism for large strains at high strain rates is that of dislocation glide. When the applied stress or the thermal softening is sufficiently high, the range over which dislocations are able to glide continuously through the crystal lattice is significantly increased.

#### 2.3.2.2 Dislocation Cells

Dislocation cells, or subgrains, are formed within individual grains and consist of dislocation free regions separated by walls of high dislocation density. The size of these cells is found to be related to the size of voids formed during ductile deformation and fracture. As the dislocation

cell size decreases the void size also decreases and the materials ductility increases - Vecchio [37]. It would be anticipated that with decreasing stacking fault energy of a pure material, the size and extent of voids would decrease because stacking fault energy is a critical parameter in the formation of dislocation cells. The stacking fault energies for some pure metals are given in Table 2.3.

Pure metal	Stacking fault energy ( $\text{mJ m}^{-2}$ )
Aluminium	200
Copper	80
Gold	50

Table 2.3: Typical stacking fault energies for pure face centre cubic metals, from Dieter [38]

It is known that superplastic materials form subgrains, whether they are formed by dislocations moving by climb or glide is not known. However, subgrain formation causes small volumes of a crystal to become reoriented with respect to each other: a process analogous to the larger scale reorganisation of grains associated with superplastic flow - Section 2.3.1.2.

An attempt has been made to consider how subgrain formation could form the basis of a deformation mechanism capable of operating at high strain rates. Dieter [39] and Holtzman [40] found that shock loaded materials form subgrains and that as the magnitude of the shock is increased the size of the subgrains is reduced. It was also found that the smaller subgrains have more tightly packed dislocation walls. The shock experienced by a shaped charge liner is very severe and from this it may be anticipated that the subgrains would be very small and their walls of very high dislocation density. This may result in the formation of adiabatic shear bands. These are regions of very intense shear which operate at a high temperature. The surrounding material remains virtually undeformed and does not experience the increased in temperature.

The existence of these phenomena has not yet been verified in recovered slug or jet material. It is likely that thermal effects occurring after

high speed deformation has taken place, such as heating of the material due to air resistance while in flight, would anneal out any such regions of high dislocation density and cause grain growth. It is interesting to note that Jamet [17] reported the grain size of recovered slug material to be about  $20\mu\text{m}$ . This grain size was also observed in captured jet material described in Section 5. In both cases the original liner material had an initial grain size of  $\geq 300\mu\text{m}$ .

Chokshi and Meyers [35] have considered the possibilities for dynamic recrystallisation. This involves the development of a dislocation cell structure and the transformation of low angle grain boundaries to high angle grain boundaries during plastic deformation. The process is repeated continually during deformation, resulting in a steady state recrystallised grain size,  $d_s$ . They have used a relationship developed by Derby and Ashby [41] which relates the steady state grain size to the strain rate

$$d_s \propto \dot{\epsilon}^{-\frac{1}{2}} \quad (2.14)$$

Using an empirical route they estimated the value of  $d_s$  at high strain rates. This they then compared to the theoretical value of grain size required for diffusion controlled superplasticity at similar strain rates - Table 2.2. The values were of a similar magnitude and from this they deduced that superplasticity resulting from dynamic recrystallisation was a potential mechanism for very high strain rate deformation.

Although an interesting analysis, some of the numerical values used by Chokshi and Meyers are questionable. Of particular concern is the critical value for  $d_s$  at high strain rates. The method they describe for finding this value uses a graphical extrapolation on a limited amount of data.

### 2.3.3 Twins

Twinning, as mentioned in Ashby's summary of deformation mechanisms, is a perfectly valid form of deformation. However, twins are normally only able to account for 5% to 10% strain. The limited deformation accounted for by this mechanism is as a result of their highly ordered nature. A unit of deformation is required to operate over many adjacent atomic layers of the metal crystal. For a given crystal structure

this process takes place only on certain sets of lattice planes and only in preferred directions.

The occurrence of twinning in impact loaded material - see also Section 2.4.1.1 - should not be confused with the deformation processes that may occur during the collapse of a shaped charge liner. A twin may be generated as the by-product of some other deformation mechanism, such as special cases of dislocation motion. However, twinning is not considered to be a primary deformation mechanism in shaped charge jetting.

## 2.4 Testing and Characterisation of Materials

### 2.4.1 High Strain Rate Testing

The mechanical testing of materials at high strain rates is dominated by Hopkinson's bar techniques. Hopkinson originally developed the use of long metal rods to store and transfer pressure pulses to deformation samples. The apparatus was originally intended for experiments with the samples in compression. Slight re-arrangement of the experimental set-up allows tensile and torsion testing to be carried out. There are currently over fifty different versions of the Hopkinson pressure bar. Although the basic principle of all tests remains the same, considerable advances have been made following developments in instrumentation technology.

A version of the Hopkinson - Kolsky [42] bar developed by Field [43] and operating in the torsion mode has produced the highest reported strain rates to date - approximately  $10^5 \text{ s}^{-1}$ . The stress, strain and strain rate data obtained from these tests is made very difficult to interpret due to the high inertia of the test apparatus. It is also difficult to determine the stage at which the deformation becomes steady state, *ie.* when the inertia effects have been overcome. Figure 2.4 (from Blazynski [44]) compares typical stress - strain curves for commercial purity aluminium at shear strain rates from  $600 - 2800 \text{ s}^{-1}$ . A significant increase in flow stress with strain rate is observed. Note that only the specimens tested at the highest and lowest rates were strained to failure. Although no other details of the stress/strain relationship are discussed, Figure 2.4 would appear to indicate an increase in the rate of work hardening. At any given value of shear strain the gradient of the stress versus strain curve appears to increase with increasing nominal shear strain rate.

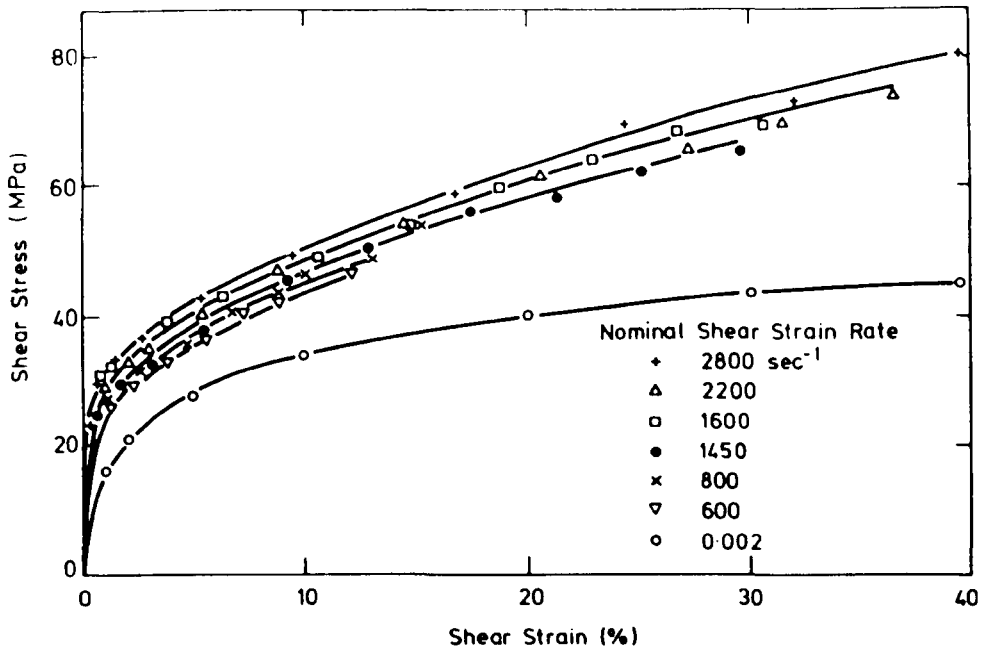


Figure 2.4: Effects of strain rate on the stress - strain response of aluminium under torsional loading. Blazynski [44]

Harding [45] has suggested a change in deformation mechanism occurs at strain rates above about  $10^3 s^{-1}$ . Below this strain rate, the dislocation deformation mechanisms are quite well known. At the higher rates Harding proposed that the dislocations are energetic enough not to require thermal activation in order to glide through the crystal lattice. Evidence to support this theory is at present though very limited and inconclusive.

#### 2.4.1.1 Shock Loaded Material

As it is difficult to examine material from shaped charges after their detonation, there have been several studies of material explosively shock loaded under conditions where recovery is easily achieved. Essentially this involves loading a sheet of material with a plane wave shock. Producing an explosive shock in a perfect plane wave is difficult but there are good experimental techniques available which are quite successful. These usually rely on the effect of air lenses to bend the detonation wave into a planar wave front.

Dieter [39] has studied various metals and compared the applied shock pressure to changes in their strength, hardness and microstruc-

ture. Holtzman and Cowan [40] have utilised austenitic manganese steel to perform a similar study. Smith and Fowler [46] have made detailed studies of many explosively formed shock phenomena. Of particular interest is a section of their work concerning the microstructural features of copper single crystals with known, different orientations in respect of the shock wave. Fine deformation twins were formed in these materials.

In all cases shear bands were observed near the surfaces where the shock loading was applied. Throughout the remaining material the twin spacing became increasingly fine with increasing distance from the shocked surface. This indicates decreasing strain with increasing distance. It is hypothesised that the twins were created as part of a mechanism for absorbing large deformation energies without the requirement for large localised strains. The latter case would involve the material overcoming large inertia. At the surface where the shock loading was applied, twinning was insufficient to absorb all the deformation energy and gross deformation occurred through the formation of shear bands.

An interesting anomaly occurs for one of the high purity copper crystals tested by Smith and Fowler. This was tested with the  $\langle 100 \rangle$  direction aligned parallel to the direction of the applied shock load. No twins were observed in this crystal probably because slip occurred preferentially on the  $\{111\}$  planes. In this particular orientation the six sets of  $\{111\}$  planes would be symmetrically distributed about the  $\langle 100 \rangle$  direction axis. The angle made between the normals to these planes and the axis is  $54.74^\circ$  while the angle between the  $\langle 110 \rangle$  directions and the axis is either  $45^\circ$  or  $90^\circ$ . The combination of these plane orientations and the  $\langle 110 \rangle$  directions at  $45^\circ$  to the axis is nearly ideal for slip to occur at the minimum resolved shear stress. The Schmidt factor was  $S\mathcal{F} = 0.408$ . This parameter has a value in the range  $0.0 \rightarrow 0.5$ . The higher the Schmidt factor, the lower the critical resolved shear stress for a particular slip system.

$$S\mathcal{F} = \cos \phi \cdot \cos \theta$$

The Schmidt factor is the product of the cosine of the angle made between the slip direction and the direction of applied force,  $\phi$  and the slip plane normal and the direction of applied force,  $\theta$ .

Johnson and Mitchell [47] were able to observe a body centre cubic (bcc) to face centre cubic (fcc) phase change in shock loaded iron. From

this they were then able to show that a shock wave of very high intensity travelling through a material can cause a change in crystal structure without forming, even transitory, amorphous material. This is an interesting observation as it adds weight to the argument for solid jets. Jets have frequently been considered to be liquid, this is embodied by the hydrodynamic models of shaped charges. Johnson and Mitchell's results indicate that explosive loading will not inevitably cause a solid to liquid transformation.

#### 2.4.2 Studies made on Jet Material

Since the earliest investigations of shaped charges, slug material has been available for analysis. In an attempt to learn more of how the jet deforms Hayes and Herling [48] and Zernow [49] [50] [51] have attempted soft recovery of jet fragments. Zernow has reported success in the capture of copper jet fragments. To analyse this material optical and scanning electron microscopy and X-ray analysis by the Debye-Scherer method have been used. The results indicate that the jet is behaving like a tensile specimen. The material has a wire drawing or fibre texture characteristic to material elongated in tension. The lattice spacing was reported to increase by about 5%. Some results show broadening of the diffraction peaks whilst others suggest an increase in the diffraction angle but no broadening of the peaks. It would be expected that if cold work remained in the samples then peak broadening should be apparent.

To avoid the inherent difficulties of fragment capture experiments, there has been considerable effort applied to making X-ray diffractions of jets while in flight. Much of the early work was concerned simply with designing an X-ray system capable of recording a diffraction pattern. This initial study was carried out by Green [52] [53]. Further developments were undertaken by Charbonnier [54], Danzig and Green [55] and Reifsnider and Green [56]. A comprehensive overview of flash X-ray systems is given by Green [57].

Green [52] was the first worker to record diffraction patterns from shaped charge jets. These were made of an aluminium jet using non-monochromatic *ie.* unfiltered - molybdenum radiation. A rather diffuse ring could be discerned in the pattern which could correspond to {200} planes. Liquid metal could also have produced a diffuse diffraction ring

of similar diameter. Due to the poor quality of the image very little other information could be obtained.

Jamet [17] [58] has developed the system to a point where texture analysis of aluminium and copper jets is possible. In the course of the study on aluminium, liners were manufactured from a bar of known texture. Some had their axes parallel to that of the bar and others with their axes perpendicular to it. The texture analysis of the jets in flight was compared and contrasted with the microstructure of recovered slugs and to the liners characteristics as recorded by normal radiographic techniques.

From these results Jamet was able to show that although the initial liner texture does not affect the final jet texture, it does affect its break-up characteristics. The jets were all reported to have the  $\langle 111 \rangle$  directions parallel to their axis, regardless of the original texture of the liner. This is the wire drawing or fibre texture. Those jets resulting from liners where the  $\langle 111 \rangle$  directions were not parallel to the liners axis were reported to break-up earlier and into smaller fragments. In addition, Jamet's results categorically indicated the existence of crystalline jet material.

Other work on texture in shaped charge jets includes that carried out by Schiferl [59] and Wisotzki [60]. Schiferl has carried out a theoretical analysis on titanium hemispherical liners and Wisotzki has patented a method for producing single crystal liners which can be adapted to study preferred orientations and texture. Although neither of these has reported specific relationships between texture and jet break-up, their efforts and those of the other authors cited in this section indicate the considerable interest in this phenomenon.

### **2.4.3 Jetting Characteristics**

In addition to the published literature relating to high speed deformation and shaped charges, there is considerable information held in the form of radiographs taken of previous experiments conducted by Hunting Engineering Limited. These may have been unrelated and quantitatively not comparable but some interesting observations can still be made.

A novel attempt has been made to characterise jets by the fashion in which they break-up. In the following sections three characteristic

break-up modes have been identified and these will be explained in due course. The break-up models and their associated liner materials are summarised in Table 2.4.

Liner Material	Break up Modes		
	Classical	Fractured	Vaporous
Fine polycrystalline Pure Metals	*	*	
Pure Metal Single crystals		*	
Alloys		*	*
Powder Formed Materials			*

Table 2.4: Qualitative classification of jet break-up

The terms “Classical”, “Fractured” and “Vaporous” will be explained in the following text. Each of them is discussed in a separate section where the effect of a liners microstructure on jet characteristics will be examined.

#### 2.4.3.1 Classical Jets

A “Classical” jet has smooth, nearly parallel sides and appears solid in radiographs. Upon break-up, the jet will form into ellipsoidal particles which neck down to a point. These then cease to elongate and continue in flight without further break-up or development of a tumbling motion. In this document the “Classical” jet is used as a standard against which others can be compared - a detailed section from the radiograph of a pure aluminium jet is shown in Figure 2.5.

To date only pure metal liners have resulted in “Classical” jets. “Classical” jets, though, are not always produced by pure metals. Several variables in the liner materials microstructure must all be met simultaneously, otherwise the jet may particulate in a different fashion. The variables which have so far been identified are: material purity and grain

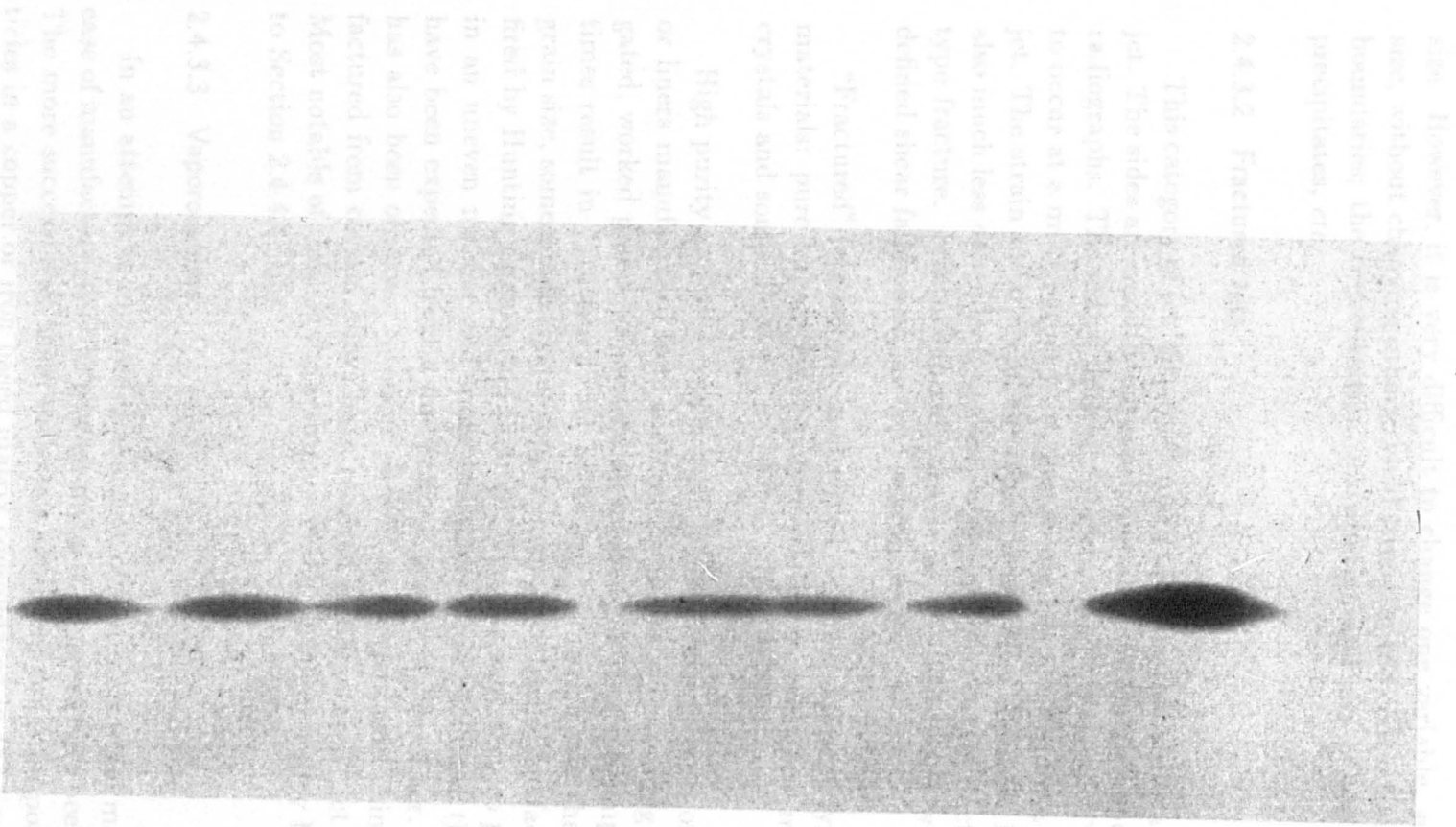


Figure 2.5: Detail from the radiograph of a "Classical" pure aluminium jet

size. However, it is very difficult to change one variable, such as grain size, without changing others: yield strength; the concentration of grain boundaries; the concentration, distribution and size of grain boundary precipitates, *etc.*

#### 2.4.3.2 Fractured Jets

This category of jet initially forms in the same manner as a “Classical” jet. The sides are smooth and nearly parallel, and the jet appears solid in radiographs. The major differences occur upon break-up. This is likely to occur at a much earlier time than would be expected for a “Classical” jet. The strain to failure of the material has been reduced. Break-up is also much less dependent, or completely independent, of ductile necking type fracture. Fracture in this case is usually associated with sharply defined shear failures of the type seen in Figure 2.6

“Fractured” jets have been observed for three different types of liner materials: pure large grained polycrystalline metals, pure metal single crystals and some alloys.

High purity annealed copper with a grain size in excess of  $\sim 100\mu m$  or liners manufactured from high purity material containing very elongated, worked grains - a cold rolled microstructure for example - sometimes result in “Fractured” jet break-up. To investigate the effects of grain size, some single crystal copper liners have been manufactured and fired by Hunting Engineering Limited. The jets were seen to particulate in an uneven manner and more fragments were produced than would have been expected from a fine grained polycrystalline liner. Break-up has also been observed to occur parallel to the jets axis. Liners manufactured from certain alloys have resulted in “Fractured” jet break-up. Most notable of these is the aerospace grade aluminium alloy L168, refer to Section 2.4.4.4.

#### 2.4.3.3 Vaporous Jets

In an attempt to increase the density of materials while maintaining ease of manufacture, various powder metal composites have been studied. The more successful of these materials consist of tungsten powder particles in a copper or iron based matrix consolidated in the liquid phase.

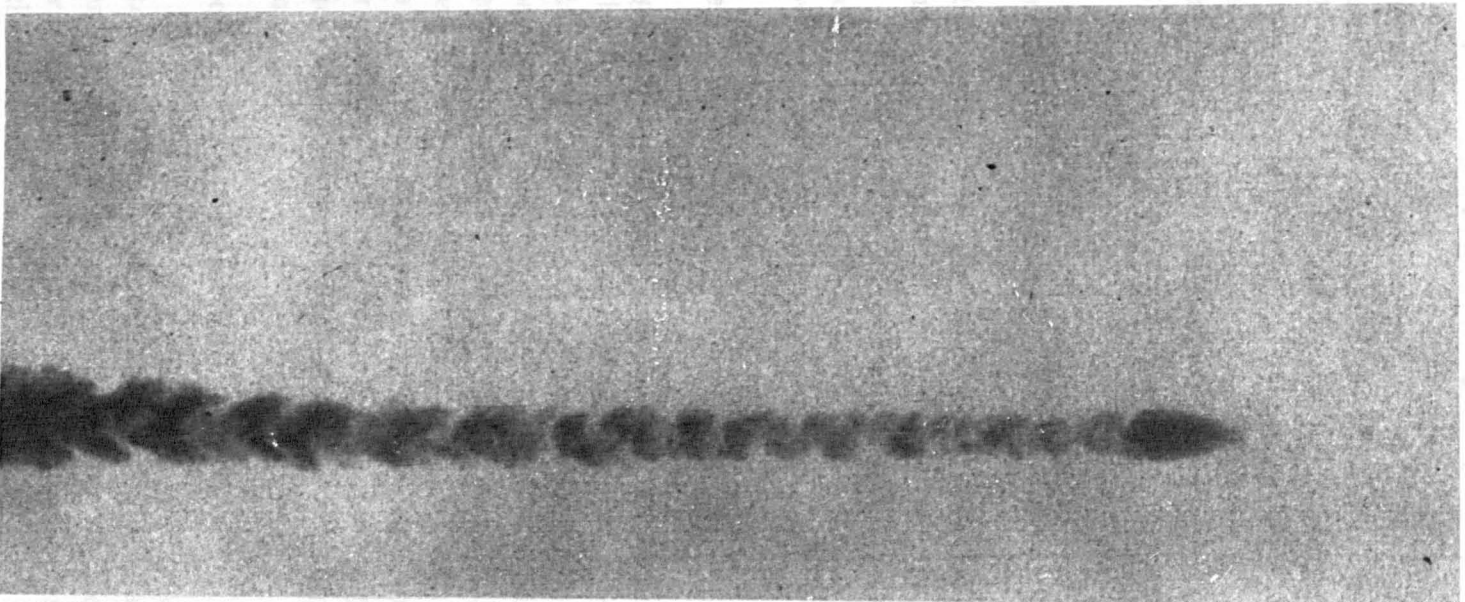


Figure 2.6: Detail from the radiograph of a “Fractured” aluminium alloy jet

This results in a powder composite of very low porosity and, with careful processing, good strength and ductility. The jetting performance of these materials was, though, not as good as had been hoped for. Some problems arose due to the additional mechanical tolerances required for dense materials but the jets had also become unstable. In most cases the jet was in fact a loosely associated cloud of particles. It is suggested that differences in mechanical properties between the particles and matrix resulted in interfacial failures. A radiograph of a jet which had a copper matrix is shown in Figure 2.7. This type of jet is described as "Vaporous".

#### 2.4.4 Materials Properties

There has been little published work in which systematic studies have been made of materials properties in respect to jetting processes. Lichtenberger *et al.* [61] [16] have investigated pure copper, brass and a zinc-aluminium alloy. Their results and the interpretation of them is very interesting, however they are entirely phenomenological.

##### 2.4.4.1 Copper

Lichtenberger's [61] [16] investigation into many commercially pure copper could be interpreted as showing that improved jetting performance was obtained from liners with the lowest recrystallisation temperature. Some batches of copper containing about  $10^{-5}$  (weight percent is assumed) silver impurities were found to have better jetting properties than very pure OFE - oxygen free electrolytic - material. "Better" jetting properties being those which result in the greatest elongation before break-up occurs. Similar quantities of phosphorous or oxygen were found to impair the jet's performance despite the ability of phosphorous to act as a grain refiner.

If a jets performance is improved on some, but not all, occasions by virtue of a low impurity content and a fine grain size, this suggests that other factors are also critical. The precipitates at grain boundaries may be particularly deleterious to a jets performance. Phosphorous and oxygen will form precipitates on grain boundaries whereas silver is able to go into solid solution.

2.4.4.2 Brasses

The study as an investigation of 70% copper 30% (α + β) brass. Several interest to remove the structure of the recrystallized grain - grain

The result best hole - there caused the for pure copper stress relieved tion of particle the "Fracture"

2.4.4.3 Zinc

The zinc a bccoid copper have superplastic carefully control a lamellar form to be obtained pure, 350°C underlined and

It was found a considerable to hydrogen gas between the zinc particles micro give good charac

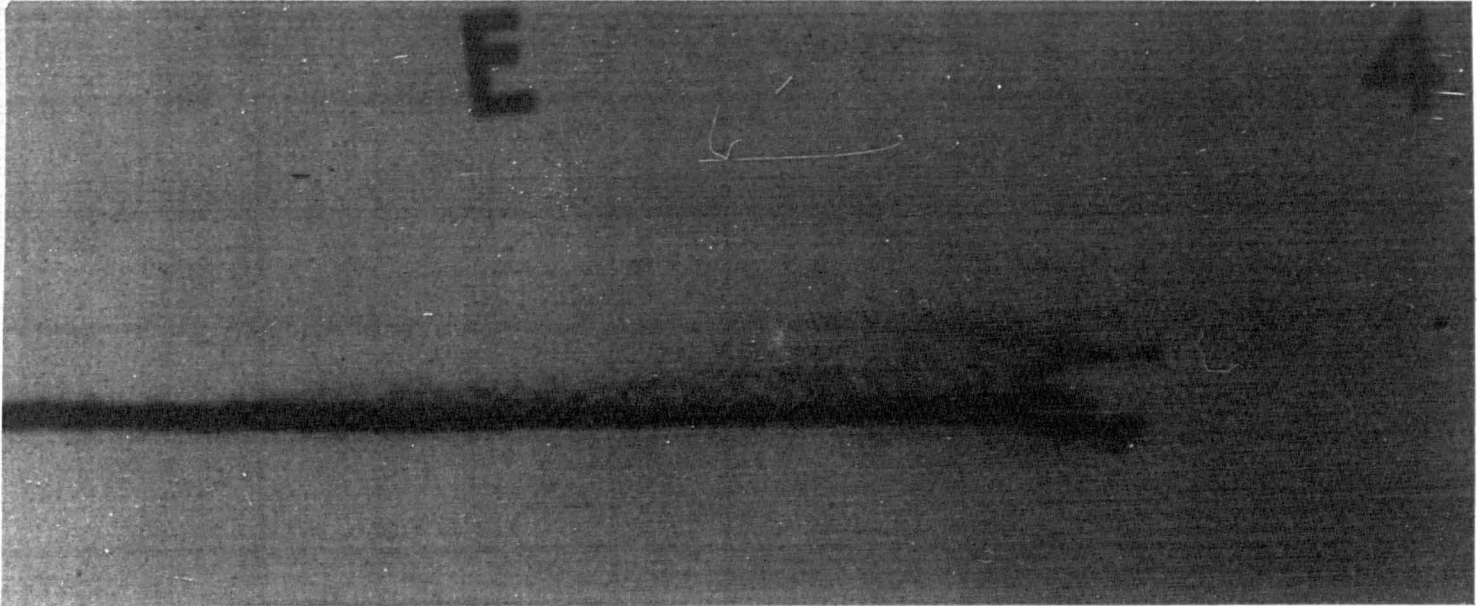


Figure 2.7: Detail from the radiograph of a "Vaporous" tungsten particle, copper matrix powder metal jet

#### 2.4.4.2 Brasses

The study of brasses by Lichtenberger *et al.* [61] was made primarily as an investigation of grain size. Two alloys were used: a single phase 70% copper 30% zinc  $\alpha$  - brass and a double phase 60% copper 40% zinc ( $\alpha + \beta$ ) brass. These were thermally manipulated to produce three different microstructures in each alloy: One was given a recovery treatment to remove residual stress but still maintained the heavily worked microstructure of the original material. A second was treated at just above the recrystallisation temperature to produce a fine -  $5\mu m$  - grain size and the third treated at high temperature to produce a coarse - approximately  $30\mu m$  - grain size.

The results showed the fine grained microstructure to produce the best jets - those with the greatest penetration performance. Brittle fracture caused these jets to break-up earlier and into more fragments than for pure copper. Jets with large or highly deformed grains - even in the stress relieved state - break-up incoherently, *ie.* there is a radial dispersion of particles. These jets appeared to be on the borderline between the "Fractured" and "Vaporous" modes of break-up.

#### 2.4.4.3 Zinc - Aluminium

The zinc aluminium alloy used by Lichtenberger [61] was of monotectoid composition, 78wt% zinc 22wt% aluminium. This is known to have superplastic properties at low rates of strain if its microstructure is carefully controlled. In this study three microstructures were developed: a lamella form produced by slow cooling from the  $\alpha'$  phase, a spinodal form obtained by rapid quenching from the solution treatment temperature,  $350^{\circ}C \rightarrow 0^{\circ}C$ , and the superplastic form which was obtained by an undefined annealing treatment on the spinodal microstructure.

It was found that if the rate of cooling from the molten state was low, a considerable amount of microporosity appeared. This was attributed to hydrogen gas coming out of solution and to differential shrinkage rates between the zinc and aluminium rich phases. The presence of microporosity caused a decrease in the elongation performance of the jet. When non porous microstructures were tested, all three variants were reported to give good elongation performance. The lamella microstructure resulted

in the best performance.

The ability of this alloy to produce good jets is surprising as it was anticipated that the presence of a second phase, each phase having different mechanical properties, would complicate the deformation process and cause early break-up. Close examination of the results indicates that Lichtenberger had assessed performance in terms of penetration. The zinc - aluminium jets were in fact characterised by "Fractured" break-up, resulting in many small fragments at an early time. The apparently high penetration performance was a result of a greater mass of material. Accounting for the difference in density and using the standard geometry described by Lichtenberger, the zinc - aluminium liners were equivalent to 1.2 mm thick copper. The copper liners used for comparisons were 1.0 mm thick.

Additions of approximately 2wt% copper to the zinc - aluminium alloy resulted in the formation of "Vaporous" jets. It is suggested that this was due to the formation of copper precipitates in the aluminium rich phase of the alloy.

Considerable interest has been expressed in these materials because of their "superplastic" properties. This has possibly been without consideration for the special conditions required for materials to exhibit this phenomenon. Under high strain rate conditions these materials cannot exhibit superplastic properties unless their grain size is very small - see Section 2.3.1.1. Grain sizes sufficiently small to allow superplastic properties at the rates of strain required for jetting are not currently attainable. The two phase microstructure of zinc - aluminium alloy may be ostensibly equivalent to the matrix/particle or particle/particle structure of powder metals.

#### 2.4.4.4 Aluminium

Commercially pure aluminium liners have been fired by Hunting Engineering Limited. These produced "Classical" jets consisting of elongated ellipsoidal particles and a slug. Relative to firings of copper liners, very few aluminium liners have been fired and there is not as yet sufficient data to indicate whether they are as sensitive to trace impurities or metallurgical properties such as grain size.

Recently some aluminium alloy liners were tested. These were manufactured from aerospace alloy L168. This is a high strength aluminium - copper - magnesium alloy. Its mechanical properties can be developed primarily by heat treatment which produces precipitate strengthening. Jets of this material are seen to break-up almost instantaneously by a process of brittle fracture. There were many more occurrences of fracture and therefore more jet fragments than would have been observed for a pure aluminium jet. The jets profile was that of a chevron and the usual slug section was not fully formed.

## CHAPTER 3

# Investigation of Liner Materials

### 3.1 Introduction

The aim of the experiments described in this chapter was to study the effect of the liner material on jet break-up. Aluminium was chosen as the base material for most of this work. By varying the amounts and type of alloying additions the mechanical properties could be varied considerably. The strongest alloy used had nearly six times the tensile strength of annealed, pure aluminium. Firings were also carried out with copper liners for comparative purposes.

The practical details relating to the firings are described in this chapter whilst some information pertaining to methods of laboratory analysis has been placed in Appendix B. The design drawings and assembly procedure for the warheads are presented in Appendix A.

#### 3.1.1 Experiments With Aluminium Liners

From previous research by Hunting Engineering Limited, it was known that pure aluminium liners would produce "Classical" jets and that certain aluminium alloys would produce "Fractured" jets. The experiments described in this thesis using aluminium were designed to test a range of materials between these two extremes. Pure aluminium is discussed initially (1000 series), this is followed by the non - heat treatable aluminium - magnesium (5000 series) alloys and then the precipitate strengthened aluminium - copper - magnesium (2000 series) alloys. This provides the basis of a structured series of experiments which progressively move upward in terms of the liner materials strength. Three types

of aluminium were selected: pure aluminium was chosen specifically as a low strength, high ductility material, aluminium - magnesium alloys were used because of their capability for showing increasing amounts of work hardening as the magnesium content rose, and aluminium - copper - magnesium alloys were selected since they could be heat treated to provide a range of mechanical properties. The density of all these materials was approximately constant. All these firings used the same design of shaped charge, thus the only variables were the material properties of the liner.

### **3.1.2 Experiments With Copper Liners**

As copper is probably the most commonly used liner material for commercial shaped charges it was used to allow comparisons to be made with aluminium. To accommodate the difference in density it was decided that an equal mass of material should be used and this meant that the copper liners had to be made considerably thinner. Major changes in the design of the shaped charge were undesirable as this would make comparison harder, but some minor modification was inevitable.

Two experiments were conducted using copper liners where the aim was to capture jet material in a condition as close as possible to that of the jets in flight. This captured material was then subjected to laboratory analysis.

### **3.1.3 Experimental Data**

The materials used to manufacture liners described in this chapter are described in Table 3.1. This table also relates each material to a unique firing reference number with which each experiment was identified.

When the firings were carried out the X-ray units were pulsed at specific times after the initiation of the detonator. This event was recorded by a probe placed between the detonator and the booster pellet, see Figure A.6. The recorded values are given in Table 3.2.

Firing reference	Alloy designation		Heat treated condition of liner at firing
	BS	ISO	
<b>Pure Aluminium</b>			
Al-M	E1B	1050 A	As-manufactured
Al-O	E1B	1050 A	Annealed
Al-⊥	E1B	1050 A	As-manufactured <sup>(1)</sup>
Al-	E1B	1050 A	As-manufactured <sup>(2)</sup>
<b>Non heat treatable aluminium alloys</b>			
A	NE4	5251	As-manufactured
B	NE5	5154	As-manufactured
C	NE5	5154	As-manufactured
D	NE8	5083	As-manufactured
<b>Precipitate strengthened aluminium alloys</b>			
QU		2014	As quenched
T6	L168	2014	T6511
NA		2014	Naturally aged
SC		2014	Slow cooled
<b>Pure Copper</b>			
Cu-M	C106		As-manufactured
Cu-O	C106		Partially annealed

Table 3.1: Materials used for investigation of shaped charge liners.

“As-manufactured” indicates the material is in the condition specified by its designation and has received no mechanical or heat treatment following its extrusion (or rolling in the case of the C106 copper). The heat treated conditions of firing references QU, NA, SC, Al-O and Cu-O were applied specifically for the purposes of this investigation, details are given in the following sections.

- (1) Liner axis perpendicular to extrusion direction
- (2) Liner axis parallel to extrusion direction

Reference	X-ray times ( $\mu s$ )				Figure
	$X_1$	$X_2$	$Y_1$	$Y_2$	
Pure Aluminium					
Al-M	53.5	103.3	154.3	<b>179.4</b>	4.9
Al-O	53.7	103.6	154.6	<b>179.6</b>	4.10
Al- $\perp$	52.2	102.0	150.9	<b>180.9</b>	4.11
Al- $\parallel$	N/A	102.1	151.0	<b>181.0</b>	4.12
Non heat treatable aluminium alloys					
A	49.4	99.7	150.5	<b>179.5</b>	4.23
C	51.3	101.4	152.4	<b>181.4</b>	4.25
B	49.3	99.3	150.3	<b>179.4</b>	4.24
D	49.4	99.5	150.3	<b>179.5</b>	4.26
Precipitate strengthened aluminium alloys					
QU	35.9	51.0	71.0	<b>91.0</b>	4.36
T6	50.2	61.0	81.3	<b>100.1</b>	4.37
NA	50.4	61.2	81.5	<b>100.3</b>	4.38
SC	50.1	60.9	81.2	<b>100.0</b>	4.39
Pure Copper					
Cu-M	50.0	150.3	180.9	<b>200.0</b>	4.45
Cu-O	51.0	151.2	181.5	<b>200.9</b>	4.46

Table 3.2: Time delays for radiograph images relative to initiation of detonation.

The radiographs produced at those times in bold type are presented as figures in Chapter 4.

## **3.2 Commercially Pure Aluminium**

### **3.2.1 Experimental Details**

Four experiments were to be carried out with aluminium. This material was of a commercial grade and was 99.5% pure. Given the experience of previous firings of commercially pure aluminium by Hunting Engineering Limited, it was felt that there was no reason to pursue exceptionally high purity material. A “Classical” jet would result which would eventually form into elongated ellipsoidal fragments.

The experiments were required to investigate differences in grain morphology induced by mechanical work. Two firings were made using material in the as-manufactured condition and in the annealed condition. The other two firings were carried out using material in the as manufactured condition but with different grain alignments relative to the extrusion direction.

### **3.2.2 Material for the Manufacture of Liners**

Two batches of material were available, these were both of designation E1B M. The condition and chemical composition of this material is as follows;

- E, designates an extrusion
- 1B, designates material with a minimum purity of 99.5% aluminium
- M, designates material in the “as-manufactured” condition: *ie.* no subsequent heat treatment has been applied following extrusion.

The chemical composition of the material is given in Table 3.3. The British Standard for material of composition 1B is synonymous with that for ISO designation 1050 A.

### **3.2.3 The Shaped Charge Liners**

Four liner blanks were cut from the bar stock to the design shown in Figure A.4. One of these was machined with its axis perpendicular to the

Element	Max wt%
Silicon	0.25
Iron	0.4
Copper	0.05
Manganese	0.05
Magnesium	0.05
Zinc	0.07
Titanium	0.05
Others: each	0.03
Aluminium	Remainder (Min 99.5 %)

Table 3.3: Nominal chemical composition of E1B M/1050 A aluminium.

extrusion direction. The axis of the remaining three liners was parallel to the extrusion direction.

One liner blank, with its axis parallel to the extrusion direction, was annealed at  $505 \pm 5^\circ\text{C}$  for 45 minutes in an air circulation furnace. At the end of this period the furnace was switched off and the part allowed to cool overnight. The liner blank was now in the annealed, E1B O, condition. The surface of the liner blank had become heavily oxidised during the heat treatment. This oxide layer was removed when it was machined to its finished form. The design drawing for this component is shown in Figure A.5.

The remaining liner blanks were to be fired in the as-manufactured condition. These were machined to their finished form without being heat treated - Figure A.5.

### 3.2.4 Firing Conditions

These firings utilised Hunting Engineering Limited's orthogonal firing frame. This structure supported and accurately positioned the warhead such that jets could be fired vertically downwards. This allowed radiographic (X-ray photographic) images of the jets to be recorded from two mutually perpendicular directions. The secondary purpose of the frame was to provide some protection from explosive blast damage to other

items of experimental apparatus. Two pairs of pulsed X-ray units were arranged orthogonally about the frame, each pair facing a film cassette. A Hewlett - Packard Model 730/2710 X-Ray System was used to operate Model 5153 external X-ray tubes which contained tungsten anodes and beryllium windows. This system was able to produce a 30 nanosecond energy pulse. Prior to the explosive firing an exposure was made onto the X-ray film with a grid glass placed in the line of flight of the jet. The grid glass was then removed and radiographs of the jet were made as a second exposure on the same film. The grid glass contains a mesh of reinforcing steel wires the position of which had been accurately measured. The experimental arrangement included a semi infinite target stack into which the jet was fired. The purpose of this material was to absorb and safely contain the jet fragments. A schematic diagram of the experimental arrangement is shown in Figure 3.1 and a photograph an experiment with the grid glass in position is shown in Figure 3.2.

The warheads for firing references Al-O and Al-M were supported with their front face approximately 1600 mm above a steel target. For firing references Al- $\perp$  and Al- $\parallel$  this distance was 1260 mm. These distances - dimension X in Figure 3.1 - were required to make distance calibrations in the radiographic images. The distance from the front face of the warhead to a known position on the grid glass was also required, dimension Y in Figure 3.1. By making measurements of the true grid glass and its radiographic image, the magnification factor for the films could be found. All distance measurements were referenced to an origin at the front face of the warhead.

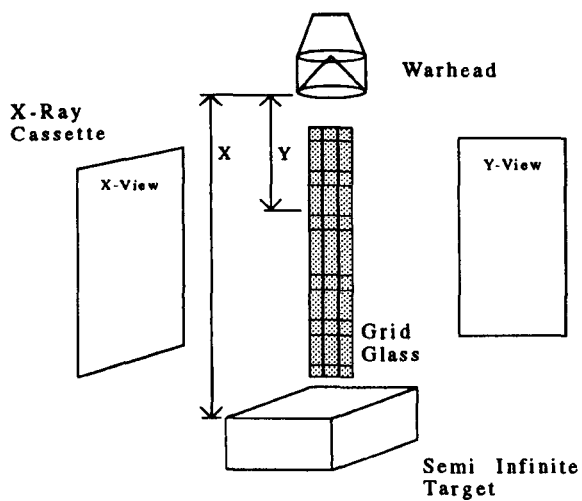


Figure 3.1: Schematic of experimental set-up for vertical firings. In some firings the grid glass was replaced by an alternative means of calibration, however, these worked on similar principles. A photograph of this firing set-up is shown in Figure 3.2

### 3.3 Non Heat Treatable Aluminium Alloys

#### 3.3.1 Experimental Details

An analysis was carried out in order to test for a relationship between the mechanical properties of a shaped charge liner and the resulting jet velocity. Two different aluminium alloys were used. These had similar alloy-chemical proportions, such that the mechanical properties and characteristics - of the liner

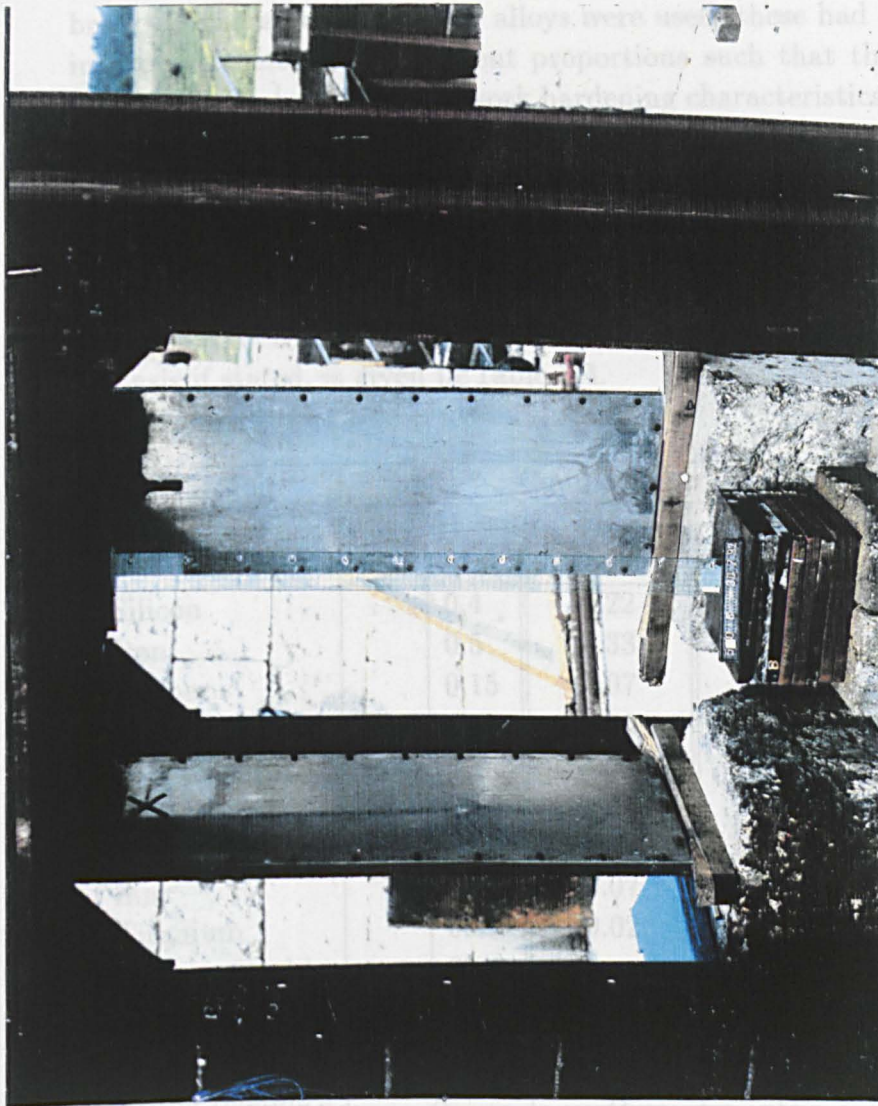


Figure 3.2: Experimental set-up for firing reference Al-L

Table 3.4: Chemical composition of non heat treatable aluminium alloys

### 3.3 Non Heat Treatable Aluminium Alloys

#### 3.3.1 Experimental Details

An analysis was carried out in order to test for a relationship between the mechanical properties of a shaped charge liner and the resulting jet break-up characteristics. Four alloys were used, these had similar alloying constituents but in different proportions such that the mechanical properties - in particular the work hardening characteristics - of the liner material could be varied.

#### 3.3.2 Material for the Manufacture of Liners

The alloys have the following ISO designations; 5251, 5154 (two liners) and 5083. Their composition, nominal or measured by atomic absorption analysis if stated, is given in Table 3.4.

Alloying element	Composition in weight %					
	5251		5154	5154	5083	
	Min	Max	Measured	Measured	Min	Max
Silicon		0.4	0.22	0.19		0.4
Iron		0.5	0.33	0.29		0.4
Copper		0.15	0.07	0.05		0.1
Manganese		0.5	0.26	0.54	0.4	1.0
<b>Magnesium</b>	<b>1.7</b>	<b>2.4</b>	<b>3.24</b>	<b>3.45</b>	<b>4.0</b>	<b>4.9</b>
Chromium		0.15	0.01	0.02	0.05	0.25
Nickel			0.01	0.01		
Zinc		0.15	0.07	0.02		0.25
Titanium		0.15	0.02	0.01		0.15
Others: (each)		0.05		0.05		0.05
Others: (total)		0.15		0.15		0.15
Aluminium	Remainder					
Firing reference	A		B	C	D	

Table 3.4: Chemical composition of non heat treatable aluminium alloys

### **3.3.3 The Shaped Charge Liners**

Four liners were cut from the available bar stock, to the design shown in Figure A.4. Since no heat treatment would be applied to any of the materials they were then machined to their finished form as shown in Figure A.5.

### **3.3.4 Firing Conditions**

The firings utilised Hunting Engineering Limited's orthogonal firing frame. Each warhead was supported with its front face approximately 1600 mm above a steel target. Two pairs of flash X-ray units were arranged orthogonally about the frame, each pair facing a film cassette.

In this respect the set-up was similar to that described in Section 3.2.4. However, instead of using a double exposure technique - where the image of a calibrated grid glass is superimposed over the image of the jet - a solid bar was used to which markers were attached. The spacing between the markers and their position relative to the front face of the warhead were known. The bars were left in place during the firing, adjacent to the line of flight of the jet. This technique required only a single exposure to be made and resulted in an appreciable gain in resolution for the radiographs.

## **3.4 Precipitate Strengthened Aluminium Alloys**

### **3.4.1 Experimental Details**

To investigate the effect of introducing precipitate hardening in the alloy on jet break-up characteristics, a series of experiments was designed to use aluminium alloys in different heat treated conditions. The particular heat treatments were chosen to achieve a wide range in the values for proof stress and ultimate tensile strength (UTS). The aim of the experiments was to obtain radiographs of the jets produced from liners manufactured from these materials. From these images jet break-up data could be extracted for comparison and analysis.

### **3.4.2 Material for the Manufacture of Liners**

Material designated by British Standard L168 [62] was available for the manufacture of four liners. This material was supplied in the T6511 condition. The BS L168 designation specifies the materials composition in terms of ISO designation 2014 A. This is listed in Table 3.5. The condition, including heat treatment, required for the material to conform to this designation is as follows;

#### **L168-T6511**

- **Solution Treatment**

The solution treatment shall consist of heating at a temperature of  $505 \pm 5^\circ\text{C}$  and quenching in water at a temperature not exceeding  $40^\circ\text{C}$ .

- **Controlled stretching involved in a straightening operation**

- **Artificial Ageing**

Artificial ageing shall consist of heating at a temperature of  $175 \pm 5^\circ\text{C}$  for 5 hours to 12 hours.

### **3.4.3 The Shaped Charge Liners**

Four liner blanks were cut from the L168 bar stock. These were manufactured to the design shown in Figure A.4. One liner blank in the

Alloying element	Composition <i>wt%</i>	
	Min	Max
Silicon	0.5	0.9
Iron		0.5
Copper	3.9	5.0
Manganese	0.4	1.2
Magnesium	0.2	0.8
Chromium		0.1
Nickel		0.1
Zinc		0.25
Titanium		0.15
Titanium + Zirconium		0.2
Others: (each)		0.05
Others: (total)		0.15
Aluminium	Remainder	

Table 3.5: Nominal composition of precipitate strengthened 2014 - L168-T6511 aluminium alloy

L168-T6511 condition was machined to its finished form. This components design is shown in Figure A.5.

The three remaining liner blanks were solution heat treated to remove the effects of the artificial ageing carried out on the L168-T6511 material. This solution treatment was carried out at  $505 \pm 5^\circ\text{C}$  for 45 minutes in an air circulation furnace. The liner blanks were then given one of the following heat treatments;

- Quenched in water, machined to the finished form and then naturally aged at room temperature for a period of 1624 hours before firing.
- Quenched in water, then in liquid nitrogen and held at this temperature. Throughout the machining process a mixture of liquid nitrogen and methanol was used as both a lubricant and coolant. The finished liner was then stored in dry ice until about 15 min-

utes before firing in order to preserve as near as possible the “as quenched” heat treated condition.

- Left in the furnace after its solution heat treatment and the temperature controller reset to 200°C. After 3½ hours the furnace had stabilised at this temperature. The furnace was then switched off and allowed to cool overnight. The liner blank, now in the “slow cooled” condition, was then machined to the finished form.

#### **3.4.4 Firing Conditions**

The firings utilised Hunting Engineering Limited’s orthogonal firing frame. The warhead was supported with its front face approximately 1200 mm above a steel target. Two pairs of flash X-ray units were arranged orthogonally about the frame, each pair facing a film cassette. Lead markers were attached to the cassettes to act as distance markers. By making measurements of the experimental geometry these distance markers could be used to find a magnification factor for the films and thus calibrate the resulting radiographs.

## 3.5 Commercially Pure Copper

### 3.5.1 Experimental Details

An experiment using copper was designed to provide comparative results for the work on aluminium and its alloys.

### 3.5.2 Material for the Manufacture of Liners

The material was supplied in sheet form. Its condition, including heat treatment, is as follows;

- As-manufactured 5mm sheet in the annealed condition was rolled to 3mm thickness
- This material was then annealed at  $505 \pm 5^\circ\text{C}$  for 3 hours

The chemical composition of the alloy was described by the British Standards designation C106. This is a non-arsenical phosphorus deoxidised copper, the full specification is given in Table 3.6.

Alloying constituents	Weight %	
	Min	Max
Copper (inclusive of silver)	99.85	
Phosphorus	0.013	0.05
Total impurities, exclusive of silver, nickel, arsenic and phosphorus		0.060

Table 3.6: Nominal chemical composition of C106 copper.

### 3.5.3 The Shaped Charge Liners

Two circular blanks were cut from the sheet. These were shear spun and given a cold isostatic press (CIP) to reach near net shape. One of the liners was partially annealed by heating at  $400 \pm 5^\circ\text{C}$  for three hours. Finally, the two liners were machined to their finished form as shown in Figure A.8.

### **3.5.4 Design of the Warhead Assembly**

This is essentially as described for warheads with aluminium liners but utilising a modified liner and locking ring. The copper and aluminium liners had equal mass and therefore to compensate for the higher density of copper these liners were much thinner (1.2 mm as opposed to 7.0 mm). The modified locking ring is shown in Figure A.7 and the modified liner in Figure A.8.

It was anticipated that by keeping the mass of liner material constant the jets velocity characteristics would be similar for aluminium and copper. Any differences would be manifest in the jets velocity gradient.

### **3.5.5 Firing Conditions**

The firings utilised Hunting Engineering Limited's orthogonal firing frame. The warhead was supported with its front face approximately 1200 mm above a steel target. Two pairs of flash X-ray units were arranged orthogonally about the frame, each pair facing a film cassette. Prior to the explosive firing an exposure was made onto the X-ray film with a grid glass placed in the line of flight of the jet, radiographs of the jet were made as a second exposure on the same film.

## CHAPTER 4

# Results

### 4.1 Introduction

Twelve firings were carried out with aluminium based material and two firings with copper. Images of the jets recorded by flash X-radiography were analysed and quantified in order that their break-up characteristics could be compared. Initially, laboratory tests were made upon the materials from which the liners had originally been manufactured such that their mechanical properties and microstructures could also be compared.

In this chapter the results of these investigations will be presented in tabular and graphic formats. The discussion and interpretation of the results will follow in the next chapter.

Radiographic images recorded by flash X-ray techniques are presented in this chapter. When considering these images it should be appreciated that the jet material was travelling at up to  $6 \text{ mm } \mu\text{s}^{-1}$  - that is six kilometres per second or over twenty thousand kilometres per hour. To achieve still frame images required an exposure time of approximately  $30 \times 10^{-9}$  seconds - thirty billionths of a second. In addition, the photographic process was required to take place in the immediate vicinity of a large explosion.

The digitised images are the result of extensive image analysis carried out for quantitative evaluation of jet fragments. These have been reproduced at a reduced size in order that the entire jet can be seen, this may have resulted in some loss of detail.

## 4.2 Commercially Pure Aluminium

Four firings were conducted using extruded, commercially pure aluminium as the liner material. Three liners were in the as-manufactured condition *ie.* no subsequent heat treatment was applied. This meant that their grain structure was strongly aligned with the extrusion direction. Two of these had been manufactured such that their axes were parallel to the extrusion directions. The third liner was manufactured with its axis aligned perpendicularly to the extrusion direction. The fourth liner had been manufactured with its axis parallel to the extrusion direction, but this was also in the annealed condition.

Orthogonal micrographs of the two grain structures under consideration are shown in Figures 4.1 and 4.2. The grains in Figure 4.1 are clearly elongated as a result of the extrusion process. They also show that recovery and a degree of recrystallisation have occurred due to the elevated temperature at which extrusion is carried out. Subsequent annealing was carried out on some material in order to change its mechanical properties. The yield stress was significantly reduced while other properties remained approximately constant, see Figure 4.3. The change in yield stress resulted from large scale grain growth, from  $30 \times 10\mu m$  to  $300 \times 100\mu m$ , measured in the plane parallel to the extrusion direction. Fine grained materials will generally have a higher yield strength than those with large grains. This is expressed by the Hall - Petch equation

$$\sigma_y = \sigma_0 + Kd^{\frac{1}{2}} \quad (4.1)$$

Where  $\sigma_y$  is the yield stress and  $d$  is the grain size,  $K$  and  $\sigma_0$  are constants.

The tensile mechanical properties for the four variants of these materials are summarised in Table 4.1 - nominal stress, nominal strain values are given. Orientations are denoted by L, longitudinal - parallel to extrusion direction and T, transverse - perpendicular to extrusion direction.

The values plotted in Figure 4.3 show the effect of annealing on stress - strain behaviour. When compared to the annealed material, the as-manufactured material is found to have an increased proof stress, increased UTS and reduced elongation to failure. Figure 4.4 shows the effect of orientation with respect to an aligned grain structure. Tensile tests were made parallel to the extrusion direction and in two other mutually perpendicular directions. Extruded material in the as-manufactured

Firing reference		Proof stress (0.2%) MPa	Ultimate tensile stress MPa	Strain at UTS %	Strain at failure %
Al-M	L	84	94.8	14.1	29.4
Al-O	L	69	87.5	20.8	31.4
Al- $\perp$ M	T	58	76.3	19.6	28.3
Al- $\parallel$ M	L	72	100.8	17.6	29.2

Table 4.1: Tensile properties measured parallel and perpendicular to the extrusion direction in commercially pure aluminium in the as-manufactured and annealed conditions

condition tested parallel to the extrusion direction is plotted in both Figure 4.3 and 4.4. As these materials had been tested under similar conditions the properties might have been expected to have similar values: this was not found to be the case.

Digitised images of the jets are shown in Figures 4.5 to 4.8 and reproductions of the radiographic images are presented in Figures 4.9 to 4.12. The radiographic images are at approximately 110% of their true size. Since all experiments were conducted under similar conditions this figure is virtually constant for all radiographic images in this thesis. Although their appearance differs in detail the general features of the jets are similar. The direction of flight of the jets is from left to right. At the extreme left of the images is the slug which in Figure 4.5 is a single large fragment surrounded by some debris from the explosion. In Figure 4.7 the slug is seen to have broken into two fragments. Immediately to the right of the slug are the remnants of the collapsed liner, this material has not flowed into either the slug or the jet. The true jet extends to the right of this remnant material. The high purity aluminium jets in Figures 4.5 to 4.8 are seen to be continuous for approximately one third of their length, the remaining jet has either partially or fully particulate into long ellipsoidal fragments. At the extreme right, the tip of the jet noticeably larger than other fragments. This "foot" results from non-steady state conditions which exist in the initial stages of liner collapse and jet formation.



$\times 200$   $\overline{100\mu m}$   
 $\times 75$   $\overline{1mm}$

Figure 4.1: Micrograph of extruded commercially pure aluminium in the as-manufactured condition, 1050-M.

The axes of liners manufactured from this material were aligned with the (L)ongitudinal and (T)ransverse directions

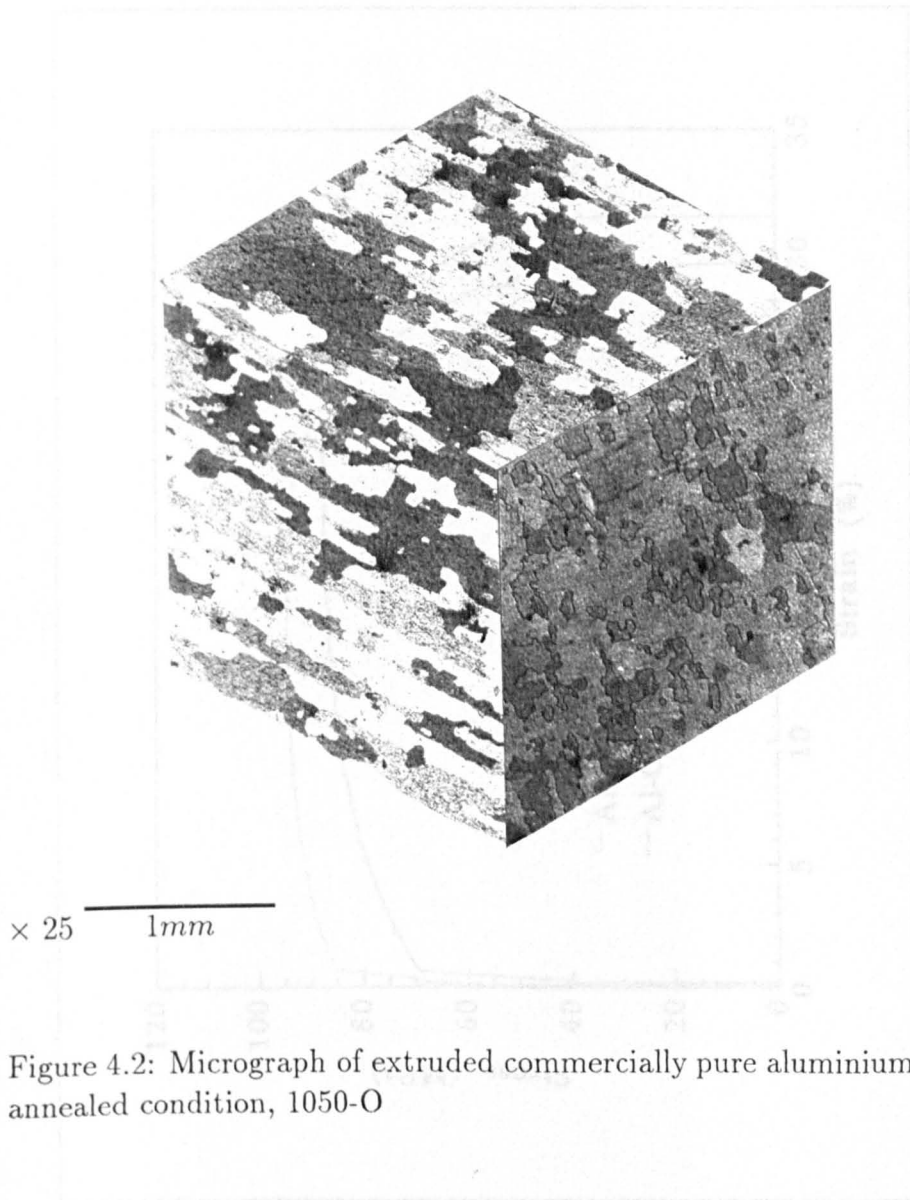


Figure 4.2: Micrograph of extruded commercially pure aluminium in the annealed condition, 1050-O

Figure 4.1: Stress versus strain for extruded commercially pure aluminium

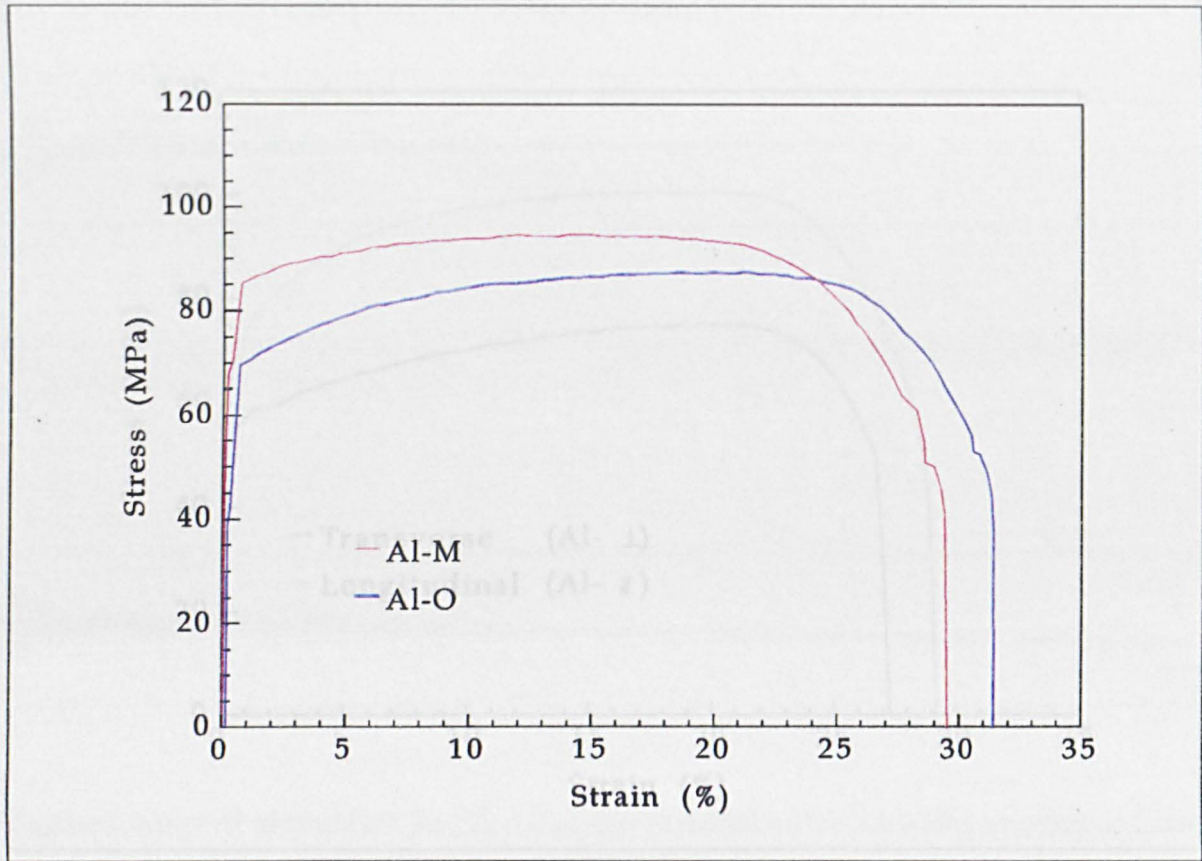


Figure 4.3: Stress versus strain for extruded commercially pure aluminium

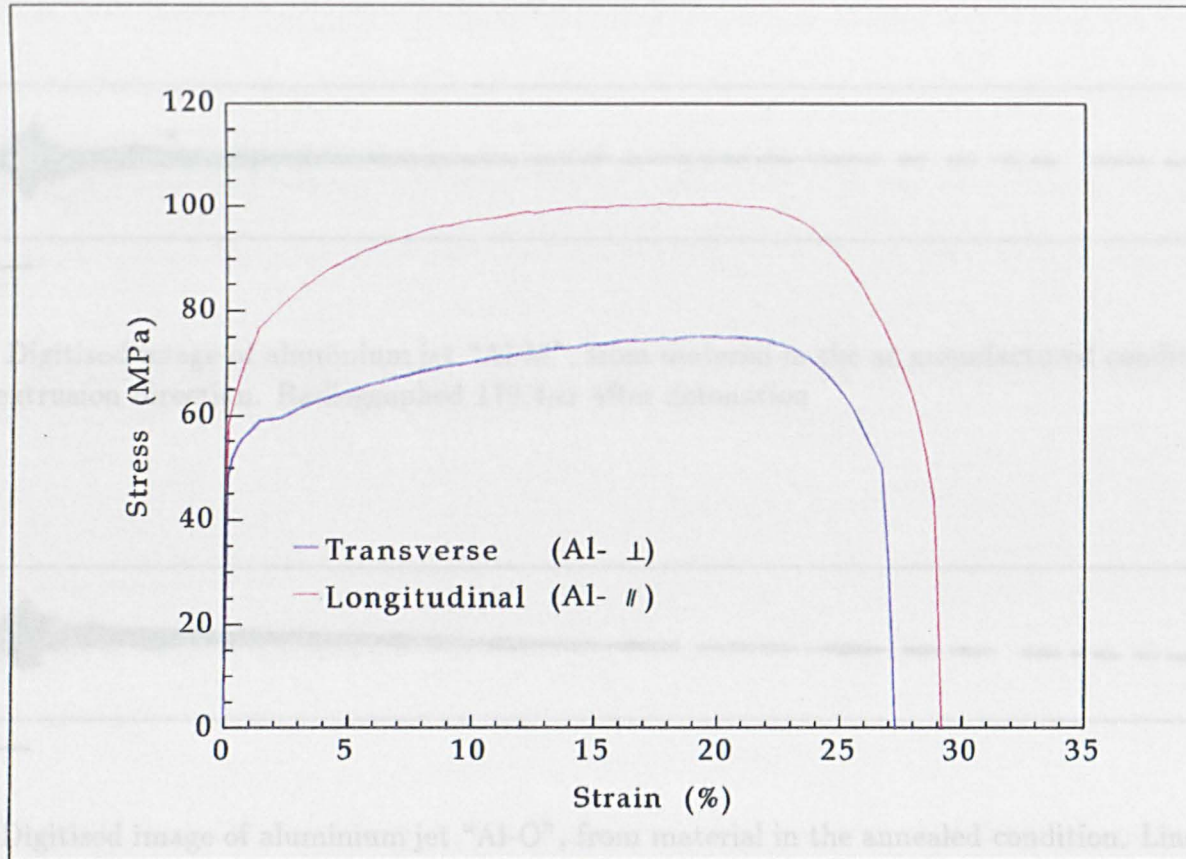
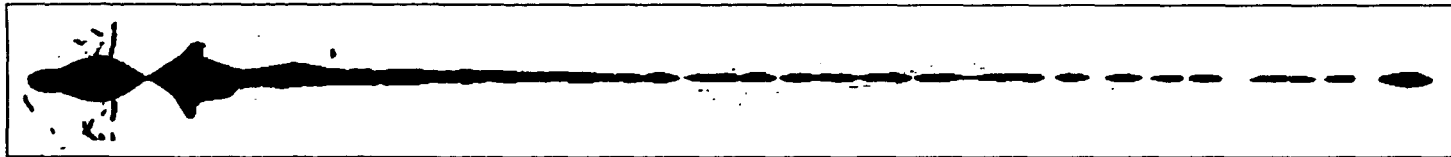


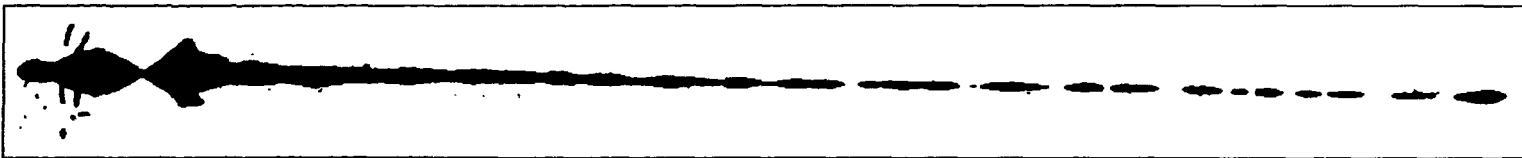
Figure 4.4: Stress versus strain for three mutually perpendicular orientations of extruded commercially pure aluminium in the as-manufactured condition



100mm

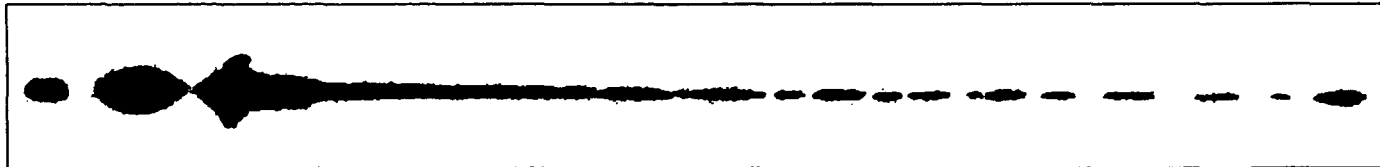
Figure 4.5: Digitised image of aluminium jet “Al-M”, from material in the as manufactured condition. Liner axis parallel to extrusion direction. Radiographed  $179.4\mu\text{s}$  after detonation

69



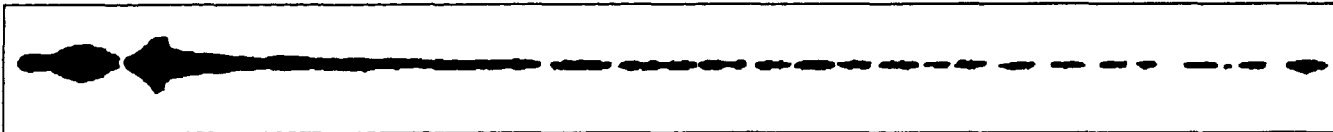
100mm

Figure 4.6: Digitised image of aluminium jet “Al-O”, from material in the annealed condition. Liner axis parallel to the extrusion direction. Radiographed  $179.6\mu\text{s}$  after detonation



100mm

Figure 4.7: Digitised image of aluminium jet "Al-⊥", from material in the as-manufactured condition. Liner axis parallel to the extrusion direction. Radiographed  $180.9\mu s$  after detonation



100mm

Figure 4.8: Digitised image of aluminium jet "Al-||", from material in the as-manufactured condition. Liner axis perpendicular to the extrusion direction. Radiographed  $181.0\mu s$  after detonation

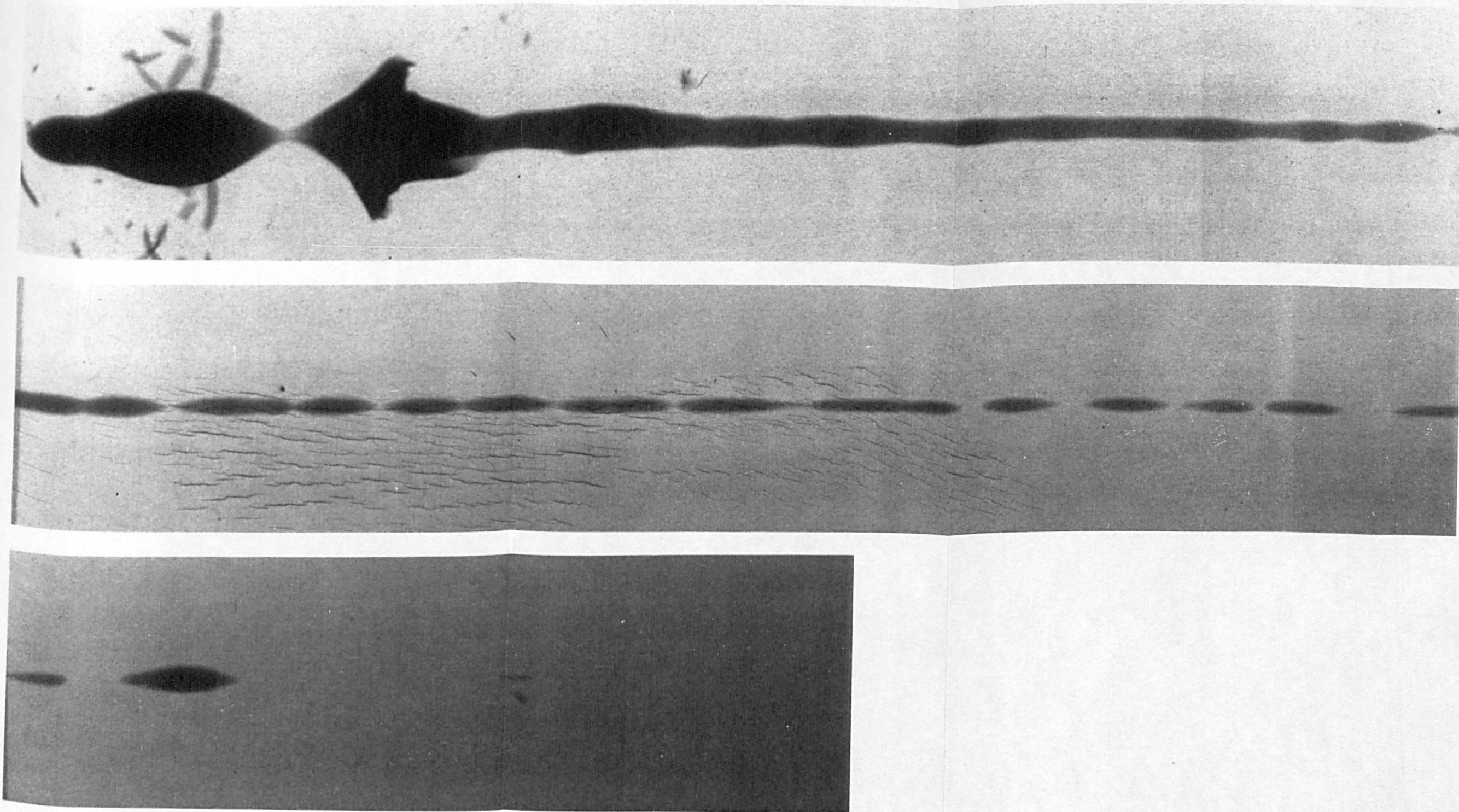


Figure 4.9: Radiograph of aluminium jet "Al-M", from material in the as-manufactured condition. Liner axis parallel to extrusion direction. Radiographed  $179.4\mu s$  after detonation

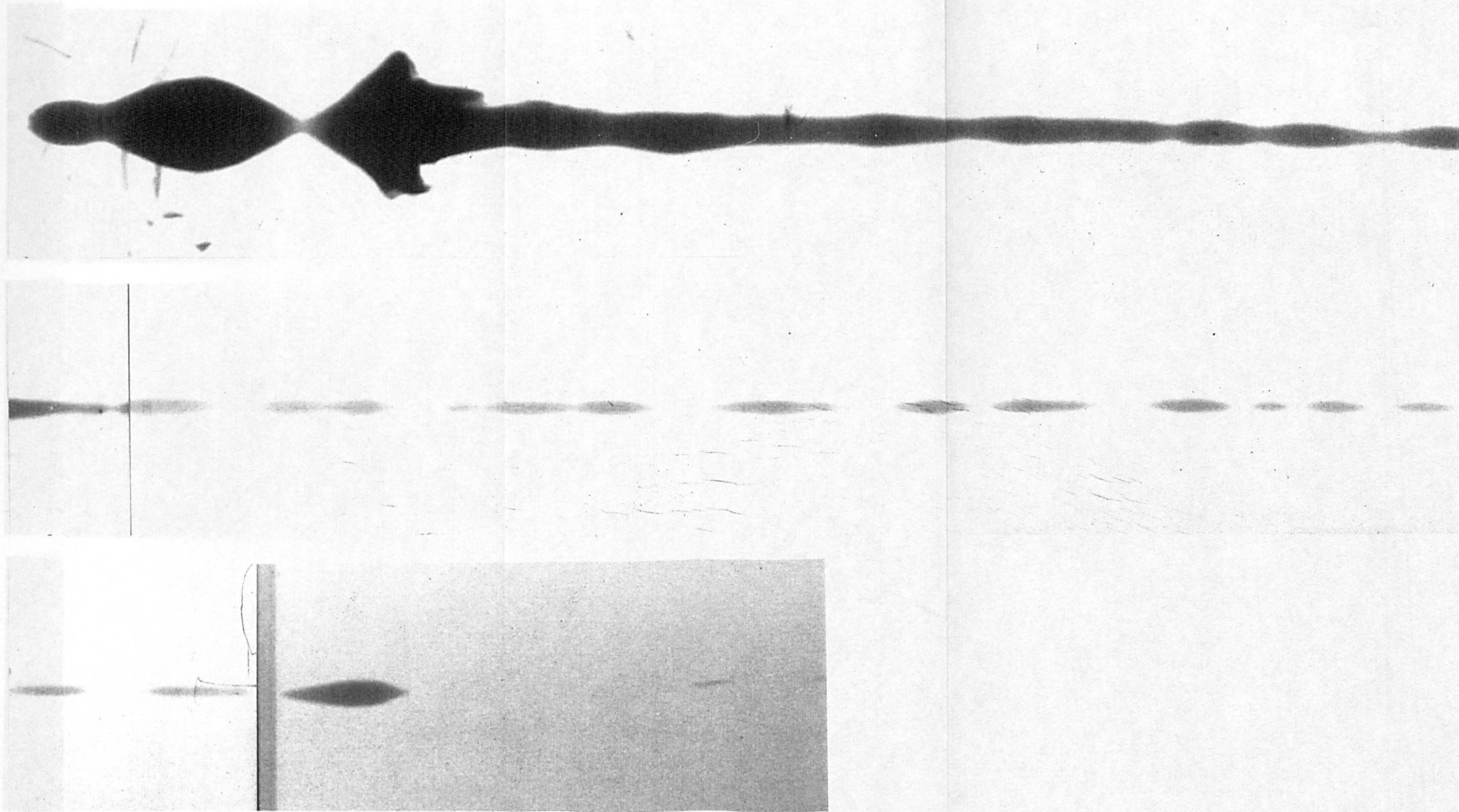


Figure 4.10: Radiograph of aluminium jet "Al-O", from material in the annealed condition. Liner axis parallel to the extrusion direction. Radiographed  $179.6\mu s$  after detonation

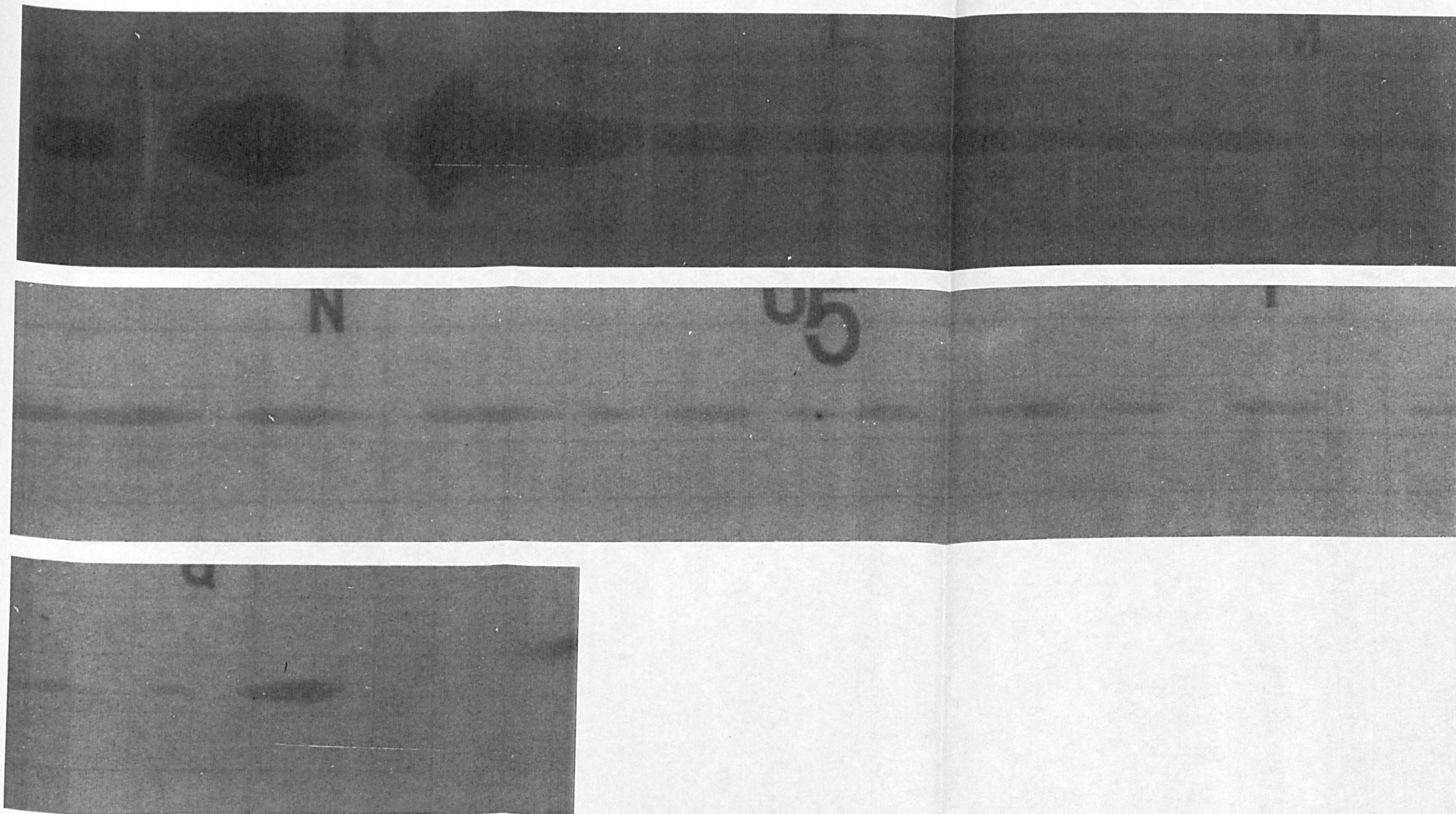


Figure 4.11: Radiograph of aluminium jet "Al-1", from material in the as manufactured condition. Liner axis parallel to the extrusion direction. Radiographed  $180.9\mu s$  after detonation

### 4.3 Non Heat Treatable

By selecting aluminum...  
control the effect of alloy...  
in order to investigate...

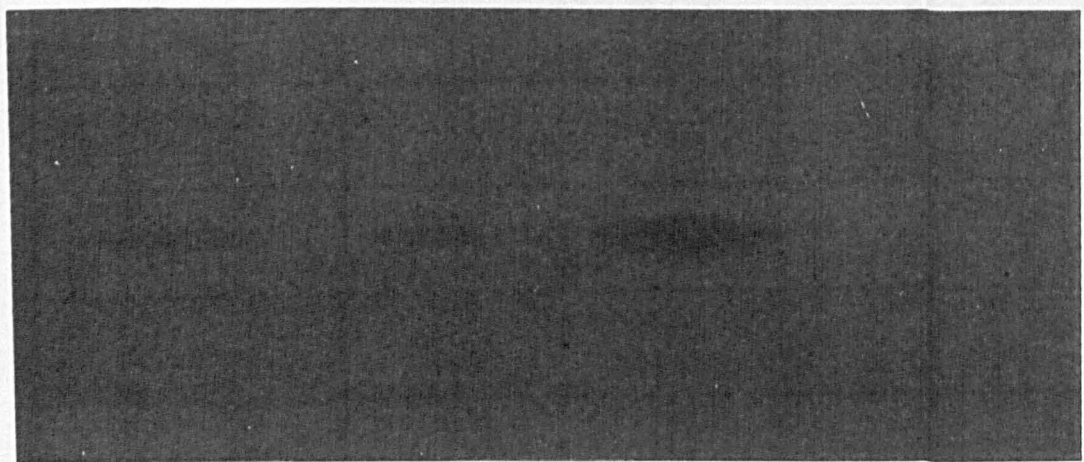
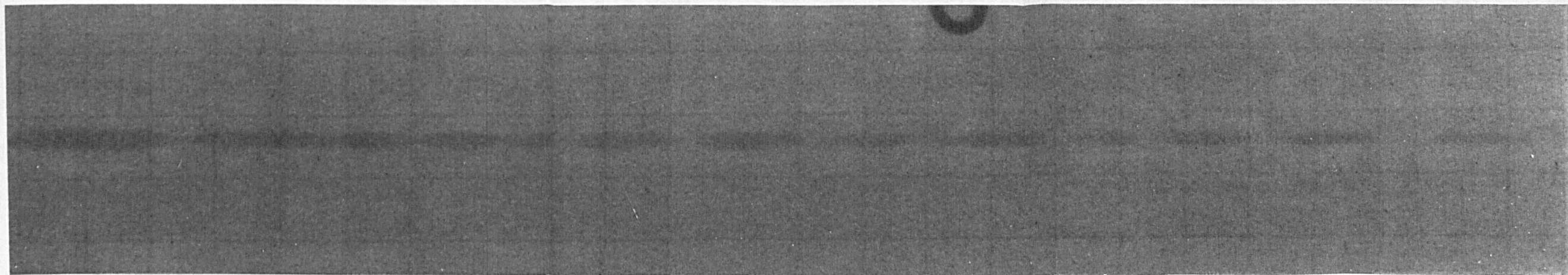
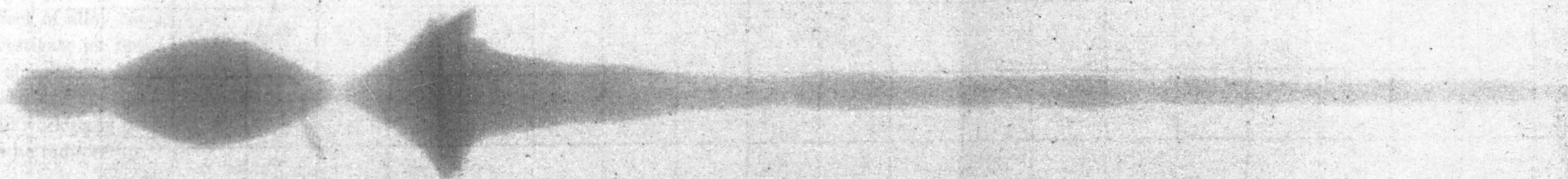


Figure 4.12: Radiograph of aluminium jet "Al-||", from material in the as-manufactured condition. Liner axis perpendicular to the extrusion direction. Radiographed  $181.0\mu s$  after detonation

### 4.3 Non Heat Treatable Aluminium Alloys

By selecting aluminium - magnesium alloys with varying magnesium content the effect of alloy composition on mechanical properties could be used to investigate jet break-up characteristics. A solid solution of magnesium in aluminium changes the tensile properties of the alloy: the UTS is increased and the strain at the UTS and strain to failure are decreased. Cold working of these alloys will cause an increase in the flow stress, this can be reduced again by annealing.

The relationship between the magnesium content of the alloy and mechanical properties are clearly seen in the stress versus strain curves shown in Figure 4.14. Several tests were made on each material to find the statistical deviation of the data. Each curve in Figure 4.14 shows the results of a single test which is typical of that material. The results and statistical analysis from the mechanical testing data are presented in Table 4.2. The standard deviation of the 0.2% proof stress and the ultimate tensile stress (UTS) was low for all aluminium - magnesium alloys. Meanwhile the standard deviation of the strain at UTS and the strain at failure was proportionately larger. The largest standard deviation was for the strain at UTS of 5154 alloy reference C, its deviation represented 20% of the mean value for strain at UTS. This large variance was attributed to random variations in stress due to discontinuous yielding which result in stress peaks, these can effect the value of strain at which the UTS is observed.

Micrographs of the four grain structures in the as-manufactured condition are shown in Figures: 4.15, 4.16, 4.17 and 4.18. Only in Figure 4.15 is there evidence that recrystallisation has occurred as a result of hot working by the extrusion process.

Mondolfo [63] notes that increasing the magnesium in solid solution (in binary aluminium - magnesium alloys) increases the recrystallisation temperature whilst magnesium in the form of coarse  $Mg_5Al_8$  particles<sup>1</sup> has no effect. Mondolfo gives the limit of solid solubility for magnesium in aluminium as 1.9wt% at 300°K under equilibrium conditions but notes that under other circumstances 4 → 5wt% magnesium may be required

---

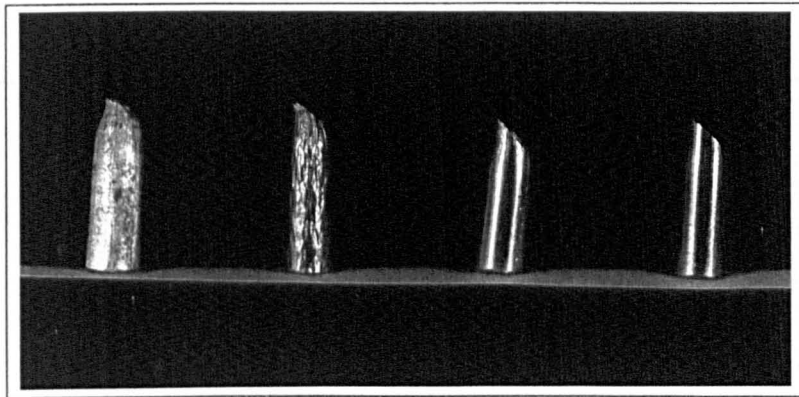
<sup>1</sup>In aluminium - magnesium alloys the second phase in equilibrium with aluminium is usually given as  $Mg_2Al_3$  however Mondolfo [63] suggests  $Mg_5Al_8$

to cause precipitation of  $Mg_5Al_8$  particles.

The 5251 grade alloy contained less magnesium than either the 5154 or the 5083 grade materials, see Table 3.4. The high magnesium content of the 5154 and 5083 grade alloys has therefore increased the recrystallisation temperature sufficiently to prevent recrystallisation and grain growth from occurring as a result of hot working during extrusion. However, in Figure 4.14 the 5154 grade alloy containing 3.24wt% magnesium (Figure 4.16) is seen to have a significantly lower UTS than the other 5154 grade alloy which contains 3.45wt% magnesium (Figure 4.17). This is attributed to the degree of working and to the effect of recovery on the 3.24wt% Mg material which is either limited or does not occur in the 3.45wt% material. Recovery has no visible effect on the grain structure of these materials but working effects remaining after cooling can alter the mechanical properties of the 3.24wt% Mg material - line B in Figure 4.14.

In Figure 4.13 the fracture surfaces of the aluminium - magnesium alloys are shown. The fracture specimen of the  $\sim 2wt\%$  Mg material (5251) exhibits "cup and cone" characteristics suggesting ductile fracture. In comparison the 3.24wt% Mg material (5154) also exhibits cup and cone characteristics and hence ductile fracture but the elongation to failure of this material is reduced. The "Orange Peel" effect visible on the specimens gauge length is typical of a large grained material deformed in tension. The fracture surfaces of the 3.45wt% Mg material (5154) and the  $\sim 4.5wt\%$  Mg material (5083) both indicate very low ductility failure through shear however in both cases their elongation to failure is similar to that of the material containing 3.24wt% magnesium. With increasing magnesium content these alloys are able to undergo decreasing amounts of strain between their UTS and failure. The strains to UTS for the un-recrystallised 5154 and 5083 alloys is lower than that of the 5251 alloy. Had all these alloys been in the recrystallised condition the effect of increasing magnesium in solid solution with aluminium would be to increase the strain to UTS. The shortfall in strain to UTS for the un-recrystallised alloys is accounted for by residual cold work.

The digitised images and radiographs of jets resulting from liners manufactured from these materials are shown in Figures 4.19 to 4.22 and 4.23 to 4.26. These images have characteristic features which are



~ 2wt% Mg	3.24wt% Mg	3.45wt% Mg	~ 4.5wt% Mg
5251	5154	5154	5083

Figure 4.13: Fracture surfaces of aluminium - magnesium alloys similar to those observed in high purity aluminium jets - see Section 4.2. There are also some important differences: Break-up has occurred along the entire length of the aluminium - magnesium jets whereas the high purity aluminium jets were continuous over a large proportion of their tail end. Note that all radiographic images of high purity aluminium and aluminium - magnesium alloys were recorded at a similar time after detonation. The fragments into which the aluminium - magnesium alloy jets have broken are irregular and angular in shape and have a low length to breadth ratio in comparison to the regular ellipsoidal fragments of high purity aluminium. Finally, the length of solid jet has decreased, conversely the amount of free space between the fragments has increased. According to the penetration equation - Equation 2.9 - the depth of penetration is proportional to the length of jet. However, the length term applies only to solid jet and not to the distance between the jets tip and its tail. The penetration of these aluminium - magnesium alloy jets will be inferior to that of the high purity aluminium jets in Section 4.2.

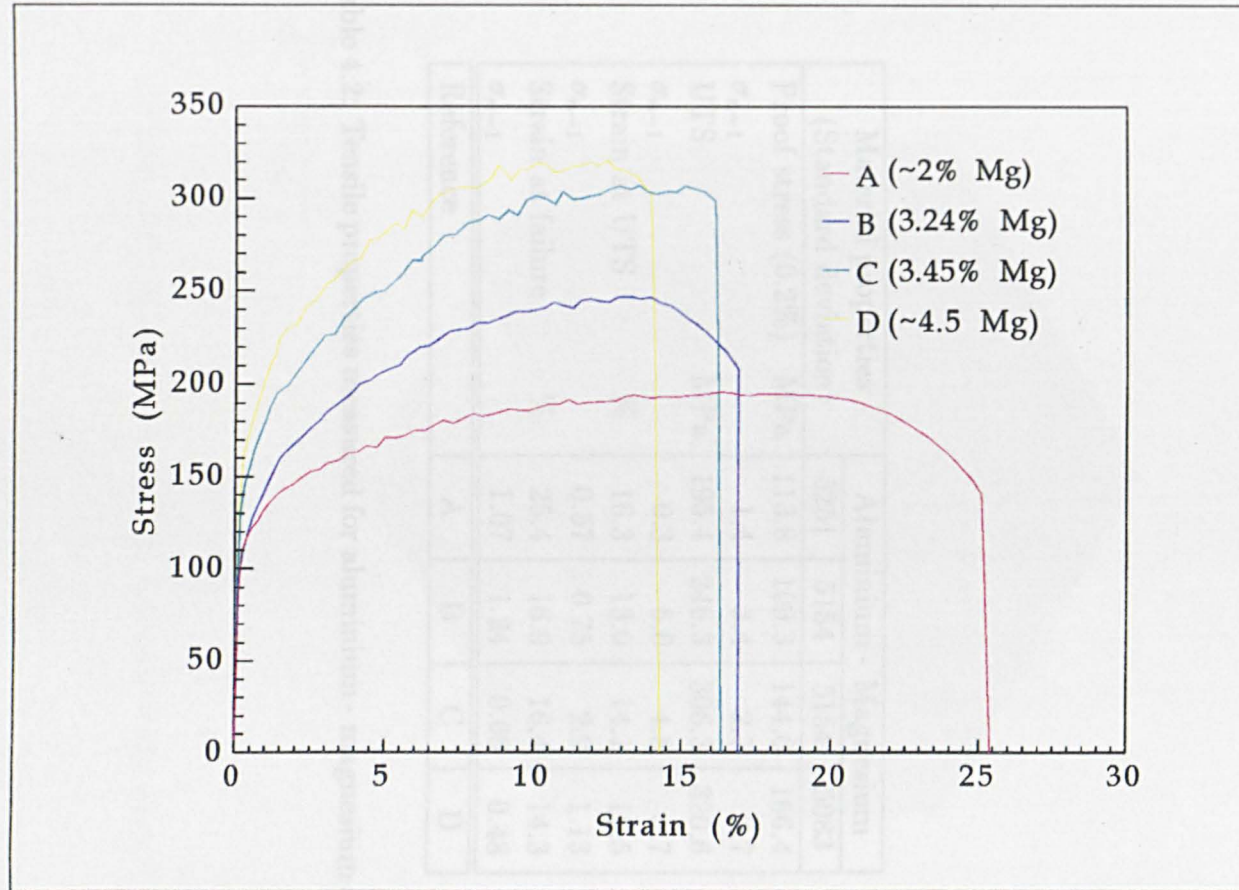
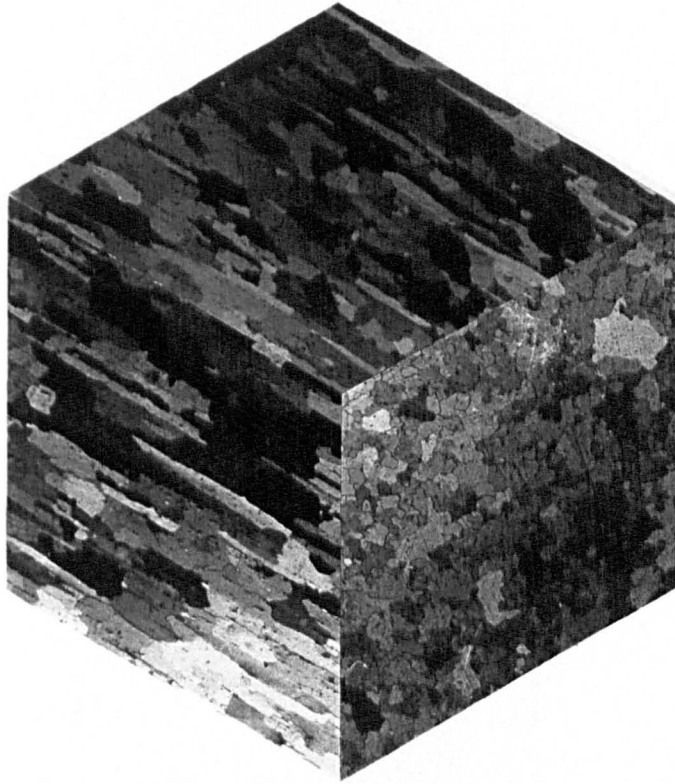


Figure 4.14: Stress versus strain for aluminium - magnesium alloys

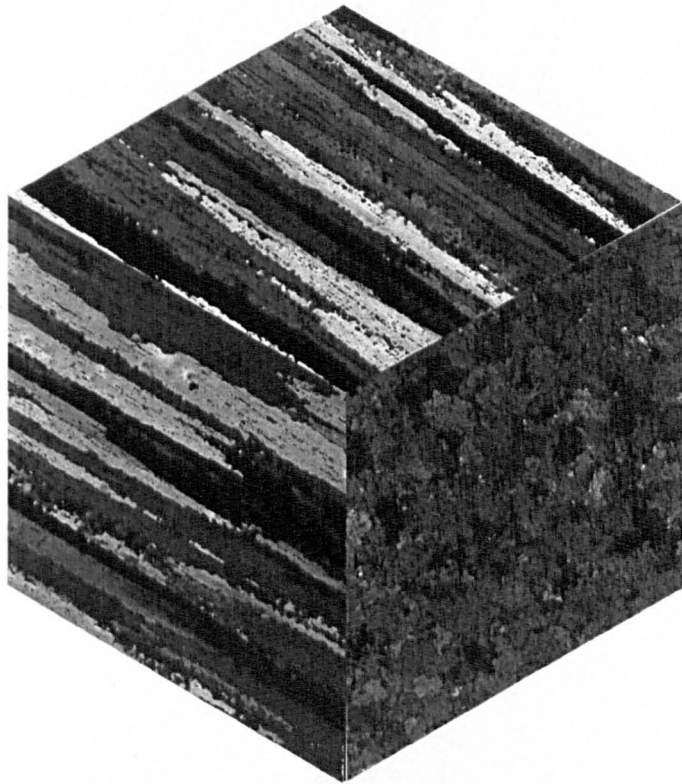
Material properties (Standard deviation)	Aluminium - Magnesium			
	5251	5154	5154	5083
Proof stress (0.2%) MPa	113.8	109.3	144.6	166.4
$\sigma_{n-1}$	1.4	3.4	2.7	2.7
UTS MPa	195.4	246.3	306.3	320.6
$\sigma_{n-1}$	0.3	6.0	4.8	5.7
Strain at UTS %	16.3	13.0	14.1	12.5
$\sigma_{n-1}$	0.57	0.75	2.9	1.13
Strain at failure %	25.4	16.9	16.4	14.3
$\sigma_{n-1}$	1.07	1.24	0.66	0.48
Reference	A	B	C	D

Table 4.2: Tensile properties measured for aluminium - magnesium alloys



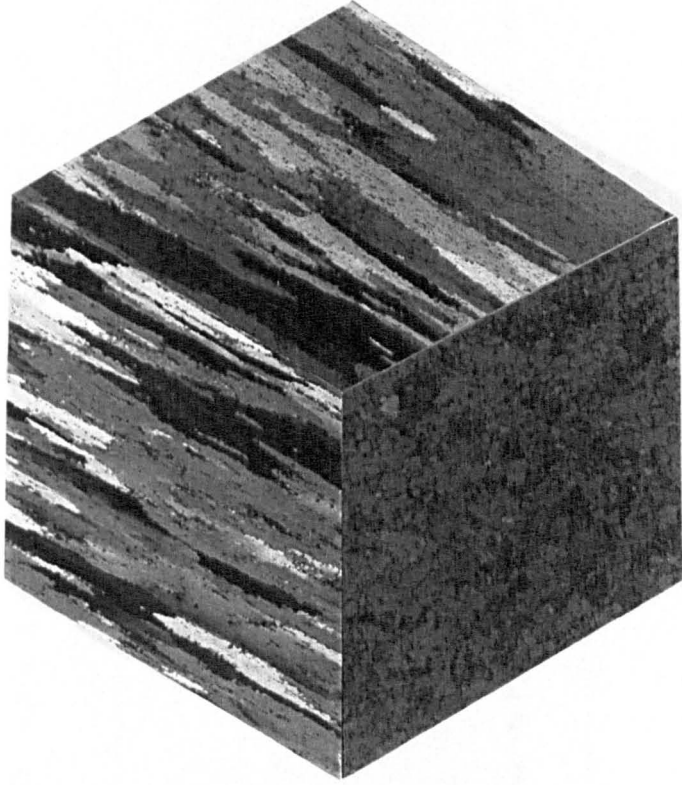
× 25  1mm

Figure 4.15: Micrograph of 5251, Al ~ 2wt%Mg alloy



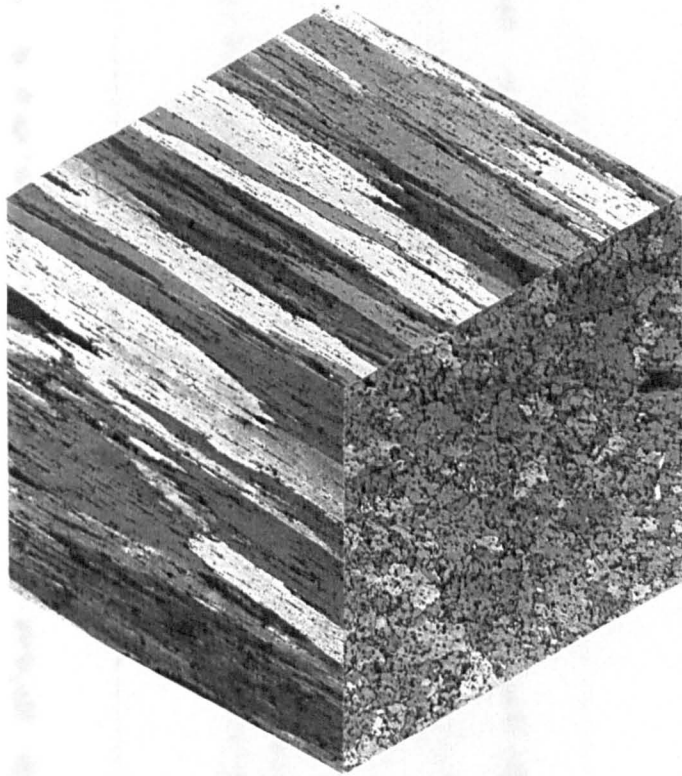
× 25  1mm

Figure 4.16: Micrograph of 5154, Al 3.24wt%Mg alloy



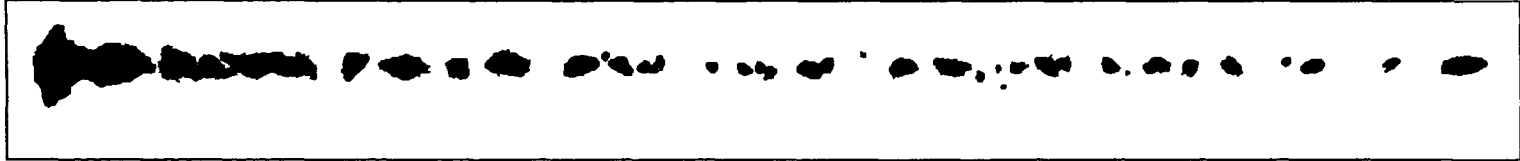
× 25  1mm

Figure 4.17: Micrograph of 5154, Al 3.45wt%Mg alloy



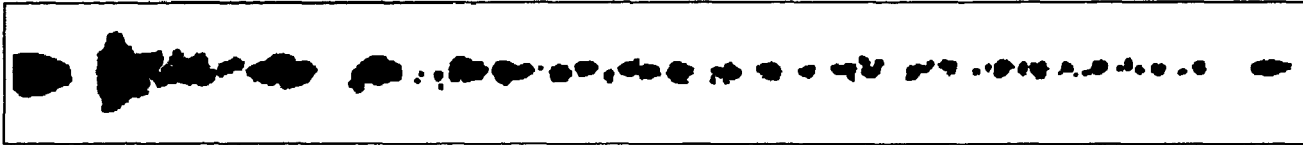
× 25      1mm

Figure 4.18: Micrograph of 5083, Al ~ 4.5wt%Mg alloy



100mm

Figure 4.19: Digitised image of jet from aluminium - magnesium alloy 5251,  $\sim 2wt\%$  Mg (Firing reference A). Radiographed  $179.5\mu s$  after detonation



100mm

Figure 4.20: Digitised image of jet from aluminium - magnesium alloy 5154,  $3.24wt\%$  Mg (Firing reference B). Radiographed  $179.4\mu s$  after detonation

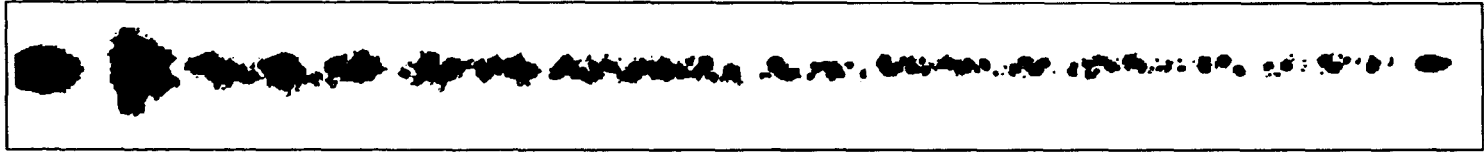


Figure 4.21: Digitised image of jet from aluminium - magnesium alloy 5154, 3.45wt% Mg (Firing reference C). Radiographed 181.4 $\mu$ s after detonation

85

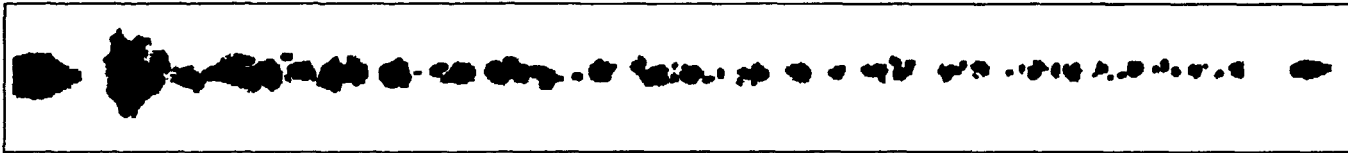


Figure 4.22: Digitised image of jet from aluminium - magnesium alloy 5083, ~ 4.5wt% Mg (Firing reference D). Radiographed 179.5 $\mu$ s after detonation

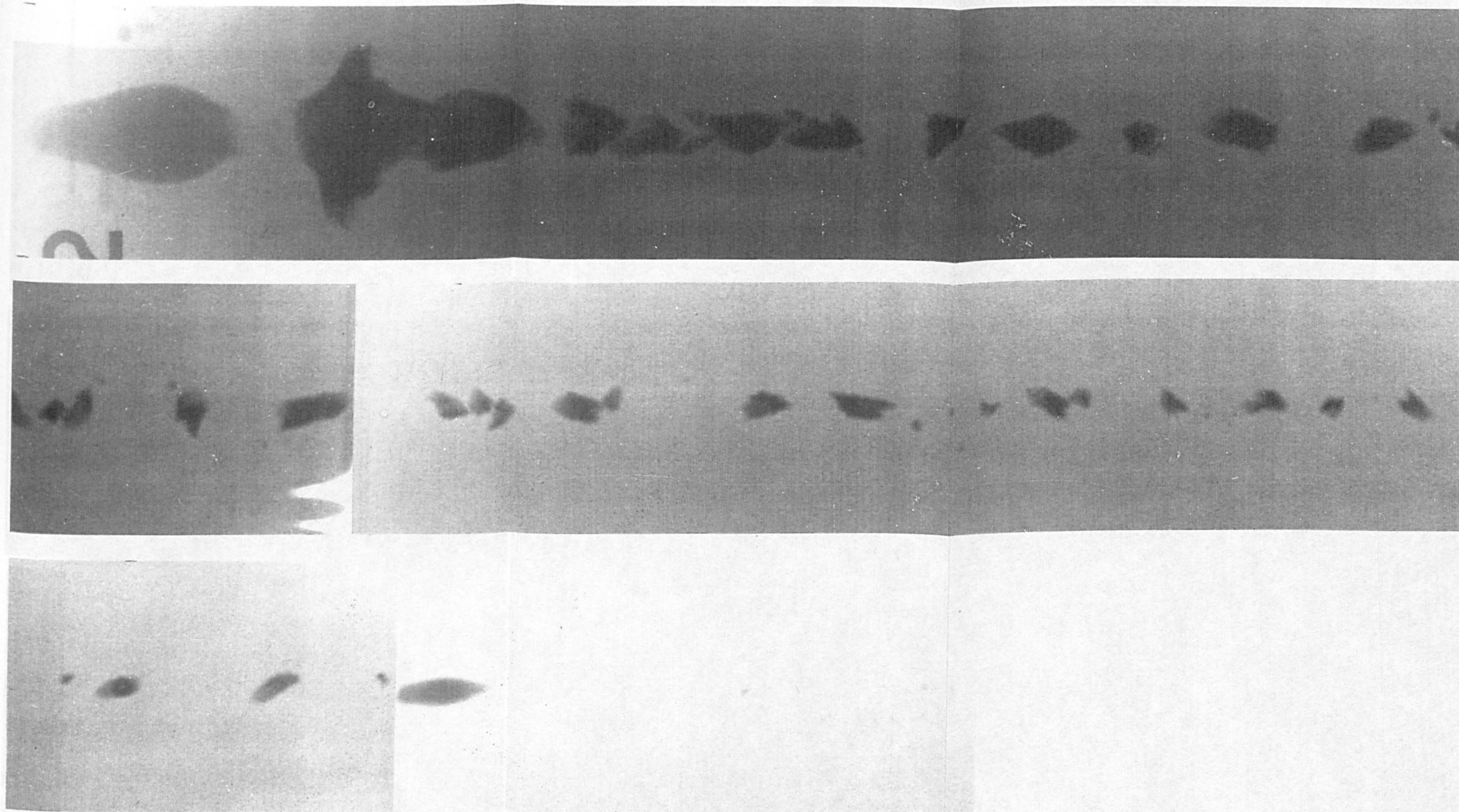


Figure 4.23: Radiograph of jet from aluminium - magnesium alloy 5251 containing  $\sim 2wt\%$  Mg (Firing reference A). Radiographed  $179.5\mu s$  after detonation

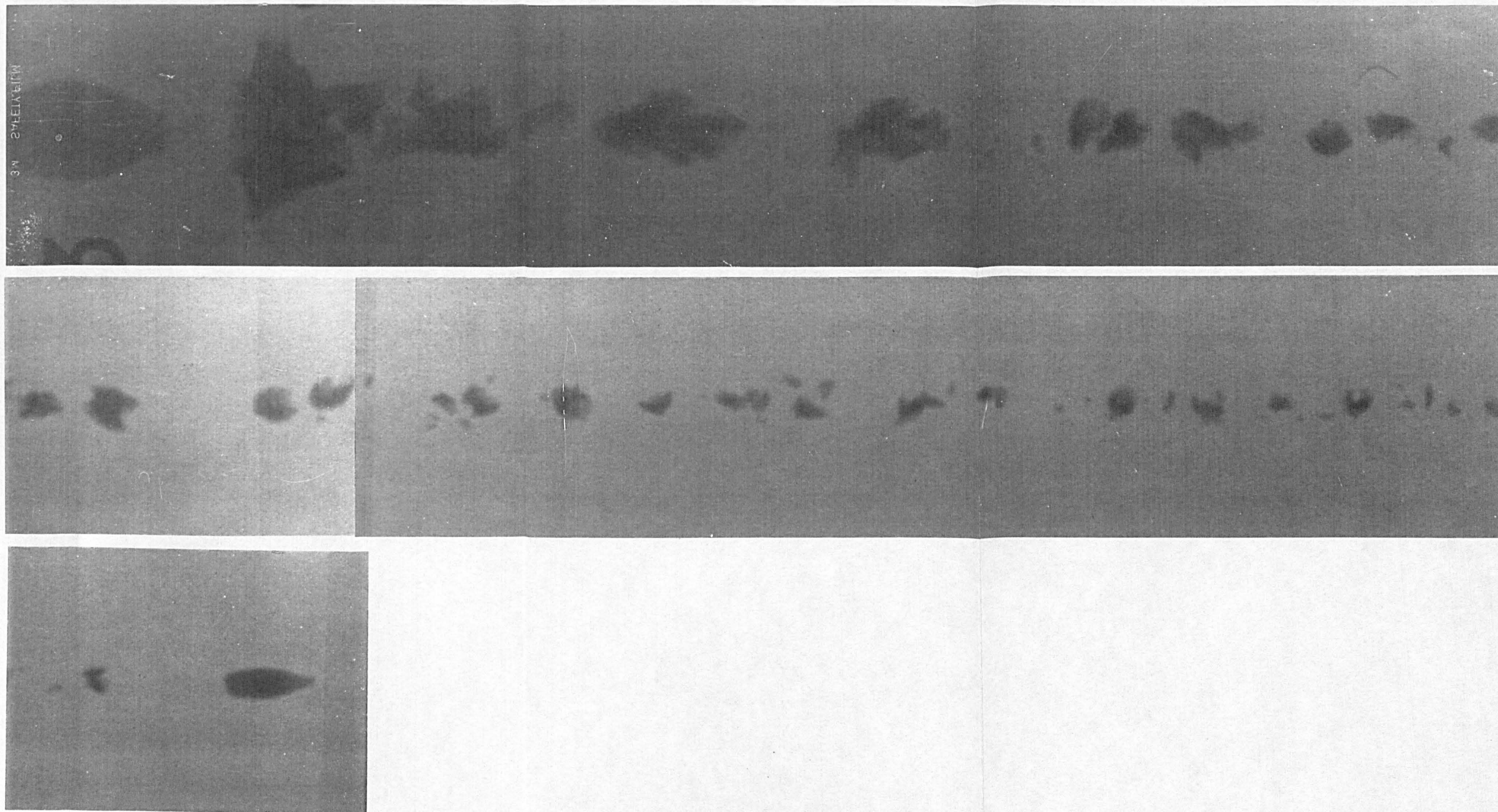


Figure 4.24: Radiograph of jet from aluminium - magnesium alloy 5154 containing 3.24wt% Mg (Firing reference B). Radiographed 179.4 $\mu$ s after detonation

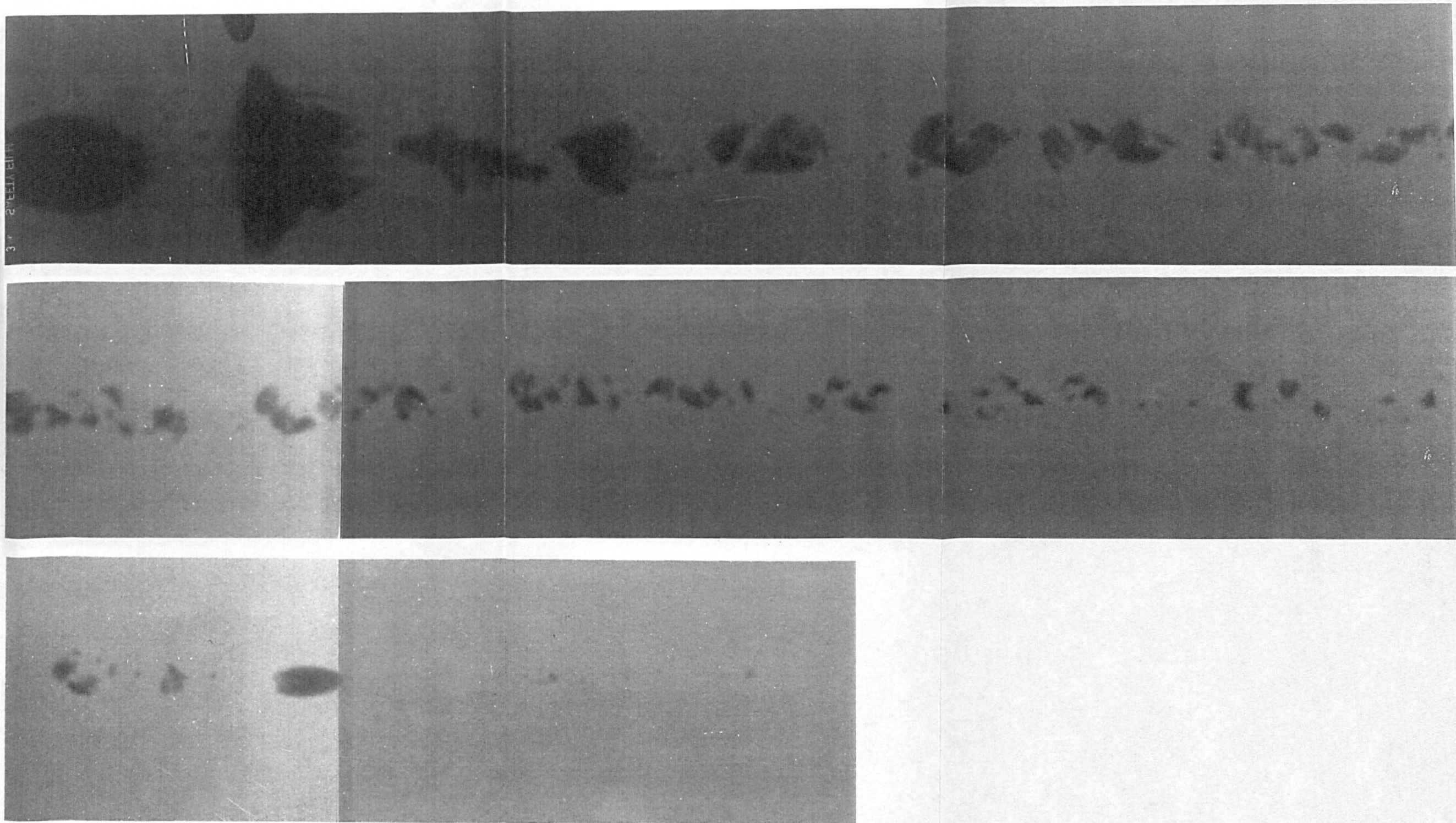
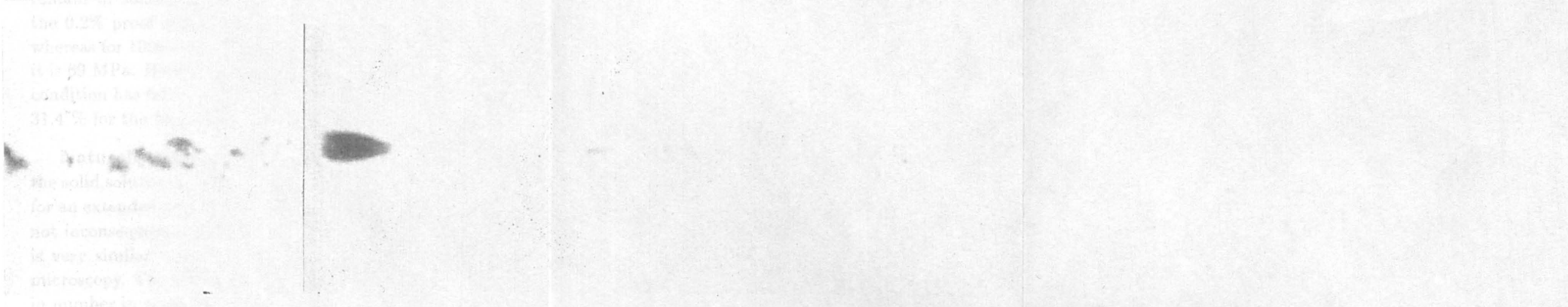
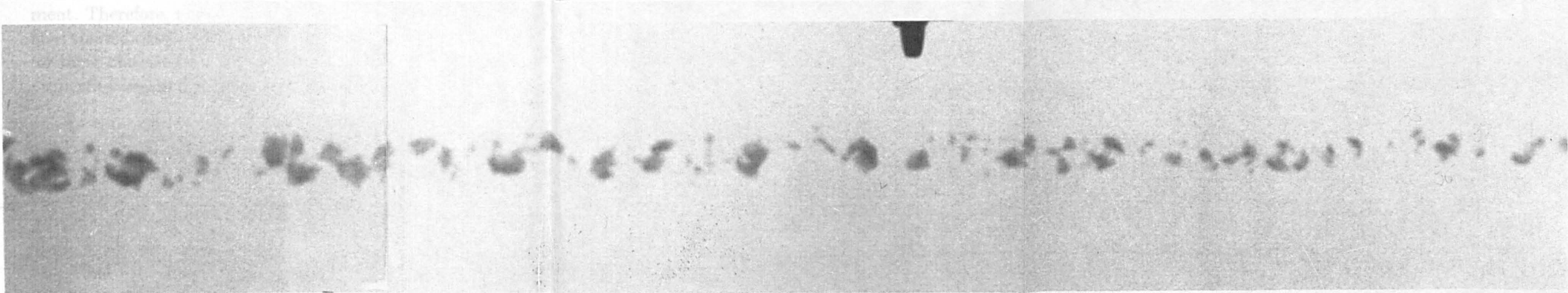
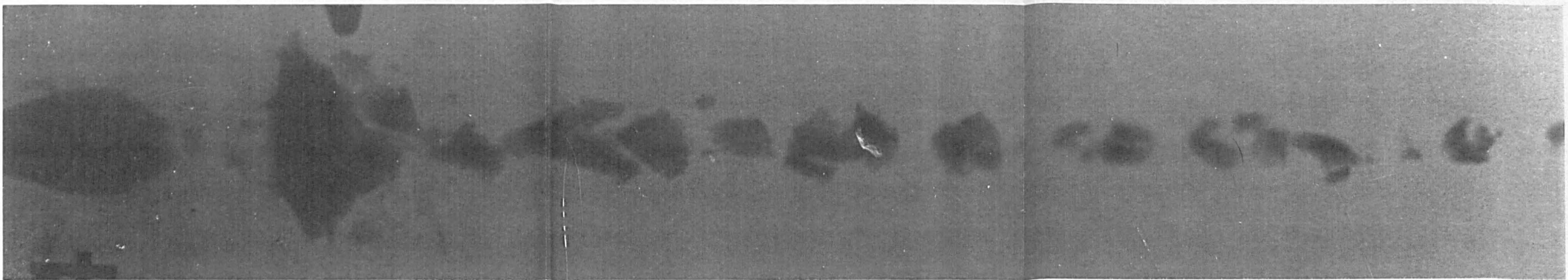


Figure 4.25: Radiograph of jet from aluminium - magnesium alloy 5154 containing 3.45wt% Mg (Firing reference C). Radiographed 181.4 $\mu$ s after detonation



ment. Therefore

the 0.2% proof stress  
whereas for the  
it is 50 MPa. In  
condition has  
31.4% for the  
nature  
the solid solution  
for an extender  
not inconspicuous  
is very similar  
microscopy. It  
in number is

Figure 4.26: Radiograph of jet from aluminium - magnesium alloy 5083 containing  $\sim 4.5wt\%$  Mg (Firing reference D). Radiographed  $179.5\mu s$  after detonation

## 4.4 Precipitate Strengthened Aluminium Alloys

Firings were carried out on a high strength, age hardening aluminium-copper - magnesium alloy designated as 2014. The 2014 material was tested in four different heat treated conditions which were selected because of their effect on the size and distribution of the second phase and hence their effect on mechanical properties. Copper forms a range of precipitates in aluminium which, in order of increasing thermodynamic stability, are: GP zones  $\rightarrow \theta'' \rightarrow \theta' \rightarrow \theta$ . Additional strengthening can be gained from the presence of other precipitates containing aluminium, magnesium and copper - *ie.* S phase  $Al_2CuMg$ . The precipitate phases present will depend entirely upon composition and previous heat treatment. Therefore, when referring to 2014 alloys it is imperative that their heat treated condition is known. The stress versus strain graphs recorded for these materials are shown in Figure 4.27 and their tensile mechanical properties are summarised in Table 4.3.

**As quenched** - Figure 4.30 The alloying constituents dissolve into solid solution during heat treatment, on quenching this structure remains but is in a thermodynamically unstable condition. Precipitate nucleation can occur immediately at ambient temperature: this alloy contains approximately 4.5wt% copper, of which only  $\sim 0.1$ wt% is stable in solution at 20°C. In the as quenched and refrigerated condition little GP zone formation will occur. These GP zones and alloying constituents which remain in solid solution have resulted in considerable strengthening - the 0.2% proof stress of 2014 in the as-quenched condition is 196 MPa whereas for 1050 commercially pure aluminium in the annealed condition it is 69 MPa. However, the ductility of the 2014 alloy in the as-quenched condition has fallen to 18.9 % nominal strain at failure in comparison to 31.4 % for the high purity aluminium.

**Naturally aged** - Figure 4.32 The material is initially quenched from the solid solution as described above, but then held at room temperature for an extended period. Diffusion at this temperature is at a very low but not inconsequential rate. The microstructure of naturally aged material is very similar to that of as-quenched material as observed by optical microscopy. The GP zones in the naturally aged material will be greater in number in comparison to those in the as-quenched material, in either case the size of these GP zones will be of the order 10 nm in diameter.

The increased number of GP zones has a very dramatic effect on the stress versus strain relationship for this material. Figure 4.27 shows that the material in the naturally aged condition - line NA - has a significantly increased yield stress and UTS while there is a slight reduction in the strain at failure when compared to the material in the as-quenched condition - line QU.

**L168-T6511** - Figure 4.28 This specification prescribes an artificial ageing treatment. After quenching from solid solution the material is reheated to  $\sim 170^{\circ}\text{C}$ , this raises the rate of diffusion for alloying constituents and allows the transformation of GP zones to  $\theta''$  or  $\theta'$  precipitates. These precipitates form as discs of the order  $100\text{nm}$  in diameter and therefore they cause no optically observable change in the microstructure when compared to material in the naturally aged or as-quenched conditions. The stress versus strain relationship for this material is indicated by line T6 in Figure 4.27. This shows material in the T6 condition to have a higher yield stress and similar UTS to material in the naturally aged condition, however its strain at failure has been dramatically reduced. The purpose of the T6 heat treatment for commercial 2014 alloys is to increase the proof stress of the material.

**Slow cooled** - Figure 4.34 The material is not quenched from the solid solution, it remains in the furnace and is cooled slowly to room temperature. The material will therefore be in an equilibrium condition and thermodynamically completely stable. All insoluble alloying elements will have formed  $\theta$  precipitates which would then have had time to coarsen. As a result of segregation and because the rate of diffusion is greater along grain boundaries than in the bulk grain, the coarse precipitates form on grain boundaries. These precipitates are sufficiently large to be observed optically. Note that the magnification used in Figure 4.34 is greater than that for Figures 4.28, 4.30 and 4.32 in order that these grain boundary precipitates are clearly shown. Slow cooling has resulted in the formation of precipitates too large to result in optimum strengthening through interactions with dislocations. As a result its stress versus strain relationship - line SC in Figure 4.27 - shows that the yield stress and the UTS of this material have fallen dramatically when compared to those achieved for the heat treatments described previously. However, the presence of precipitates has still increased the yield stress and UTS in comparison to that of high purity aluminium.

All the firings of age hardening aluminium alloys had similar break-up characteristics; there was little jet elongation before brittle fracture resulted in jet break-up. These effects are similar although more extreme to those which occurred for aluminium - magnesium alloys when break-up is compared to that of high purity aluminium jets. Comparison of the images is harder though as these aluminium - copper - magnesium alloy jets were recorded at a much earlier time to those of the high purity aluminium or the aluminium - magnesium alloy jets. The digitised images from firings of aluminium - copper - magnesium alloy jets are presented in Figures 4.29 to 4.35 and the radiographic images are presented in Figures 4.36 to 4.39.

Material properties		Age hardening aluminium alloys			
		2014 T6511	As Quenched	Natural Aged	Slow Cooled
Proof stress (0.2%)	MPa	475	196	383	117
UTS	MPa	522.0	413.8	545.5	237.1
Strain at UTS	%	5.7	16.6	14.0	11.6
Strain at failure	%	7.8	16.6	16.1	16.8
Reference		T6	QU	NA	SC

Table 4.3: Tensile properties measured for aluminium - copper - magnesium alloys

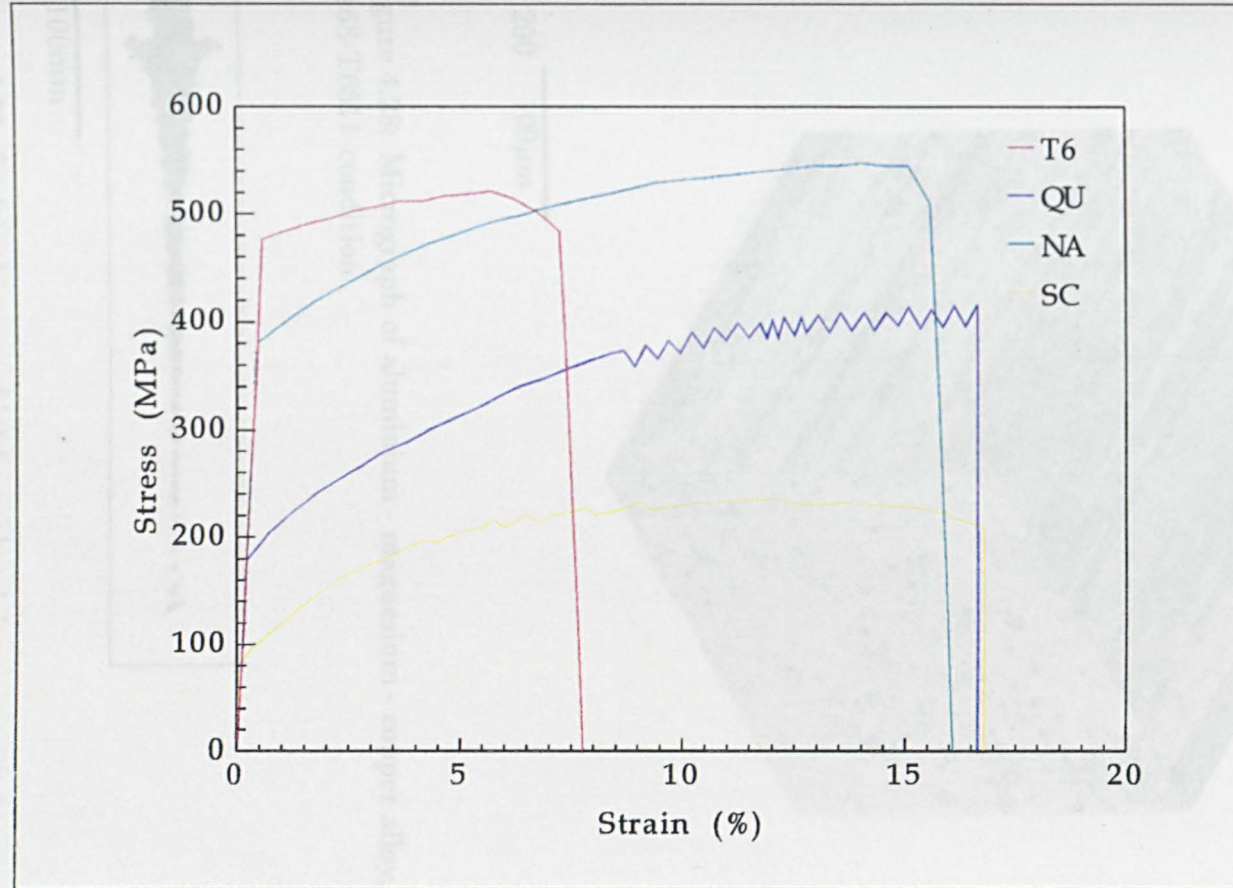
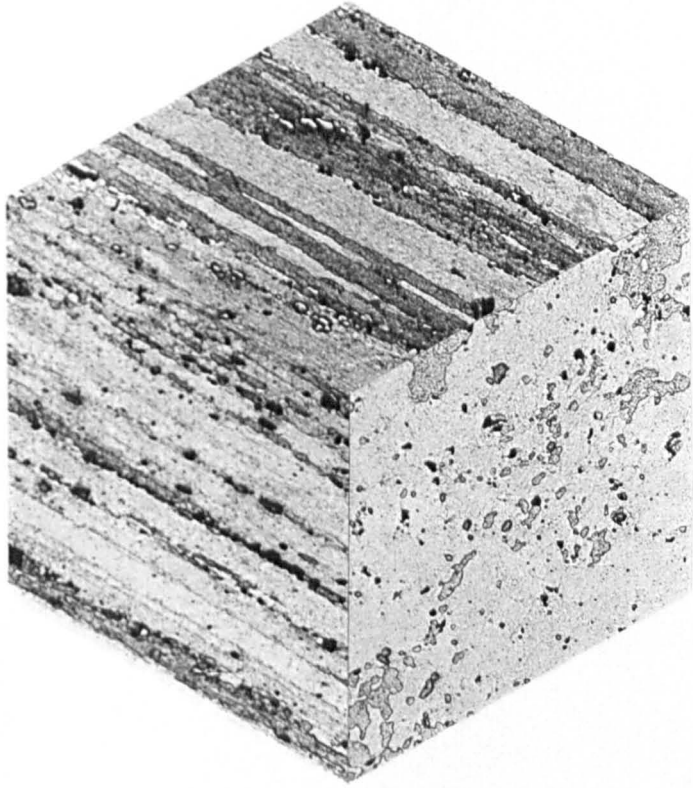
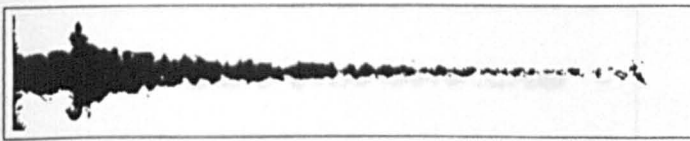


Figure 4.27: Stress versus strain for aluminium - copper - magnesium alloy of composition 2014



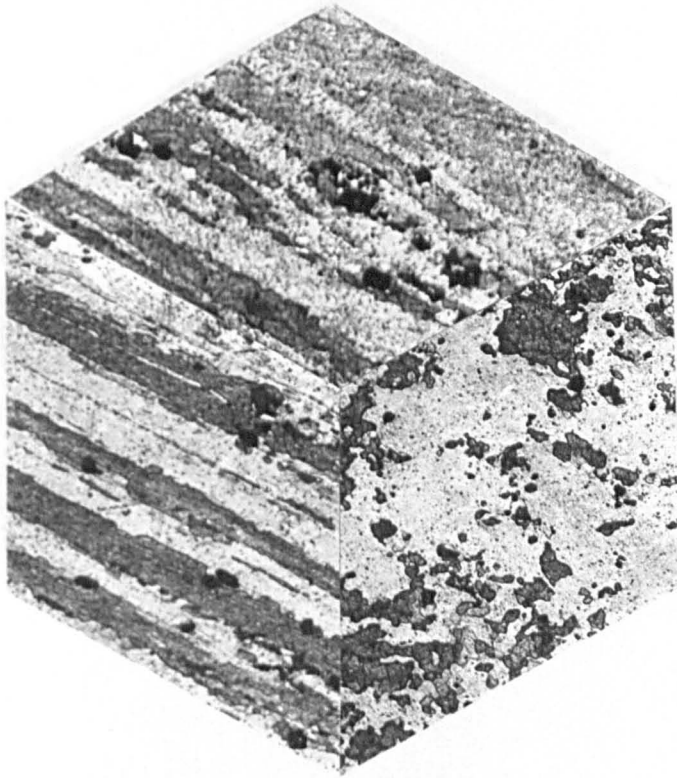
$\times 200$   $\overline{100\mu m}$

Figure 4.28: Micrograph of aluminium - magnesium - copper alloy, 2014. L168-T6511 condition



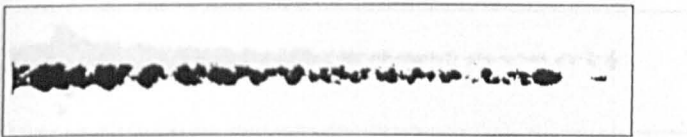
$\overline{100mm}$

Figure 4.29: Digitised image of jet from aluminium - magnesium - copper alloy 2014, in the L168-T6511 condition. Radiographed  $100.1\mu s$  after detonation



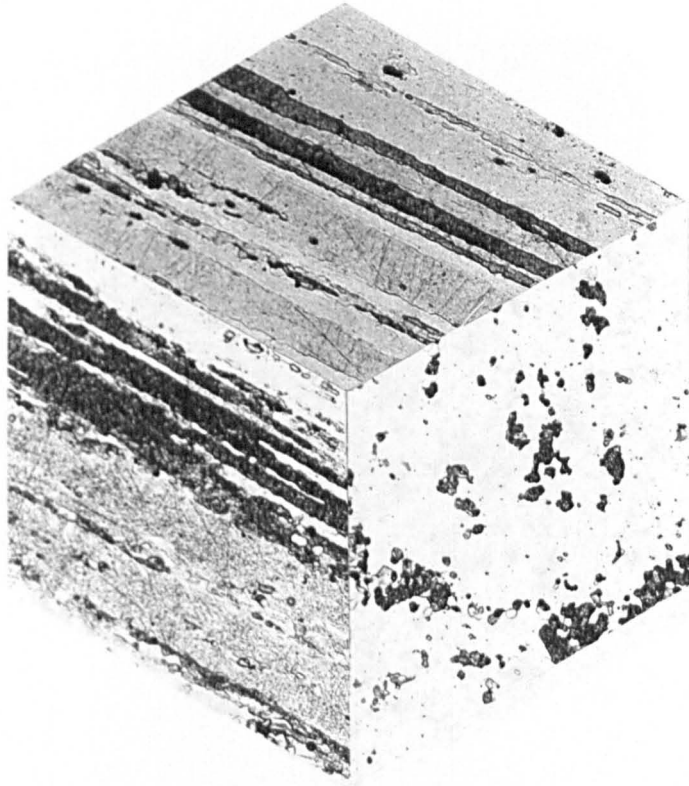
$\times 200$   $\overline{100\mu m}$

Figure 4.30: Micrograph of aluminium - magnesium - copper alloy, 2014. As quenched condition



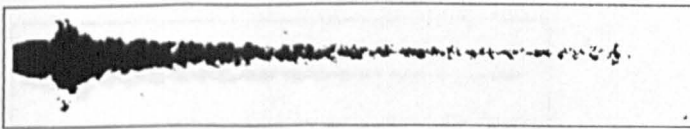
$\overline{100mm}$

Figure 4.31: Digitised image of jet from aluminium - magnesium - copper alloy 2014, in the As quenched condition. Radiographed  $91.0\mu s$  after detonation



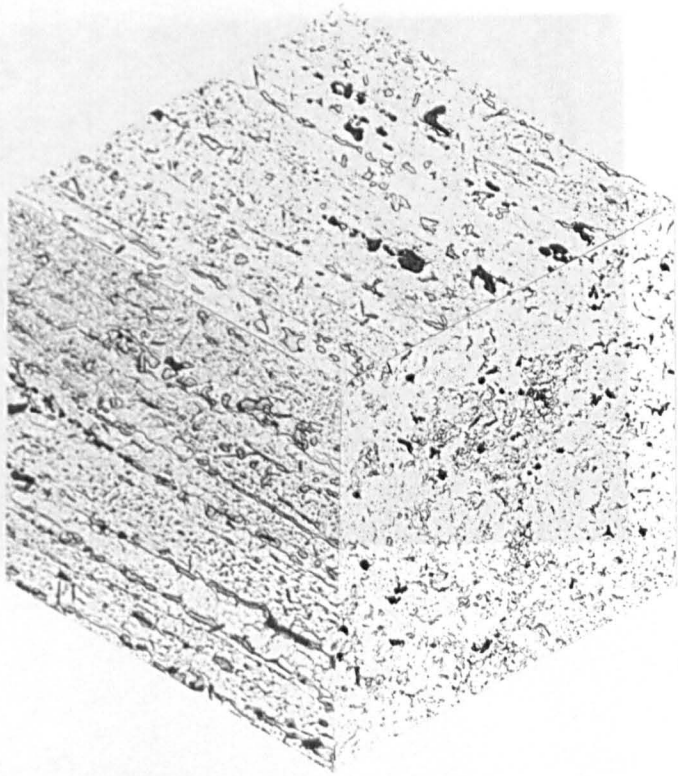
× 200  $\overline{100\mu m}$

Figure 4.32: Micrograph of aluminium - magnesium - copper alloy, 2014. Naturally aged condition



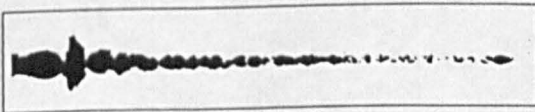
$\overline{100mm}$

Figure 4.33: Digitised image of jet from aluminium - magnesium - copper alloy 2014, in the Naturally aged condition. Radiographed  $100.4\mu s$  after detonation



$\times 400$   $\overline{50\mu m}$

Figure 4.34: Micrograph of aluminium - magnesium - copper alloy, 2014. Slow cooled condition



$\overline{100mm}$

Figure 4.35: Digitised image of jet from aluminium - magnesium - copper alloy 2014, in the Slow cooled condition. Radiographed  $100.1\mu s$  after detonation

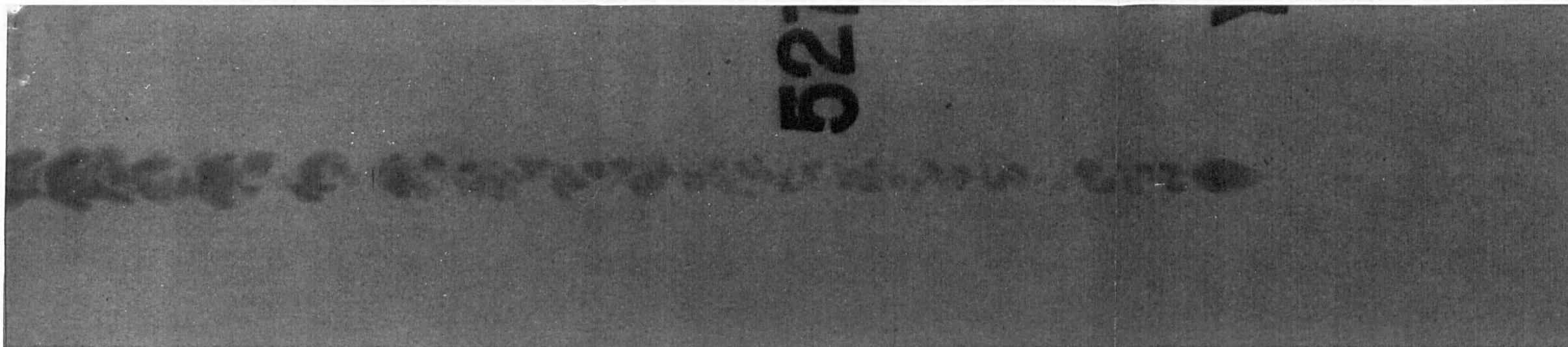


Figure 4.36: Radiograph of jet from aluminium - magnesium - copper alloy 2014, in the As quenched condition. Radiographed  $91.0\mu s$  after detonation



Figure 4.37: Radiograph of jet from aluminium - magnesium - copper alloy 2014, in the L168-T6511 condition. Radiographed  $100.1\mu s$  after detonation

#### 4.5 Commercially Pure Magnesium

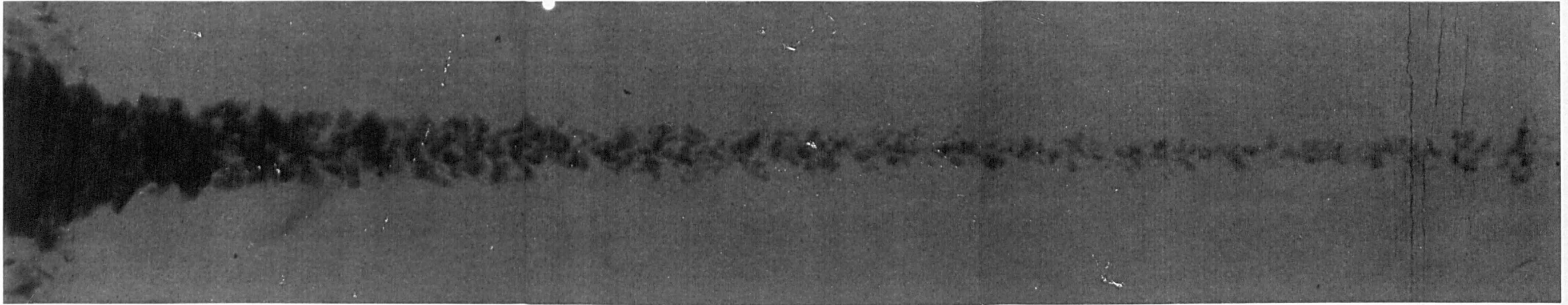


Figure 4.38: Radiograph of jet from aluminium - magnesium - copper alloy 2014, in the Naturally aged condition. Radiographed  $100.4\mu s$  after detonation

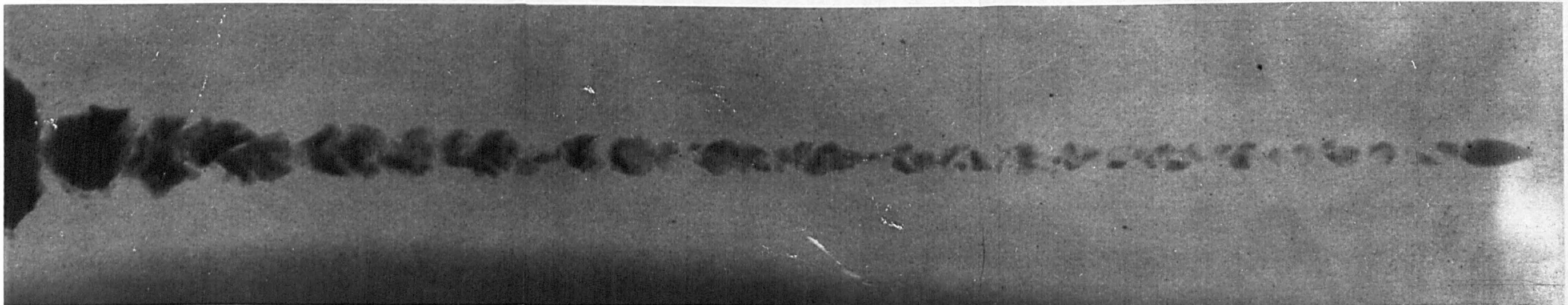


Figure 4.39: Radiograph of jet from aluminium - magnesium - copper alloy 2014, in the Slow cooled condition. Radiographed  $100.1\mu s$  after detonation

## 4.5 Commercially Pure Copper

These experiments with a denser metal were designed to complement the aluminium data and test any theories that arose relating jet break-up to the mechanical properties of the liner material.

Micrographs of the two grain structures are shown in Figures: 4.41, and 4.42. The microstructure developed by shear spinning from annealed sheet is shown in Figure 4.41, this shows large grains which contain annealing twins. There are no visible mechanical twins since the amount of cold work applied by shear spinning was small. However, etching has revealed that the material has a "distressed" appearance. Large numbers of shear lines appear dark when etched because residual cold work makes them chemically distinguishable from undeformed material. Figure 4.42 shows the shear spun material after annealing. Recovery, recrystallisation and grain growth have all clearly taken place resulting in a reduction in grain size.

The tensile properties for copper with different heat treatments are summarised in Table 4.4 and their stress versus strain curves are shown in Figure 4.40. The copper is seen to be more ductile than high purity aluminium and to have higher yield stress and UTS. It is interesting to note that there is only a small difference in the yield stress of copper in the two heat treated conditions. Cold working of an annealed material would be expected to raise the yield stress, re-annealing the material would then be expected to lower the yield stress. In this case though re-annealing resulted in recrystallisation which caused an overall reduction in grain size. This results in an increase in yield stress as described by the Hall - Petch relationship, Equation 4.1.

The digitised images from firings of liners manufactured from these materials are presented in Figures 4.43, and 4.44. Their radiographs are shown in Figures 4.45, and 4.46. When compared to the images of high purity aluminium (digitised - Figures 4.5 to 4.8 radiographic - Figures 4.9 to 4.12) the copper jets differ most noticeably in the region of the slug and the tail of the jet. Note that the images of the copper jets were recorded at a later time than those of the high purity aluminium. It is therefore suggested that this difference is not of major significance. The copper jets are seen to be virtually completely broken-up into ellipsoidal

fragments. These fragments are irregular and angular in comparison to those for high purity aluminium but not to the same extent as the aluminium alloys.

Material Properties		Copper	
		Cu-M	Cu-O
Proof stress (0.2%)	MPa	146.7	137.1
UTS	MPa	229.3	215.9
Strain at UTS	%	38.8	36.1
Strain at failure	%	50.0	49.5

Table 4.4: Tensile properties measured for copper

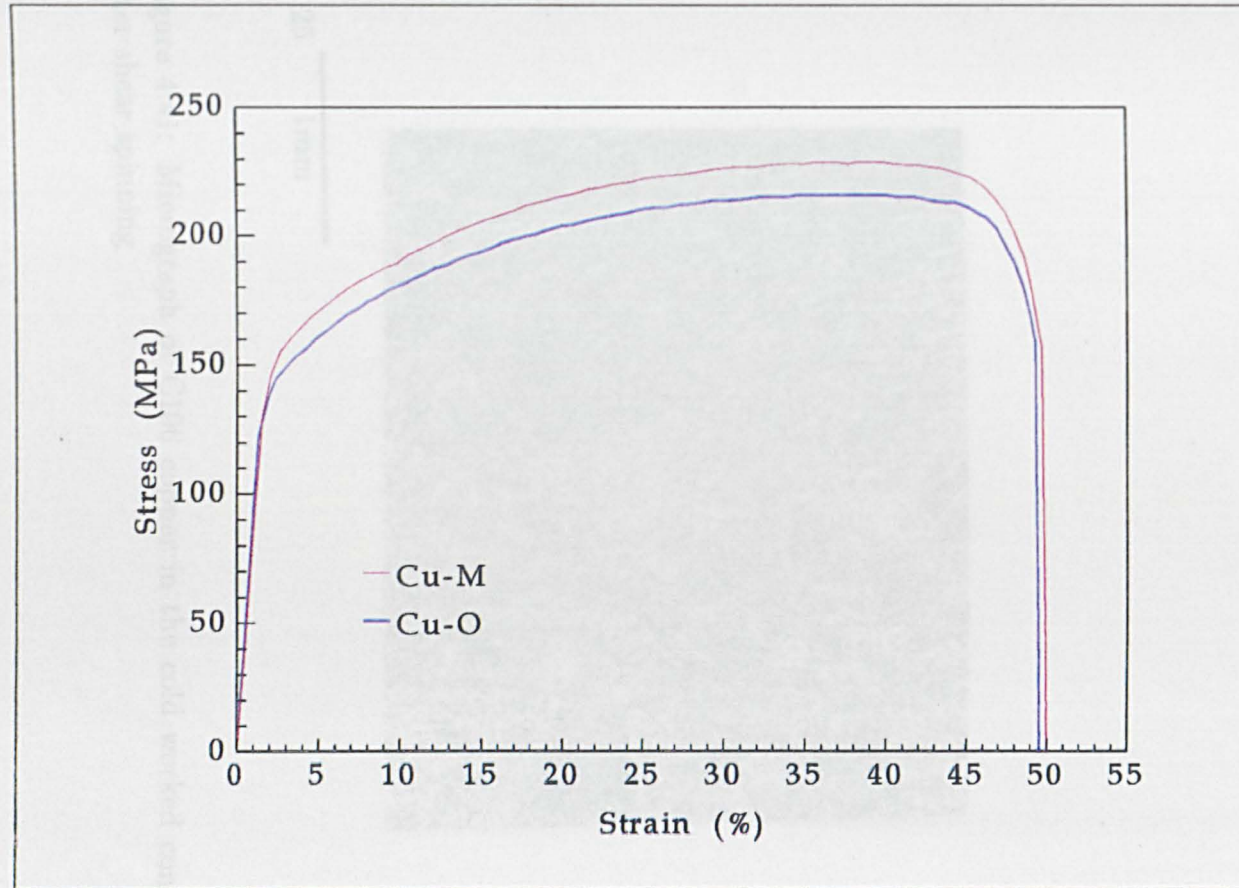
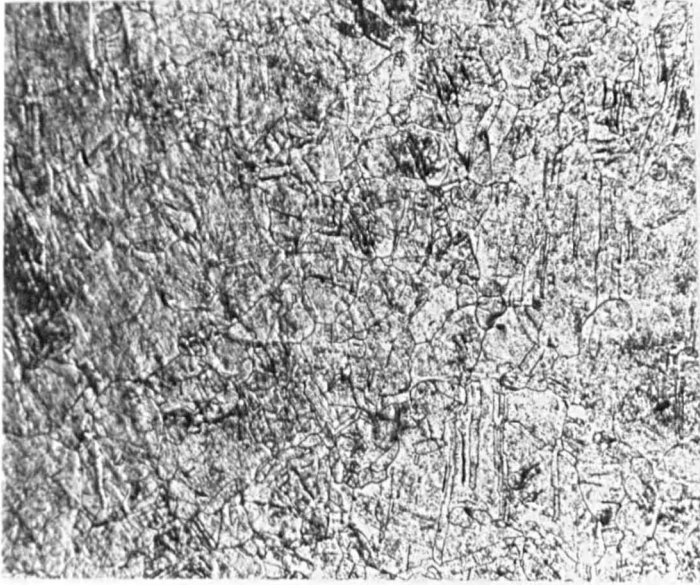
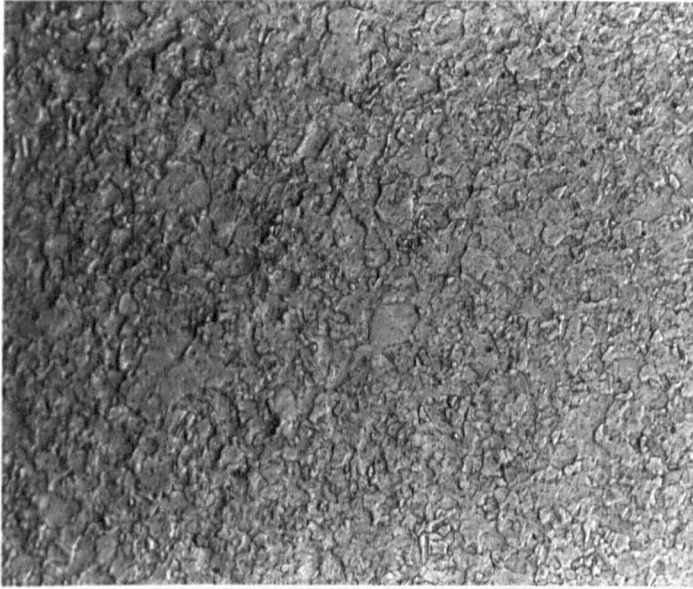


Figure 4.40: Stress versus strain for copper in the as-manufactured and partially annealed conditions



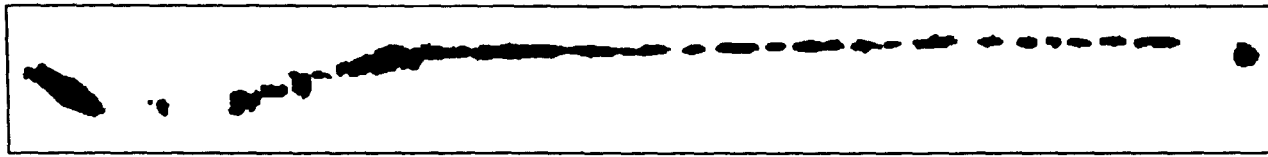
× 25  1mm

Figure 4.41: Micrograph of C106 copper in the cold worked condition after shear spinning



× 25  1mm

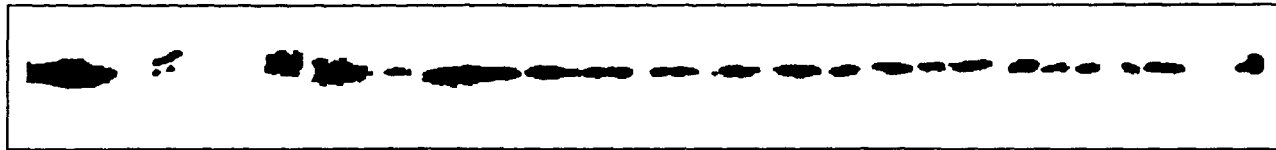
Figure 4.42: Micrograph of C106 copper which has been cold worked by shear spinning and then annealed



100mm

Figure 4.43: Digitised image of copper jet “Cu-M”, shear spun from annealed plate. Radiographed  $200.0\mu s$  after detonation

105



100mm

Figure 4.44: Digitised image of partially annealed copper jet “Cu-O”, shear spun from annealed plate and then partially re-annealed. Radiographed  $200.9\mu s$  after detonation

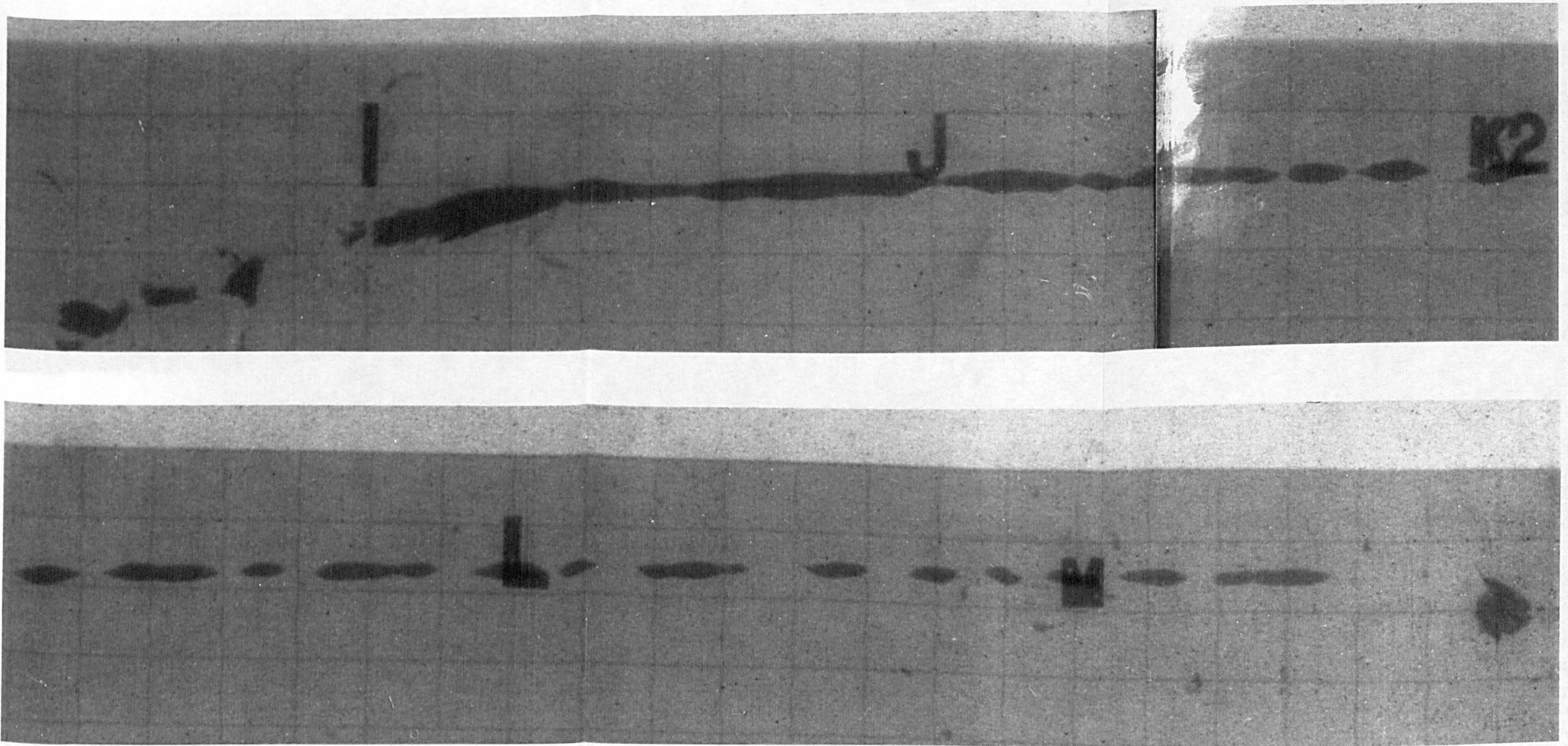


Figure 4.45: Radiograph of as-manufactured copper jet "Cu-M", shear spun from annealed plate. Radiographed  $200.0\mu s$  after detonation

CHAPTER

Capture of

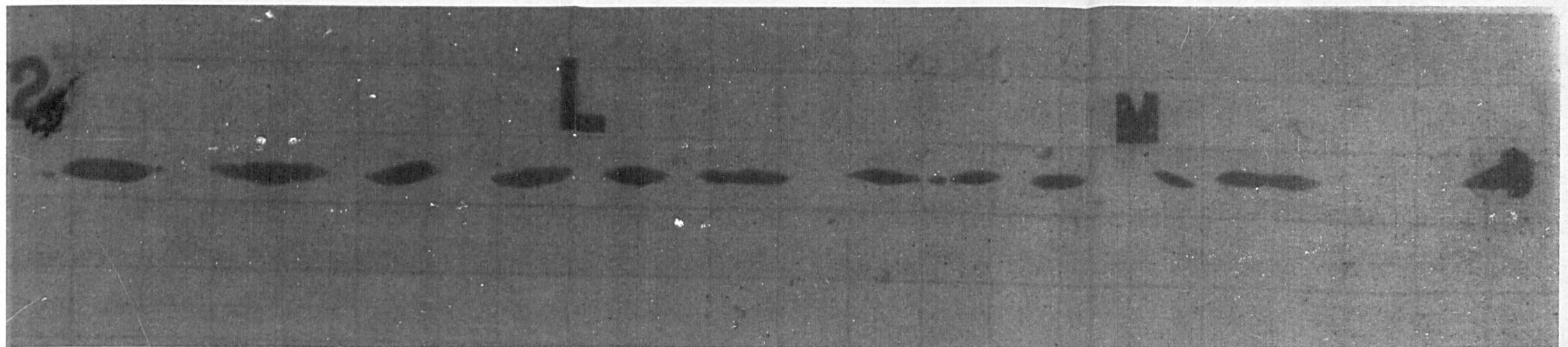
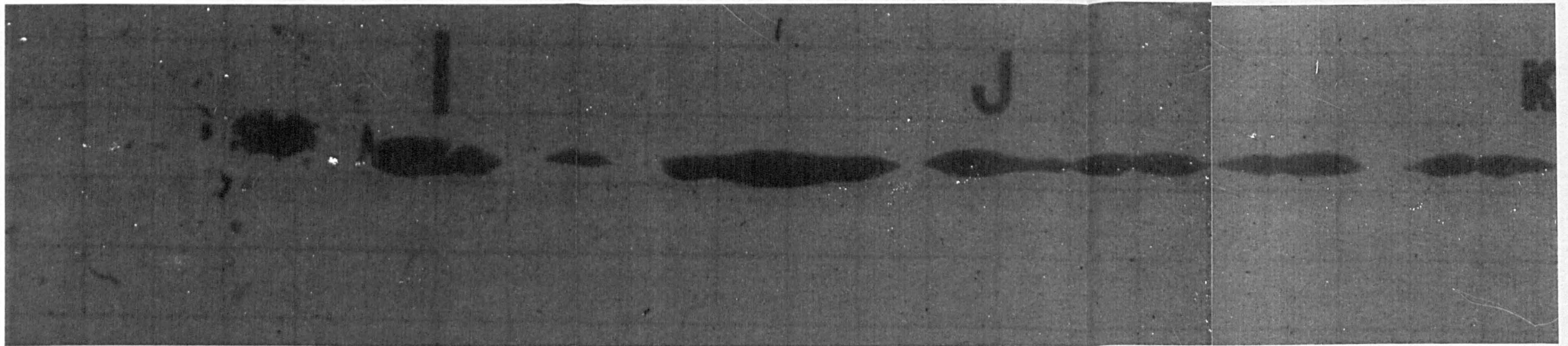


Figure 4.46: Radiograph of partially annealed copper jet "Cu-O", shear spun from annealed plate and then re-annealed. Radiographed  $200.9\mu s$  after detonation

## CHAPTER 5

# Capture of Jet Fragments

### 5.1 Introduction

Two experiments were carried out with the aim of capturing jet fragments for laboratory examination. The principle of the soft recovery pack has been discussed with reference to work by Zernow [49] [50] [51] in Section 2.4.2.

In the first of these experiments low density, solid polyurethane foam was used for the soft recovery pack. This proved to be too dense and no jet fragments were recovered in a recognisable condition. In the second of these experiments low density liquid foam was used and a small quantity of jet material was successfully recovered. A description of this experiment follows.

### 5.2 Experimental Details

#### 5.2.1 The Liner and Warhead Assembly

For this firing a truncated copper liner was used. After shear spinning, the liner was heat treated at 700°C for about 20 minutes. This caused recrystallisation and grain growth - the resulting grains were  $\sim 250\mu m$  in diameter. The material was therefore in a similar condition but with a greater grain size to the shear spun and annealed copper described in Section 4.5. Such liners would normally be expected to break up at an early time and suffer more extensive break-up in comparison to liners with a finer grain size.

The liner was put into a cylindrical case that was hand filled with PE4 explosive and then sealed by the detonator holder plate. Detonation was centrally initiated. The assembled warhead was placed on a firing frame. This consisted of two welded steel plates, one on which to rest the warhead and the other directly in front with a hole cut in the line of flight of the jet. This allowed jet material to pass through unhindered but deflected much of the blast and other debris resulting from the exploding warhead.

### **5.2.2 The Soft Recovery Pack**

Ahead of the warhead and firing frame was the soft recovery pack. This consisted of a 20 meter long polythene tube filled with liquid foam. This was standard fire fighting foam supplied by a tender from the local fire brigade. It was found that leaving the foam to stand for some time (about half an hour) allowed excess water to drain off. This was vented through holes punched in the sides and bottom of the polythene tube.

The foam filled tube was supported at the sides and underneath by blocks of low density polyurethane foam and sheets of straw-board. The foam blocks were purely for structural support. The straw-boards, a high density form of cardboard, were used to record escaping jet material. A photograph of the completed set-up immediately prior to firing is shown in Figure 5.1.

After the firing, the polythene tube was cut open and the jet fragments removed by hand. The jet material was not retained by the foam and had sunk to the bottom of the tube. This greatly facilitated in their retrieval.

## **5.3 Laboratory Analysis of Recovered Jet Fragments**

The copper liner was weighed before firing and found to have a mass of 57 grams. From experience of firings with similar liners, it was possible to predict that about 10 grams of this material would form the jet. In total 2.7 grams of copper, *ie.* liner material, were located in the soft recovery pack.



Figure 5.1: The experimental set-up for soft recovery of jet fragments in liquid fire fighting foam

Seven fragments were recovered whose appearance suggested that they may have been jet fragments. Some other material was also recovered, the origin of which was more difficult to determine. The largest two fragments were sectioned, one parallel to the jets long axis and the other perpendicularly. These were examined by optical microscopy, scanning electron microscopy (SEM) and transmission electron microscopy (TEM).

One sectioned fragment was used for X-ray diffraction analysis. These results could be compared to diffraction data for material from a second liner that had undergone different forming and heat treatment processes, but which had not experienced explosive loading.

### 5.3.1 Observed Features

#### 5.3.1.1 Fragment Size

The seven fragments were between 3 and 10 millimetres long and about 3 to 5 millimetres in diameter. The average mass of the fragments was  $\sim 0.6g$ . This is consistent with the length and breadth measurements made from radiographs, Section 7.2. The two largest fragments were seen in cross section to have become crescent shaped. This phenomenon was reported by Zernow [51] and is attributed to the capture process for tumbling fragments. Figure 5.2 shows a radiograph taken through the solid foam used in the first fragment capture experiment. Tumbling fragments can be seen, some of which appear to be crescent shaped.

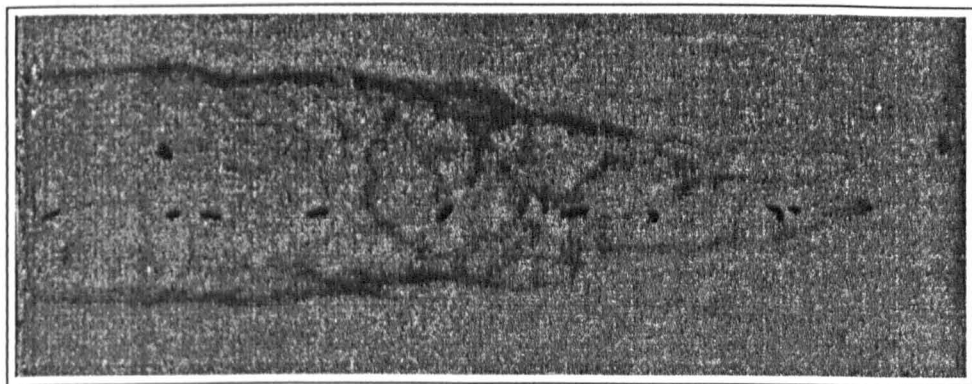


Figure 5.2: Fragments passing through a solid foam target

### 5.3.1.2 Surface Features

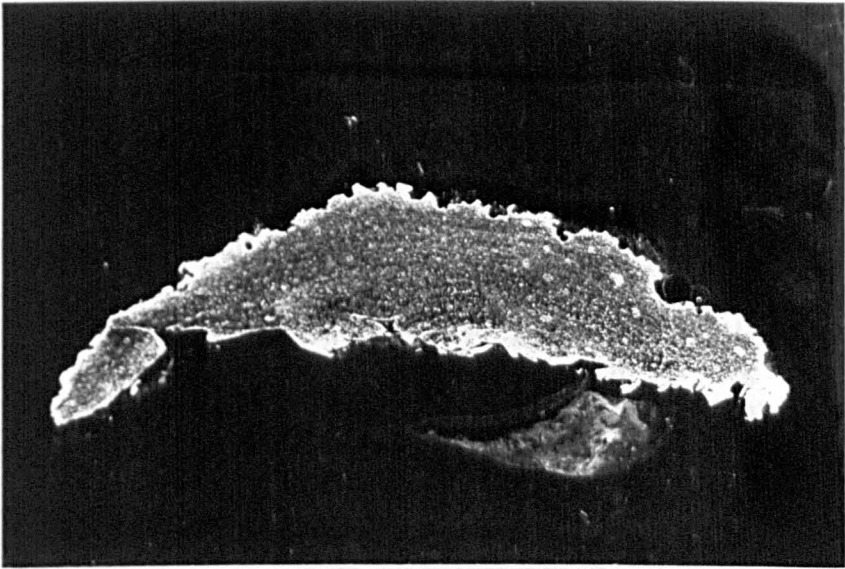
The convex surface of the jet fragments appeared to be very rough in comparison to their concave surface and in comparison to recovered slug fragments from other firings. These had a smooth, drawn or extruded surface finish. It is proposed that this surface appearance was as a result of erosion while travelling through the soft target material by a process analogous to that of sand blasting. There was no evidence to suggest that the fragments had at any time become molten.

### 5.3.1.3 Fracture Surfaces

It would have been interesting to be able to examine fracture surfaces at the tip and tail of each fragment to investigate the actual cause and mechanism of break-up. Unfortunately the erosion process that occurred during capture - in particular those which occurred in the formation of crescent shaped fragments - had erased all evidence of the fracture surfaces. A section through a recovered fragment is shown in Figure 5.3, its crescent shape can clearly be seen. Figure 5.4 shows a magnified view of the region near the tip of the fragment. Here the fine equiaxed grains can be seen in detail, but apart from a very small amount of edge distortion there is no evidence to indicate the fracture mechanism. *ie.* there was no evidence of micro void or crack formation.

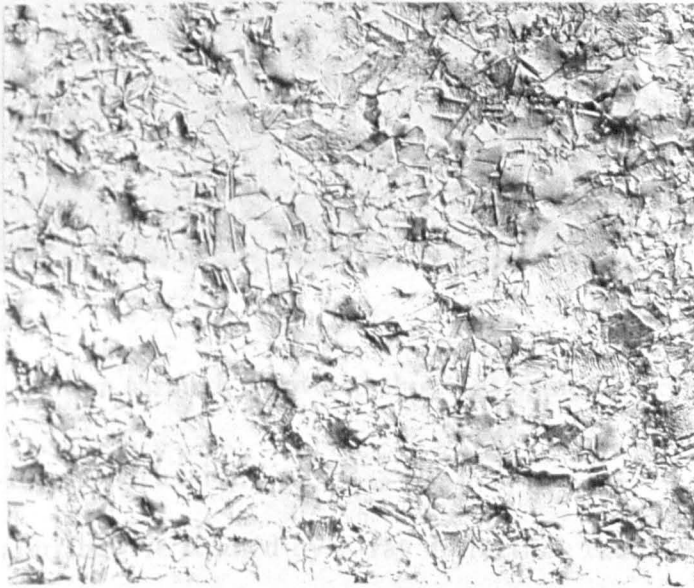
### 5.3.1.4 Grain Size

The average grain diameter of the recovered fragments was found to be less than  $10\mu\text{m}$ , the grain diameter of the original liner material was  $\sim 250\mu\text{m}$ . The  $10\mu\text{m}$  grains were also equiaxed whereas the grains in the original liner were elongated by the shear spinning process. These effects would be expected in a material that had undergone a large amount of deformation and then been sufficiently heat treated to cause recrystallisation but not grain growth.



$\times 9$   $\overline{1mm}$

Figure 5.3: Micrograph of a captured jet fragment that indicates the crescent shape attributed to the soft capture technique



$\times 400$   $\overline{50\mu m}$

Figure 5.4: Detail of microstructure in Figure 5.3

### 5.3.1.5 Other Features

A cavity or pipe has been reported to occur along the central axis of recovered jet fragments, Zernow [51]. This phenomenon was observed in the fragments recovered from this firing. Slugs recovered previously by Hunting Engineering Limited have also exhibited this feature. The pipe is believed to result from the characteristic flow pattern of material during the implosion of a conic liner. It is proposed that the dimensions of the pipe decrease along the length of the jet. The pipe is largest in the tail of the jet, thus making it much easier to find in the slug than in jet fragments. A micrograph of a recovered copper fragment that exhibits a central pipe is shown in Figure 5.5.



$\times 100$   $\overline{100\mu m}$

Figure 5.5: Section through recovered slug that exhibits a central “pipe”

### 5.3.2 X-Ray Diffraction

Five materials were studied by X-ray diffraction, these were;

- (A) Sectioned liner material, grain size approximately  $250\mu m$ .
- (B) Sectioned liner material, cold rolled 50%. Resulting grain size approximately  $350\mu m$ .

- (C) Sectioned liner material, cold rolled 50%, annealed at 650°C for 45 minutes. Resulting grain size approximately 250 $\mu\text{m}$ .
- (D) Captured jet fragment recovered from foam after firing. Initial grain size of liner material approximately 250 $\mu\text{m}$  as for (A). Final grain size of fragment - 20 $\mu\text{m}$ . X-ray beam incident to a surface parallel to the fragments long axis.
- (E) Captured jet fragment recovered from foam after firing, as for (D). X-ray beam incident to a surface perpendicular to the fragments main axis.

In each case the sample material was mounted on a goniometer and measurement of the intensity of diffracted X-rays made from  $2\theta = 10^\circ$  to  $2\theta = 140^\circ$ . The X-ray source comprised of a copper target and a nickel filter that resulted in monochromatic radiation of wavelength 1.5405 $\text{\AA}$ . The plots of diffracted X-ray intensity versus diffraction angle are given in the five figures, Figure 5.6 to 5.10.

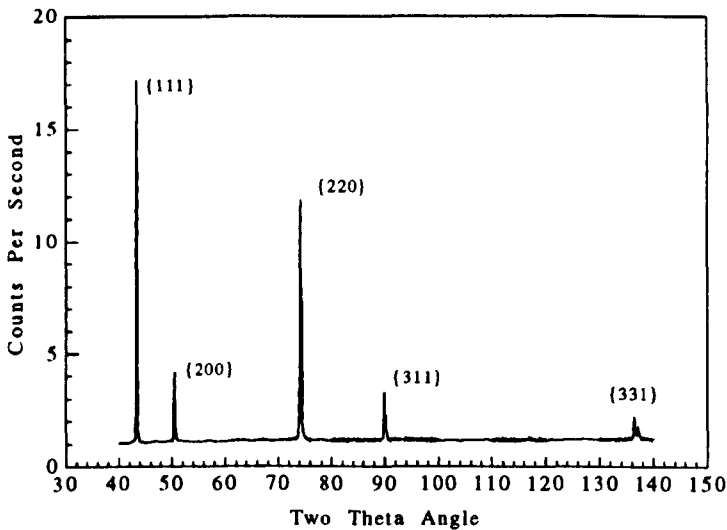


Figure 5.6: X-ray diffraction of sectioned liner material, shear spun and annealed for 12-24 minutes at  $\sim 700^\circ\text{C}$  resulting in 250 $\mu\text{m}$  grain size

Analysis of the X-ray diffraction data was made by comparing the relative intensities of the diffraction peaks with those for the international

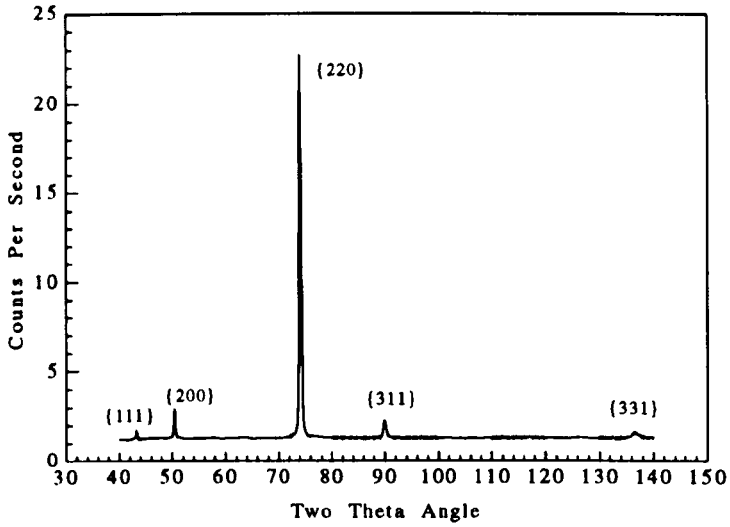


Figure 5.7: X-ray diffraction of sectioned liner material, after cold rolling by 50% resulting in  $350\mu\text{m}$  grain size in the rolling plain

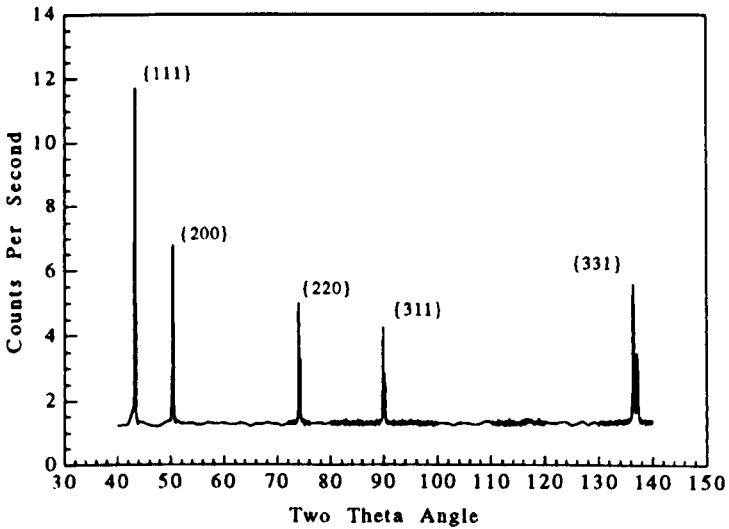


Figure 5.8: X-ray diffraction of sectioned liner material, cold rolled and then annealed for 45 minutes at  $650^{\circ}\text{C}$  resulting in  $90\mu\text{m}$  grain size

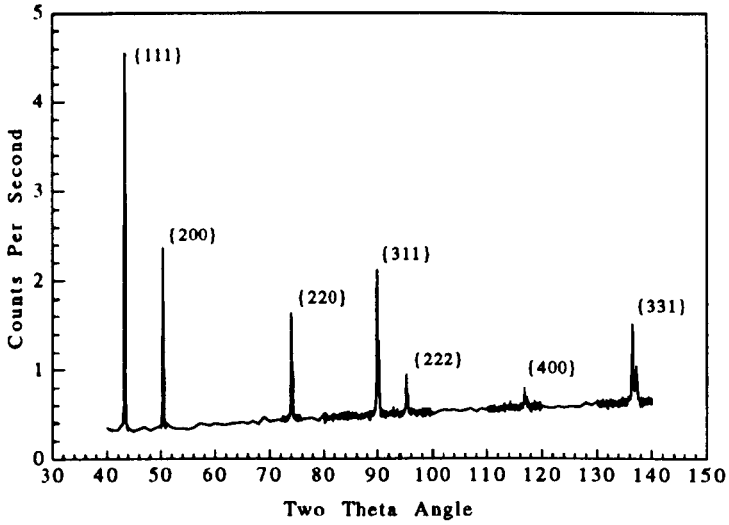


Figure 5.9: X-ray diffraction of captured jet fragment, grain size  $\sim 10\mu m$ . X-ray beam incident to surface parallel to the fragments axis

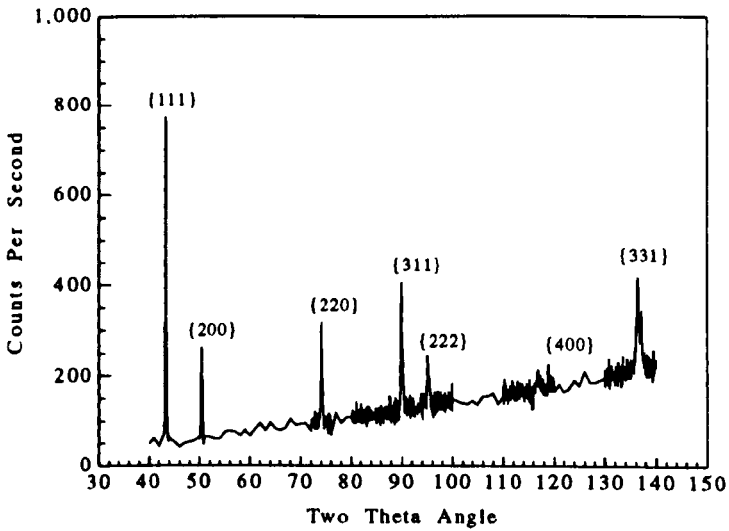


Figure 5.10: X-ray diffraction of captured jet fragment. Grain size  $\sim 10\mu m$ . X-ray beam incident to surface perpendicular to the fragments axis

standards. The largest peak is designated as having an intensity of 100 and all other peaks are expressed as a relative fraction. The sum of all the peak intensities is then used to normalise each set of values. Table 5.1 shows this numerical procedure as applied to the international standard values. Similar calculations are performed for all significant peaks for each of the five materials tested by X-ray diffraction, Table 5.2.

The normalised peak intensity values for each of the five materials are then divided by the normalised peak intensity values for the international standard. Column A, B, C, D and E of Table 5.2 divided by the right hand column - Normalised Intensity - of Table 5.1. This results in a set of values for each material that represent their peak intensities relative to the standard values. These are tabulated in Table 5.3.

Diffraction Angle $2\theta$	Crystal Planes	Relative Intensity %	Normalised Intensity
43.3	{111}	100	0.500
50.4	{200}	46	0.230
74.1	{220}	20	0.100
89.9	{311}	17	0.085
95.2	{222}	5	0.025
116.9	{400}	3	0.015
136.5	{331}	9	0.045
Total		200	1.000

Table 5.1: Normalised peak intensity values for copper international standard

The results of the X-ray diffraction analysis are particularly interesting when the {220} planes are considered. The original shear spun liner material and material which was rolled under laboratory conditions, materials (A) and (B), both have particularly high peak intensities relative to the international standard. This "texture" is known to be associated with rolling - Honeycombe [64]. When the material was annealed the rolling texture was removed. A similar effect was observed for the captured jet fragment. This would suggest that the captured material has been annealed during or after its experience of the jetting process.

Plane	Normalised peak intensities				
	A	B	C	D	E
{111}	0.265	0.060	0.351	0.327	0.350
{200}	0.121	0.107	0.204	0.171	0.137
{220}	0.455	0.735	0.150	0.117	0.125
{311}	0.074	0.082	0.128	0.152	0.169
{222}	0.000	0.000	0.000	0.068	0.067
{400}	0.015	0.000	0.000	0.057	0.027
{331}	0.071	0.016	0.167	0.109	0.126

Table 5.2: Normalised peak intensities for the five materials tested by X-ray diffraction.

(A) Sectioned liner - as-manufactured, (B) sectioned liner cold rolled 50%, (C) sectioned liner cold rolled and annealed, (D) captured jet fragment - tested parallel to axis and (E) captured jet fragment - tested perpendicular to axis

Plane	Relative peak intensities				
	A	B	C	D	E
{111}	0.530	0.120	0.702	0.654	0.700
{200}	0.526	0.465	0.887	0.743	0.596
{220}	4.550	7.350	1.500	1.170	1.250
{311}	0.871	0.965	1.506	1.788	1.988
{222}	0.000	0.000	0.000	2.720	2.680
{400}	1.000	0.000	0.000	3.800	1.800
{331}	1.578	0.356	3.711	2.422	2.800

Table 5.3: Peak intensities relative to the international standard for copper

A rolling texture, {110} <112> with {110} planes in the rolling plane, is indicated by the high relative peak intensities of the {220} planes for the shear spun and rolled materials - column (A) and (B)

The captured jet fragment does not show any strong texture. This would be consistent with material that has been recrystallised. However, it is not consistent with the results published by Jamet [58] and Zernow [49]. In each case their research indicated the fragments had a wire drawing - fibre - texture where the  $\langle 111 \rangle$  and  $\langle 100 \rangle$  directions became oriented parallel to the tensile axis. Had such a texture existed in the fragments resulting from this experiment, it is quite possible that it was subsequently removed when the material recrystallised.

### 5.3.3 Electron Microscopy

Scanning electron microscopy was used to examine jet fragments at high magnifications. It had originally been hoped that details of fracture phenomena could be examined by these means. In particular the fracture surfaces at the ends of the fragments were to be considered. However, these were believed to have been destroyed by erosion as the fragments passed through the soft target material as no features typical of fracture surfaces could be detected. In the regions near the ends of the fragments, large amounts of micro-porosity were found. Zernow [51] has previously made a similar observation.

Transmission electron microscopy did not reveal any unusual features. Subgrains of the order  $1\mu m$  diameter were observed but there was no evidence of a high dislocation density. These observations are consistent with those expected for deformed material that has subsequently been recrystallised.

## CHAPTER 6

# Target penetration

### 6.1 Introduction

Two firings were carried out in order to investigate jet/target interactions. Given that direct investigation of the jet is difficult, it is hoped that analysis of penetration phenomena will give some insight to the mechanisms for deformation at high rates of strain. Previous work carried out on penetration has been mainly concerned with the development of analytical or numerical models. These for the most part contain very little material data other than density and yield stress. Recent work has been involved in determining appropriate values for yield stress at high rates of strain.

A steel plate in each target stack was used to measure volume and dimensional changes caused by penetration. Deformation and displacement of target material was measured by metrology. The volume of the plates was measured using the Archimedes principle of displacement. Radiography and ultrasound techniques were used to search for internal defects. Macrohardness (Vickers) readings were taken at various points and lastly they were weighed. After the firings all these measurements were repeated. A cut away view of the target stack is shown in Figure 6.1. Other plates from the target stack were also investigated specifically for any evidence of mass or volume change.

#### 6.1.1 Design of Charge

Truncated conical copper liners were used for these firings. The liners were 60 millimetres in diameter, had an internal angle of  $60^\circ$  and were



Figure 6.1: Section through multi-laminate target stack after penetration. The penetration was from right to left - note the large entry hole in the first plate. The semi-infinite target is not shown

truncated at their apex. The jet tip usually has a velocity of around  $6\text{mm}\mu\text{s}^{-1}$ . Their design was the same as that used in the fragment capture experiments. These are commercially manufactured devices originally designed by Hunting Engineering Limited. As a well established design, they are known to behave predictably and to produce a jet with consistent characteristics.

### 6.1.2 The Target Stack

The target stack consisted of three sections: a steel section at the front end, mixed materials in the centre section and finally residual "semi infinite" steel. All three sections were placed in a target holder. This was a steel frame with a screw operated clamp with which to keep the plates in place and firmly in contact with each other.

The first section of mild steel target consisted of three plates. These were machined to  $125\text{mm} \times 125\text{mm} \times 20\text{mm}$ . The first and third plates were used as supports on the front and rear of the second plate. The mass of the second plate was recorded using a balance calibrated as accurate to  $\pm 2\text{g}$  in the desired weight range. A matrix of nodes was then marked onto the surface of the plate and the exact position of these nodes measured using automated metrology equipment. Operation of the metrology equipment was carried out by staff of Hunting Engineering Limited.

Five plates,  $125\text{mm} \times 125\text{mm}$ , were used in the mixed material section of the target. The materials and their thickness are presented in Table 6.1. The aim of this section was to study the effect of penetration on materials of different density. The Semi-infinite section of the target was designed to ensure that all jet material was consumed by penetration. They are a safety feature used to contain the jet.

### 6.1.3 Trials Instrumentation

#### 6.1.3.1 X-Rays

Two pulsed X-ray tubes were used to provide in-flight information on these firings. They were placed at two points along the line of flight of the jet. Prior to firing of the shaped charge round, an exposure was

Target Material	Thickness mm	Target section
Mild Steel	25.0	Steel section
Mild Steel	25.0	
Mild Steel	25.0	
Polyethylene	23.5	Mixed material target
Aluminium	25.0	
Mild Steel	20.0	
Aluminium	25.0	
Polyethylene	23.5	
Mild Steel	$\infty$	semi-infinite

Table 6.1: Materials and plate thickness for components of the target stack

made with a grid glass on the line of flight of the jet.

### 6.1.3.2 Trip screens

In the second firing each target plate was separated by a trip screen. These are made of two sheets of copper foil separated and enclosed in adhesive polyethylene film which electrically insulates each sheet from the other and also from the target stack. All the trip screens are held at a high potential and connected to a recording cathode ray tube (CRT) oscilloscope. The sweep generator of the oscilloscope is triggered by the detonator. When the jet penetrates and short circuits trip screens in the target stack, this is recorded by the CRT trace. The times at which the jet passed through particular sections of the target can then be measured directly from the oscilloscope display.

## 6.2 Results

### 6.2.1 Volumetric Measurements

#### 6.2.1.1 Internal inspection

The radiography and ultrasound failed to resolve any internal defects before or after the firings. The limit of resolution for these tests, though,

was limited to the order of a millimetre - therefore only macroscopic inclusions, cracks or voids could have been found.

#### 6.2.1.2 Plate mass

Within the limits of accuracy, better than 0.1%, only the first target plate was found to have had changed its mass, Table 6.2. If it is assumed that the balance used gives repeatable readings, regular calibration records show this to be a reasonable assumption, then the apparent increase in mass of the remaining plates may be due to debris attached to their front and back faces -mainly copper or copper alloy.

The decrease in mass of the first target plate is attributed to the release of shocked material from its free surface. This occurs because tensile forces in this unsupported region exceed the tensile strength of the material. Some portions of the plate are therefore able to break away and the total mass of the plate is decreased. Examination of radiographic images shows this process to be analogous to the "splash" resulting from a more conventional impact of an object onto water.

#### 6.2.1.3 Plate volume

The volume of the target plates has not changed by more than 0.5% (estimated experimental error) The volumes were measured using the Archimedes principle using the same equipment each time, it was hoped that any significant error would be standard and repeatable. However, a non standard error may have been caused by bubbles trapped in the hole following penetration. As much care as possible was taken to avoid this.

#### 6.2.1.4 Hole volume

An attempt was made to measure the volume of the hole produced in the target plates. This was done by running water from a burette into the cavity through its exit hole while its entry hole was sealed. The potential for error involved with this measurement was large due to the rough and deformed plate surface which makes it difficult to achieve a good fit to the hole profile. It is therefore possible that the measured volume will comprise a portion relating to deformation as well as to penetration. The

Plate number	Initial mass g	Final mass g	Balance g
First firing			
2	3488	3491	+3
Second firing			
1	3490 *	3466	-24
2	3485	3487	+2
3	3490 *	3492	+2
4	508 *	497	-11
5	1519 *	1521	+2
6	3490 *	3487	-3
7	1519 *	1523	+4
8	508 *	499	-9

Table 6.2: Calculated and measured plate masses

The limit of accuracy of the balance was found to be  $\pm 3\text{g}$ . An \* denotes that the mass quoted was calculated from the plates dimensions results for the measured hole volumes are presented in Table 6.3.

### 6.2.2 Metrology of target plates

Metrology allows the displacement of material to be measured, *ie.* the changes in dimension due to deformation. It was found that the target plates had become thicker in the region where the jet had penetrated - this approximates to the centre of the plates. At their edges there were virtually no changes in dimension. The change in thickness of the plates can be used to calculate the volume of material displaced from the hole. A simple model of the plates was used in which each of their faces was considered to be a four sided pyramid. The volume of displaced material on each side of the plates was then given as one quarter the height of the pyramid times the square of its base. The sum of these values will give the volume of the hole. These calculated values are presented in Table 6.3 and are found to be in good agreement with the values measured previously.

Plate number	Calculated volume (cc)	Measured volume (cc)	
		Firing 1	Firing 2
1	8.0	13.5	15.5
2	4.0	5.0	4.0
3	3.5	5.0	5.1
4	1.0	4.3	4.1
5	2.7	-	2.6
6	1.4	3.7	1.7
7	2.7	1.2	2.6
8	1.0	3.2	1.4

Table 6.3: Calculated and measured hole volumes

### 6.2.3 Microhardness Testing

Each of the target plates was cut roughly in half through the centre of the hole. This material was then further sectioned to produce standard specimen mounts of material from the immediate vicinity of the penetration. The aluminium samples were mounted in cold setting resin to avoid becoming heat treated by the automated mounting process. All specimens were ground and polished to a one micrometre grit.

Strings of microhardness indents were made at different locations, starting adjacent to the hole and moving towards the edge of the target plate in a direction normal to the penetration. The distance between each indent was measured optically using the microscopes graduated eye-piece. As the plates were known to have been rolled a string of readings was also taken parallel to the direction of penetration close to the edge of the hole. For comparison some points in the bulk material of the plate were also tested. All indents had been made using a fifty gram load and all readings were consistent for different locations on the specimens. *ie.* There was no difference recorded in the change in hardness moving away from the hole whether measurements were taken adjacent to the entry or exit points on the plate or from any point in between.

It has been found that although the hardness values are numerically different for steel and aluminium, the profile of hardness versus distance

curves can be qualitatively compared. There are several general features common to most sets of results: The surface of the hole was lined with an alloy of copper from the jet and material from the target plate - this alloy had a very high hardness. Target plate material adjacent to the internal edge of the hole has been softened by recrystallisation. There is a peak of hardened material approximately one millimetre from the edge of the hole. The hardness falls off gradually with increasing distance into the plate. These observations are schematically represented in Figure 6.2.

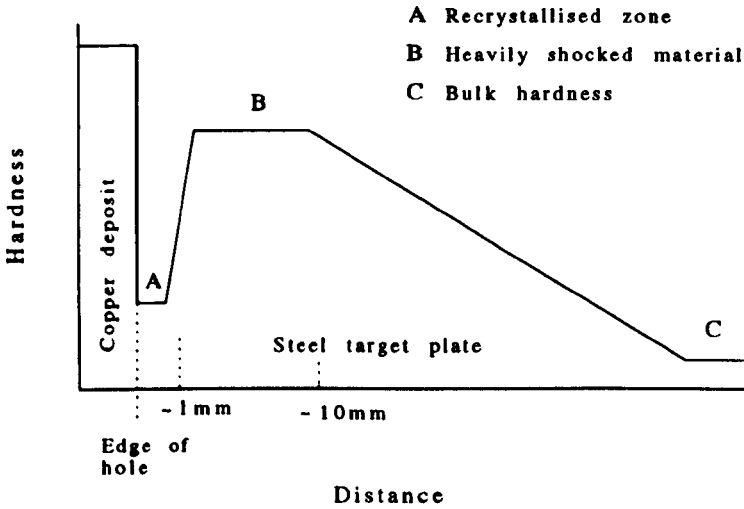
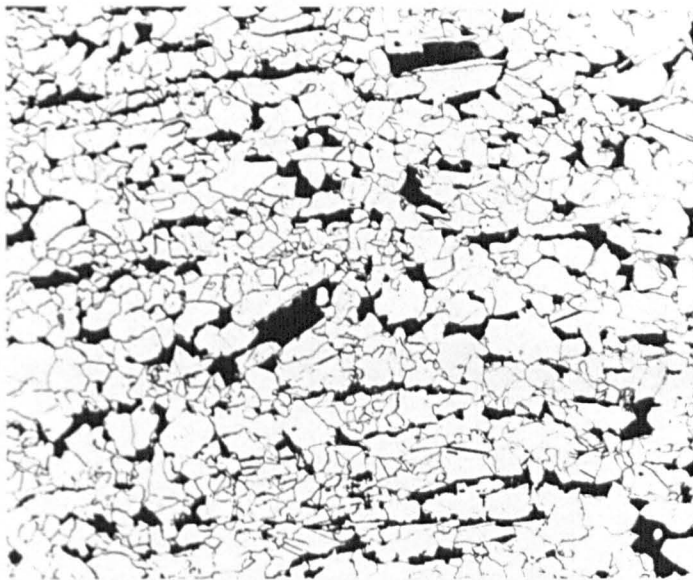


Figure 6.2: Schematic diagram of hardness versus distance from the hole resulting from jet penetration

From these results it is clear that the target has been severely work hardened over the first millimetre surrounding the hole and to a decreasing extent further into the target plate. In a limited number of sites the surface of the hole was not lined by the alloy of copper and target plate material. In these cases the softened region of target close to the hole could not be found, thus suggesting that the deposition of the alloy had annealed a thin annulus of material adjacent to the hole.

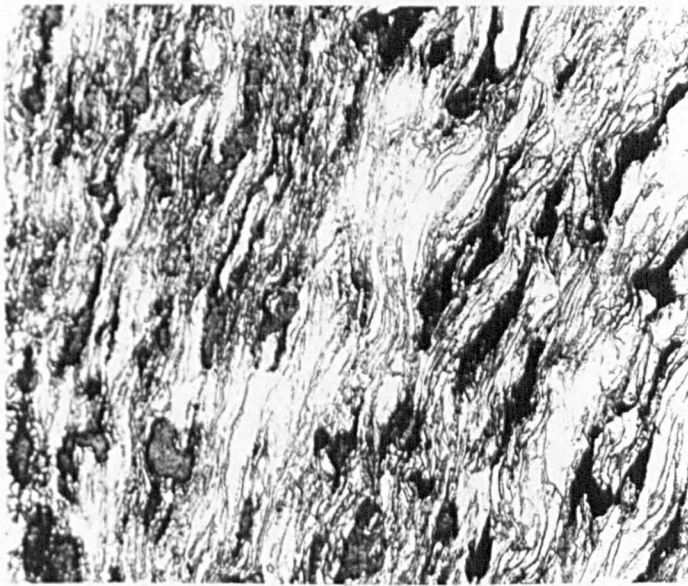
#### 6.2.4 Metallography

Metallography has shown that the steel at the outside edge of the plate was virtually undeformed, Figure 6.3. Twins or Neumann bands found in these areas show that the material has been shock loaded. However, the density of these is low therefore they cannot have contributed greatly to the total strain. Close to the hole - but not immediately adjacent to it - the material was shocked to a much greater extent. The twin or Neumann band density was correspondingly high in this region. It was this part of the plate in which the greatest thickening occurred in the direction parallel to the penetration. Deformation was seen to be as a result of grain elongation, Figure 6.4. Even in a heavily shocked region, Neumann band formation would not have been a significant mechanism for deformation to occur.



$\times 200$   $\overline{100\mu m}$

Figure 6.3: Micrograph of shocked steel taken some distance from the hole



$\times 200$   $\overline{100\mu m}$

Figure 6.4: Micrograph of heavily shocked steel taken adjacent to the hole

## CHAPTER 7

# Measurement of Jet Fragments In Flight

### 7.1 Introduction

In this chapter an attempt has been made to rationalise the observed jet break-up characteristics. The assumption that jets from different liner materials are comparable is to be verified on the basis of the information gained during break-up.

It has been observed that jets break-up into different sized fragments depending on the liner material from which they originate. It might be thought that the length of the fragments is a characteristic parameter which will be constant for a particular material and determined by its materials properties. To test this hypothesis the length of jet fragments was measured from the radiographic images presented in Chapter 4. The measured values are presented in Figures 7.1 7.2 and 7.3.

Fragment length was found to be an acceptable parameter. However, it was observed that the breadth of jet fragments also varied for different liner materials. Utilising both the length and breadth terms meant that the fragments' volume could be calculated and their mass found by multiplying the materials density. A revised hypothesis is proposed which uses fragment mass as the characteristic parameter for jet break-up. With break-up defined in terms of fragment mass this approach to jetting becomes consistent with other models, *eg.* the Pugh - Eichelberger - Rostoker (PER) [9] theory which defines jet formation in terms of mass flow - see Equation 2.6.

## 7.2 Limitations of X-ray Photographic Imaging

Initially, measurement of the fragments was made by hand from photographic contact prints of the X-ray negatives. This was found to be an unsatisfactory process as the image quality of the radiographs made it difficult to achieve a high degree of accuracy. The X-ray tubes were approximately three meters from the line of flight of the jet and could be considered as distant point sources of illumination. Therefore they should have projected sharp images of the jets onto the film but certain factors reduced the final image quality.

Low contrast radiographs were the consequence of the extreme experimental conditions, which included the level of protection required by the X-ray film and the very short exposure time allowed to produce a still frame of a particle travelling at up to  $6\text{ mm}\mu\text{s}^{-1}$ . Aluminium plate  $3\text{ mm}$  thick plus a light proof polythene bag were used to surround the X-ray film whilst the exposure time was  $\sim 30 \times 10^{-9}$  seconds. The very intense burst of high energy X-rays were able to penetrate the thinner portions of the jet fragments, *ie.* their edges, which resulted in poor edge definition.

Image contrast was improved by use of high contrast film and operation of the X-ray sources at minimum energy values  $\sim 200\text{ KeV}$  for the available system, in order to reduce the penetration of X-rays. The single exposure technique developed for firings described in Section 3.3 resulted in the best overall improvement in image contrast.

## 7.3 Digital Image Analysis

Measurement of jet particles was greatly facilitated when image analysis equipment became available. The X-ray negatives were placed on a light box and digitally scanned, thus cutting out the intermediate step of producing a positive print. For calibration at a later stage, a transparent rule was placed on the light box with the negatives. The digital

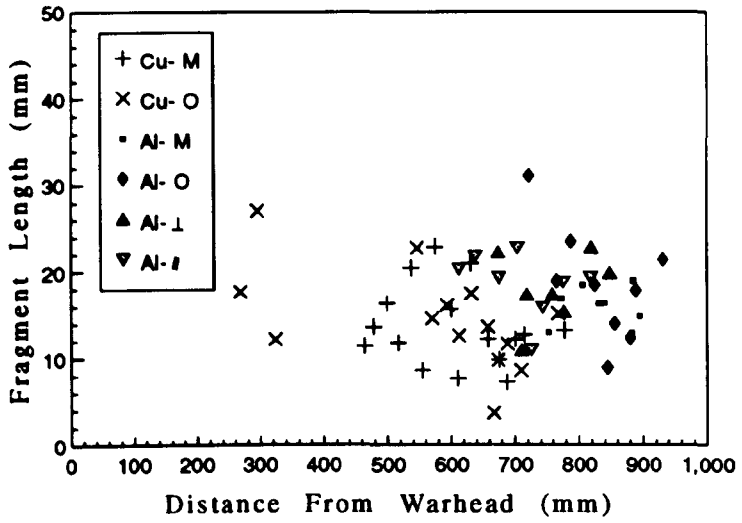


Figure 7.1: Jet fragment length resulting from pure aluminium and copper liners

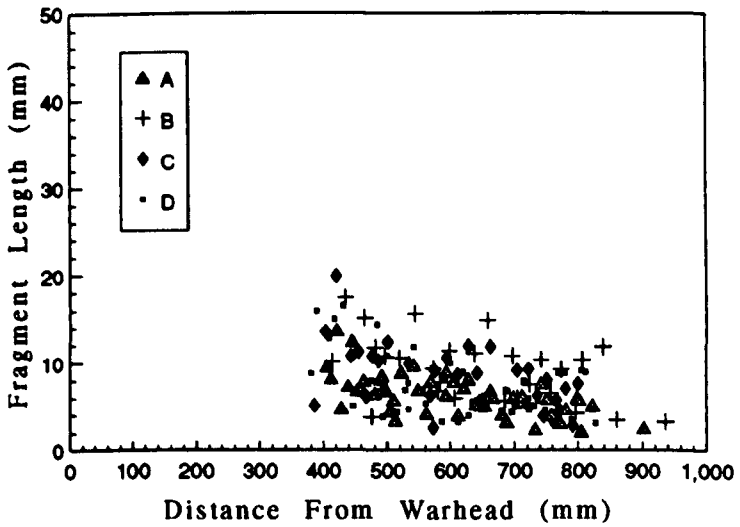


Figure 7.2: Jet fragment length resulting from aluminium - magnesium alloy liners

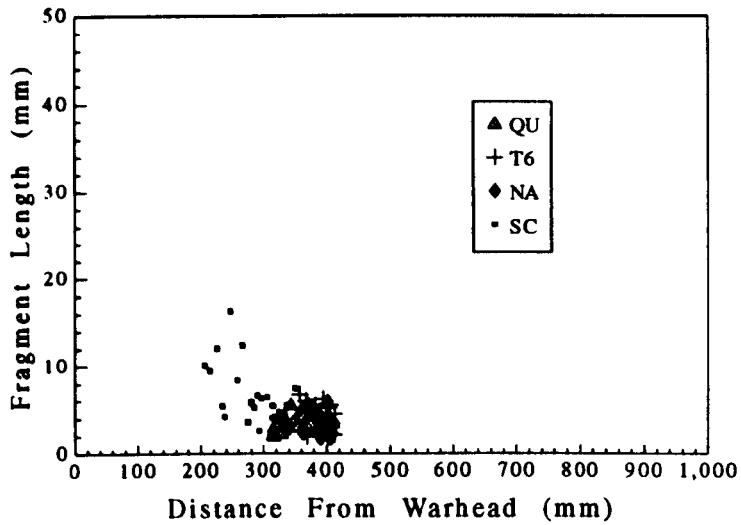


Figure 7.3: Jet fragment length resulting from aluminium - copper - magnesium - alloy liners

information was stored as a 256 grey level bit map. This categorised each image as a  $768 \times 576$  array of pixels (dots). Each pixel was described by a brightness value in the range 0 - for black to 255 - for white. The advantage of this system was that the jet fragments could be "seen" numerically, this meant that some of the analysis process could be automated. The human eye is very sensitive but its analysis is subjective and not repeatable.

Firstly a noise reduction filter was passed over the numerical images, this reduced or eliminated speckle type detail. These resulted from local abrupt changes in the contrast level. Meanwhile, gradual changes in contrast were left unchanged. Next, a Sobel filter was used to detect changes in contrast. Regions in which there was a significant change in contrast level became bright, while those areas where the contrast was constant became dark. The effect was to remove most of the image while leaving bright halos where the edges of particles had been detected. The image was next converted to a binary format and, for clarity, the centres of the halos were filled in to create a silhouette image of the solid particles. These images were shown in Chapter 4.

Measurement of the particles length and breadth, and their X and Y coordinates relative to the top left of the image were made automatically by the image processing software. The software was able to calibrate these measurements by reference to the image of a rule digitised at the same time as the X-ray negatives. The data was passed on to spreadsheet software for further manipulation:

- Where a jet had been recorded over more than one image it was necessary to link data sets such that the X and Y coordinates became continuous
- Scaling was carried out with reference to calibration markers
- The jets velocity gradients were plotted
- The average volume and mass of jet fragments were calculated

## 7.4 Velocity Gradients

The velocity gradients were calculated by finding the position of jet fragments in two images taken at known times. The difference in position divided by the difference in time yields the fragments velocity. When the velocity for each fragment in a jet is known, the gradient in velocity between the jets tip and tail can be found. It is a characteristic of shaped charges with straight sided conic liner profiles that the velocity gradient is linear.

It was assumed that the jets would form in a similar manner regardless of their liner material, thus making their subsequent break-up characteristics simpler to compare. To make firings of copper, aluminium and aluminium alloys as similar as possible, all firings were carried out using the same design of charge and detonation system. Their liners were of the same mass - differences in density were compensated for by changing the thickness of the liner.

The values plotted in Figure 7.4 show that all the copper, aluminium and aluminium - magnesium alloy jets had very similar velocity gradients. This implies that the jet formation process was similar in each case, *ie.* the time for collapse, the rate of flow of liner material and, by

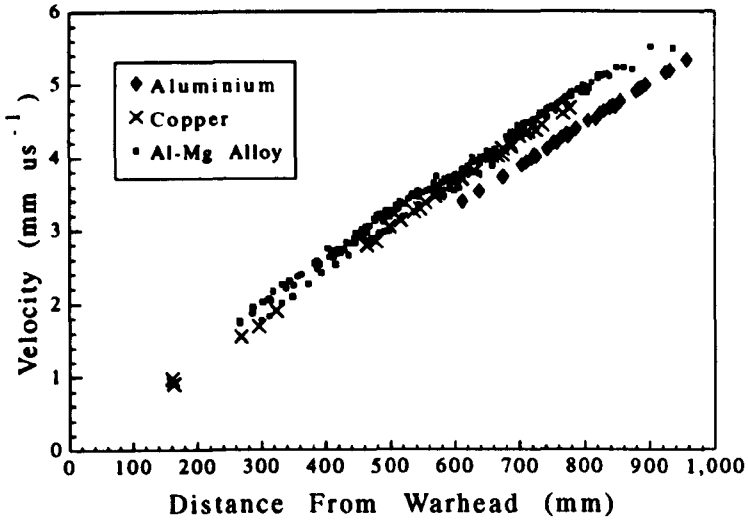


Figure 7.4: Velocity gradients for copper, aluminium and aluminium - magnesium alloy jets

inference of the Pugh, Eichelberger, Rostoker (PER) theory [9] (Equations 2.4 and 2.6), the proportion of mass making up the jets were all similar. Results for aluminium - copper - magnesium alloys are not plotted here because their radiographs were recorded at different times. It can be assumed that as these firings were also carried out under similar experimental conditions, the jets would have formed in a similar manner and would have had similar velocity gradients.

## 7.5 Quantification of Jet Break-Up

The data collected by image analysis was not in a form which allowed for comparison of the jet break-up characteristics. In the following sections various manipulations of this data will be discussed with a view to finding a format in which useful comparisons of the different jets can be made. However, firstly there are two assumptions required to make further data manipulation rational.

The radiographic images of jets recorded all available material regardless of whether this was a true jet. Material from the slug or partially formed fragments originating from the end of the collapse process were

included in many images. In order that the slug and partially formed fragments do not confuse the analyses to be carried out on jet material, only those fragments with a velocity greater than  $2.5\text{mm}\mu\text{s}^{-1}$  will be considered.

The “foot” at the tip of the jet will also be disregarded as this is believed to be created by inconsistent velocity conditions during the initial stages of jet formation. Computer modelling of jet formation by Hunting Engineering Limited predicts there to be an inverse velocity gradient at the beginning of the jet formation process, *ie.* the first jet material to emerge from a collapsing liner does so at a lower velocity than the material that follows. These conditions rapidly reverse as the jet formation process becomes established, however, the material with the highest velocity catches up with the original jet tip and agglomerates to form the “foot”.

### 7.5.1 Jet Fragment Volume and Mass

Given the measured sizes of the jet fragments and the assumption made in Section 7.4 that the proportion of liner mass in each of the jets would be similar, the volume of the jet fragments was calculated. To do this the fragments were assumed to be rods with a circular cross section, no account was taken of irregularities in fragment shape. The average mass of each jet fragment was then calculated by multiplying its volume by the materials density. This assumes that the fragments do not contain any voids. The calculated values are presented in Table 7.1. In Section 5.3.1.1 recovered copper fragments were found to have an average mass of  $\sim 0.6\text{g}$ . This is lower than the values in Table 7.1 however the measured mass of these fragments does not include errors due to assumptions about fragment shape or material which has been eroded in the capture process. The distribution of fragment mass along the length of the jets is plotted in Figures 7.5, 7.6 and 7.7.

### 7.5.2 A Quantitative Jet Parameter

Given the assumption that the jets resulting from liners with similar geometry and mass have similar velocity characteristics, then the mass of jet fragments is a suitable quantitative comparator. However, the break-up is uniquely identified according to the dimensions of the resulting

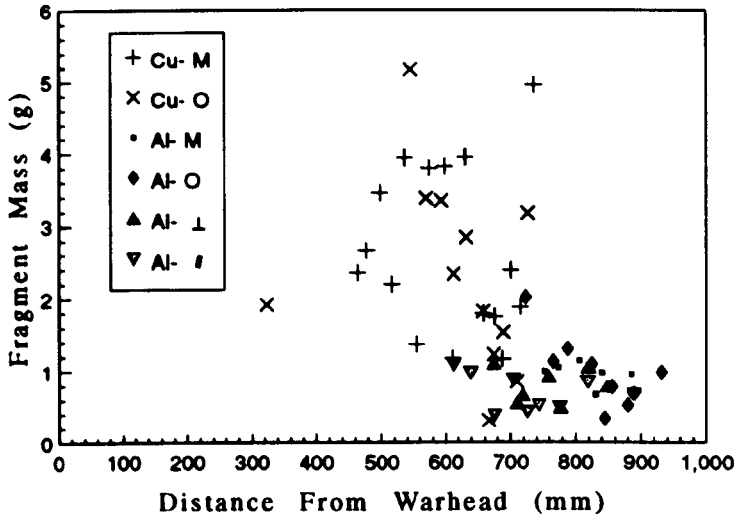


Figure 7.5: Fragment mass distribution along pure aluminium and copper jets

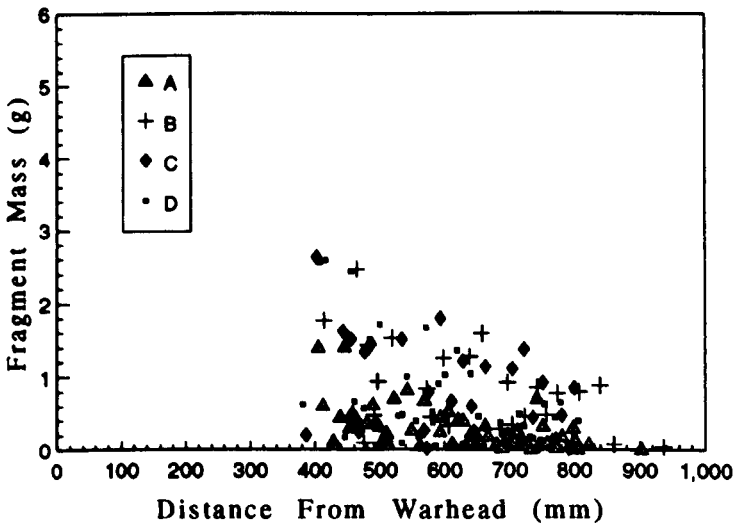


Figure 7.6: Fragment mass distribution along aluminium - magnesium alloy jets

Firing reference	Average volume (mm <sup>3</sup> )	Standard deviation ( $\sigma_{n-1}$ )	Calculated mass (g)
<b>Pure aluminium and copper</b>			
Cu - M	298.9	126.8	2.67
Cu - O	260.8	143.7	2.33
Al - M	333.3	59.6	0.90
Al - O	363.0	172.6	0.98
Al - ⊥	292.7	82.2	0.79
Al -	258.1	94.9	0.70
<b>Aluminium - magnesium alloys</b>			
A	377.2	378.0	1.02
B	315.7	295.8	0.86
C	151.5	202.1	0.41
D	266.3	368.8	0.72
<b>Aluminium - copper - magnesium alloys</b>			
QU	21.0	19.0	0.06
T6	26.0	25.5	0.07
NA	24.0	28.5	0.07
SC	152.1	256.8	0.41

Table 7.1: Calculated average mass of jet fragments

Density of copper taken to be 8920 Kg m<sup>3</sup>, aluminium and aluminium alloys 2710 Kg m<sup>3</sup>. Variations in density due to alloying are very small and were therefore considered inconsequential given the assumptions made while calculating the fragment volume.

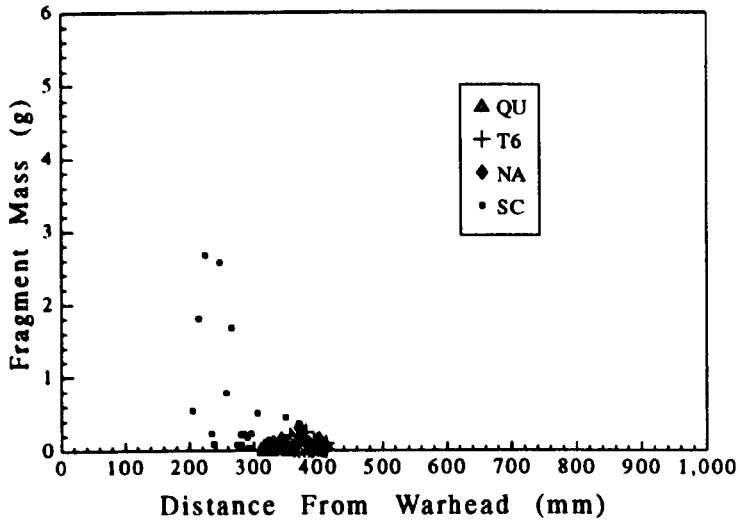


Figure 7.7: Fragment mass distribution along aluminium - copper - magnesium alloy jets

fragments. Using the original values of fragment volume without including the density term results in a parameter which is dependent solely on the geometry of the jet fragments. The difference between comparisons of jets by mass and volume parameters results from differences in density. Hence, using the mass parameter separates the results for copper and aluminium while the volume parameter appears to unify them. It might be assumed that a single relationship could be described to relate the volume of jet fragments to a mechanical property of face centre cubic metals. However, with only two results available for copper this cannot be proved and in the following sections the mass of jet fragments will be used to analyse the effect of certain materials properties on jet break-up.

If the fragment volume distribution along pure aluminium and copper jets are plotted, the average fragment volume is seen to be similar for both materials. This is shown in Figure 7.8. However, the PER theory [9] predicts that for shaped charges of similar liner geometry the mass of the jet should be consistent. The apparent conflict this creates is due to the times at which the radiographic images of the jets were taken. The copper jets were completely fragmented after  $\sim 200\mu s$  and therefore all jet fragments could be measured. In contrast a large proportion of

the pure aluminium jets had not fragmented at this time. Therefore the measured aluminium fragments represent only a proportion of the volume or mass of the entire jet.

It is postulated that if the mass of the aluminium and copper jets are similar - as predicted by the PER theory - and the average fragment volumes are similar - indicated by the measured values plotted in Figure 7.8 - then the number of fragments in each jet must be related by the ratio of the materials density.

$$\text{Number of Al fragments} = \frac{\rho_{Cu}}{\rho_{Al}} \times \text{Number of Cu fragments}$$

It might therefore be anticipated that comparison of the average fragment volume would allow materials of any density to be described by a single straight line relationship. This cannot at present be verified due to a lack of data for materials of different densities which also have a wide range in materials properties. Assuming that the relationship was valid a comparison of the average fragment mass would produce a set of parallel lines for different materials. The spacing of these lines would be related to the materials densities.

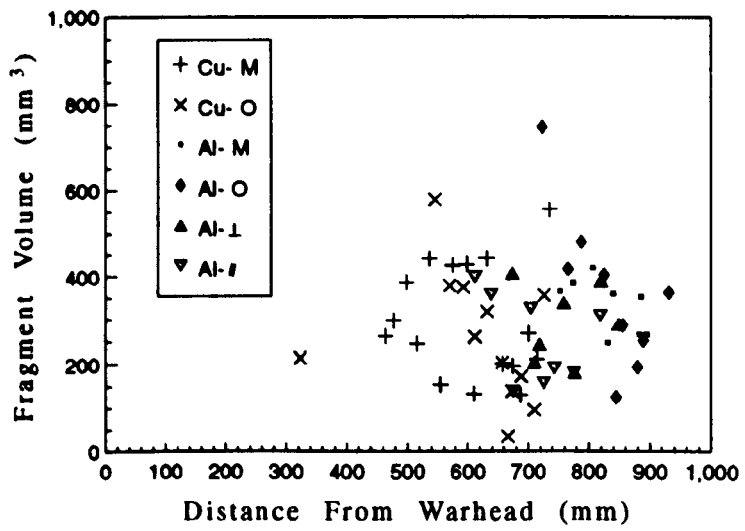


Figure 7.8: Fragment volume distribution along pure aluminium and copper jets

## CHAPTER 8

# Lateral Velocity Induced by Shear

When a jet breaks-up the material is probably under conditions similar to a uniaxial tension test. The principle applied force is parallel to the axis of the jet and forces perpendicular to the axis are resultant not applied. If a jet is assumed to be in uniaxial tension and the failure mode is predominantly through shear, then at failure there is a resultant component of the axial force which acts in a perpendicular direction. Conventionally shear forces act symmetrically in all directions. In pure metals of circular cross section this results in the formation of a point when ductile tensile failure occurs. However, in less ductile materials catastrophic failure may occur when deformation takes place on just one shear plane. This asymmetric failure would then result in an induced lateral velocity, the magnitude of which can be estimated if the following assumptions are made;

- The jet is in uniaxial tension
- The failure mode is pure shear
- Shear occurs at  $45^\circ$  to the main axis of the jet on a single plane (in a polycrystalline material this is a geometric plane not a lattice plane)
- shear failure occurs at a stress equal to half the quasi static ultimate tensile stress (UTS) of the jet material
- Shear occurs through the movement of dislocations
- Dislocations move at approximately the speed of sound - sonic velocity - of the jet material

- The continuous jet (that which has not broken-up) is assumed massive, such that a force acting perpendicularly to the axis of the jet as a result of shear will cause a lateral velocity in a jet fragment but no lateral velocity in the continuous jet. This assumption allows lateral velocity to be considered as the result of only one shear fracture.

The force acting along the axis of a jet which has diameter  $D$  is given by

$$F_{(axial)} = \sigma_{(UTS)} \times \pi \times \left(\frac{D}{2}\right)^2 \quad (8.1)$$

The resultant component of force acting in a perpendicular direction is given as a function of the force acting along the jet axis where  $\theta$  is the angle between the axis and the direction of shear,

$$F_{(perp)} = \cos \theta \sin \theta \times F_{(axial)} \quad (8.2)$$

The acceleration,  $a$ , resulting from an applied force is given by the Newtonian equation

$$a = \frac{F}{m} \quad (8.3)$$

where  $m$  is the mass of the jet.  $m = \rho \times \pi \times \left(\frac{D}{2}\right)^2 \times L$

The lateral velocity is then given by another Newtonian equation,

$$V = U + at \quad (8.4)$$

where  $U$  is the initial lateral velocity, which is zero, and  $t$  is time. The time taken for shear in the jetting case will be very small and approximate to the time taken for wave front travelling at the jet materials sonic velocity to cut through the thickness of the jet. Given the speed of sound in copper and the assumed diameter of the jet this gives a time for shear of

$$t = \left(\frac{D}{V_{(sound)}}\right) \quad (8.5)$$

Combining Equations 8.1, 8.2, 8.3, 8.4 and 8.5 yields an expression for lateral velocity,

$$V_{(Lateral)} = \left(\frac{\cos \theta \sin \theta \sigma_{(UTS)} \pi \left(\frac{D}{2}\right)^2}{2\rho \pi \left(\frac{D}{2}\right)^2 L}\right) \left(\frac{D}{V_{(sound)}}\right) \quad (8.6)$$

this simplifies to,

$$V_{(Lateral)} = \left( \frac{\cos \theta \sin \theta \sigma_{(UTS)}}{2\rho L} \right) \left( \frac{D}{V_{(sound)}} \right) \quad (8.7)$$

Using this equation with the numerical values in Table 8.1 yield estimated values for lateral velocity of  $0.25\text{ms}^{-1}$  in high purity aluminium and  $1.5\text{ms}^{-1}$  in a high strength 2014 aluminium alloy in the T6511 condition.

		High Purity Aluminium	2014-T6511 Alloy
UTS (MPa)	$\sigma_{UTS}$	90	540
Density	$\rho$	8920 Kg m <sup>-3</sup>	
Sonic Velocity	$V_{(sound)}$	5 mm $\mu\text{s}^{-1}$	
Jet Diameter	$D$	5 mm	
Fragment Length	$L$	10 mm	

Table 8.1: Values used to illustrate the effect of ultimate tensile stress (UTS) on lateral velocity

This estimated value of lateral velocity is small compared to those which cause poor jet performance. A lateral velocity of  $30\text{ms}^{-1}$  would be considered damaging to jet performance but would not be unexpected in a non-precision round. However, it is shown that as the materials ultimate tensile strength increases the potential lateral velocity which may result from an asymmetrical shear failure also increases. This analysis therefore indicates that break-up could contribute to the effect of lateral velocity but that it is unlikely to be the sole cause. The tolerances applied to the manufacture and assembly of rounds is known to significantly effect the jets lateral velocity.

## CHAPTER 9

# Discussion

### 9.1 Introduction

Analysis of the radiographic images gave details of the size and position of jet fragments at a given stage in their flight. This is discussed in Chapter 7. As images had been recorded at several known times for each jet, it was possible to calculate the velocity of the fragments. The jets velocity gradients are considered in Section 7.4. Further analysis was carried out in Section 7.5 to produce a "Jet Parameter". This allowed the break-up characteristics of each jet to be compared in relation to the mechanical properties of their liner material. This analysis is discussed in Section 9.2. In Section 9.3 a theoretical analysis of dislocation deformation mechanisms at very high rates of strain is discussed and a model for the break-up of shaped charge jets is put forward.

### 9.2 Materials Properties in Relation to Jet Break-Up

It has been noted that different materials have different jetting characteristics. This is empirically stated as "Pure ductile metals produce the best jets". The "best" jets are those which break-up at the latest times, into large ellipsoidal fragments and which result in the greatest penetration into armour. The experiments carried out in this study have set out to make a more thorough investigation of the relationships between a jets break-up characteristics and certain mechanical properties of the related liner.

The first observation to be made from the results of the jet experi-

ments was that the high strength alloys fractured earlier and into smaller particles than the low strength pure metals. Time was not a measured break-up parameter, however this statement can be justified by consideration of the radiographic images of two jets. A pure aluminium jet radiographed  $\sim 200\mu s$  after detonation, see Figure 4.11 for example, has broken-up along about half of its length. In contrast an aluminium - copper - magnesium alloy jet, *eg.* L168-T6511 radiographed  $\sim 100\mu s$  after detonation - Figure 4.37 - is seen to be fragmented along its entire length.

### 9.2.1 Ultimate Tensile Strength and Proof Stress

Figure 9.1 shows the values of fragment mass for each jet, as tabulated in Table 7.1. These are plotted at the value of ultimate tensile stress, UTS, corresponding to that which was measured for the original liner material. Figure 9.2 shows the values of fragment mass versus proof stress. The range shown for each value is the standard deviation of the fragment mass. Two possible relationships can be observed for fragment mass versus UTS/proof stress. In the first case the fragment mass decreases with increasing stress values. This is indicated by the regression of values as shown in Figures 9.1 and 9.2. In addition there is a trend exhibited by certain aluminium - copper - magnesium alloys such that their fragment mass is insensitive to stress values. This is particularly evident for the proof stress of material in the naturally aged and T6511 heat treated condition, firing references T6 and NA.

The insensitivity of certain aluminium alloys is attributed to the effect of early break-up. It is postulated that the fracture of these materials has occurred early due to a catastrophic shear failure and therefore curtailed ductile deformation. This implies that the maximum measured stress in these cases was only an "experimental" UTS. Had catastrophic failure not occurred then deformation may have continued to greater "theoretical" values of stress and strain. However, these "theoretical" stress/strain values might never be attainable in practice.

It was found that the fragment mass decreases as the UTS/proof stress of the liner material increases. This relationship can be observed for pure aluminium and aluminium alloys and is assumed to be similar for copper. If the assumptions made in Section 7.5.2 are correct, the relation-

ship between the mass of copper fragments and UTS/proof stress should result in points which lie about a line parallel to that for aluminium. If this were true, then it would be possible to use fragment volume as the parameter for jetting characteristics. Using fragment volume would appear to result in a single relationship of fragment volume to UTS and proof stress (and probably other materials properties). However, with only two available data points for copper this cannot be certain. Therefore fragment mass will be used as the parameter for jetting characteristics. In the following analyses on the effect of materials properties, relationships will only be considered for aluminium and aluminium alloys.

The effect of proof stress was specifically considered by firings with pure aluminium. Firing references Al - O, annealed condition; Al - M, as manufactured condition; Al -  $\perp$ , as-manufactured with grain alignment perpendicular to the extrusion direction; and Al -  $\parallel$ , as-manufactured with grain alignment parallel to the extrusion direction. The UTS and strain to failure were similar for both Al - O and Al - M, however annealing reduces the proof stress. Figure 4.3 shows the stress versus strain curves for these materials. Similar differences in mechanical properties were achieved without heat treatment by Al -  $\perp$  and Al -  $\parallel$ . Figure 4.4 shows the stress versus strain curves for these materials. The results show that for both Al - O and Al - M and also for Al -  $\perp$  and Al -  $\parallel$  the materials had similar differences in proof stress and similar differences in their resulting fragment mass.

On a microscopic scale the grain structures of these materials were different. The annealed material had large equiaxed grains while the as-manufactured material had elongated and textured grains. These may contain residual stress due to the presence of dislocation substructures remaining after the extrusion process. However, some recovery and recrystallisation has taken place which will have diminished these residual stresses. A texture may also have resulted from the alignment of specific crystal planes by the deformation process. Grain shape and size, textural components as well as residual stresses enhance the proof stress in specimens aligned parallel to the extrusion direction. Therefore, depending on heat treatment or orientation the materials exhibited three distinct grain morphologies and differential effects due to texture and residual stresses. Consideration of Figure 9.2 shows that for the pairs of materials, (Al - O and Al - M) and (Al -  $\perp$  and Al -  $\parallel$ ) the effect of changing

these strengthening factors is to decrease the proof stress. This appears to cause an increase in their resulting fragment volume.

### **9.2.2 The Grain Size Effect**

The effect of changes in grain size on yield or proof stress can be described by the Hall - Petch equation - Equation 4.1. Taking as an example pure annealed copper with a fine grain size and copper of similar composition but with a larger recrystallised grain size. The material with the finer grain size would have a correspondingly high yield stress and hence high proof stress, therefore it might be anticipated that the resulting fragment mass would be reduced. Bourne [65] has shown that this is not the case. The fine grained material would result in larger more elongated fragments, *ie.* fragments of greater mass, despite the greater proof stress. Research by Hunting Engineering Limited with single crystal liners shows these materials to result in jets which break-up earlier and subsequently elongate to a lesser extent despite very low yield stress values.

It has been reported by Dieter [66] that reducing the grain size results in increased ductility. However, no evidence is given to support this claim. (Dieter cites work by Carreker [67] but the published results conclude no discernable effect of grain size on ductility). The amount of work hardening may increased as a result of more dislocation interactions at grain boundaries. However, fine grains cause deformation to be more dispersed in the material by activating a larger number of slip systems. The amount of deformation to occur on any one slip plane is therefore reduced and as a result the magnitude of local stress concentrations is also reduced. Reducing local stress concentrations reduces the number of sites available to initiate the formation of either micro cracks or voids and hence increases the ductility in comparison to that of material with large grains.

An additional phenomenon associated with single crystals and large grained materials is that of longitudinal break-up. This appears to be a single fracture in the direction parallel to the jets axis. It is therefore a limited form of the incoherency phenomenon - see Section 2.2.3.1. In Chapter 5 it is reported that some jet elements are found to contain a pipe along their central axis. This which is believed to be characteristic

of the materials flow pattern caused by the implosive collapse of a shaped charge liner. This pipe may be the cause of longitudinal break-up in large grained material. Fine grained material is apparently unaffected by this phenomenon.

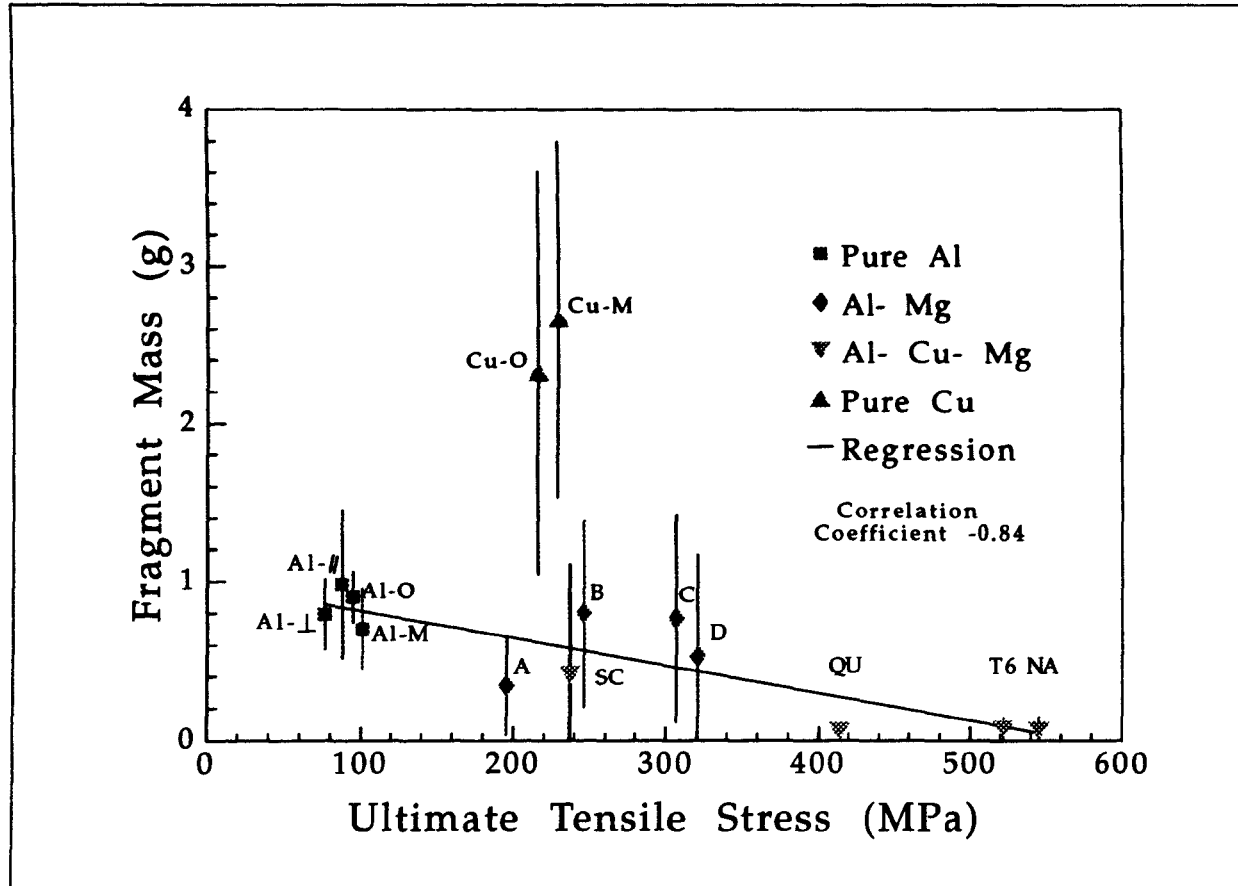


Figure 9.1: Fragment mass versus ultimate tensile strength

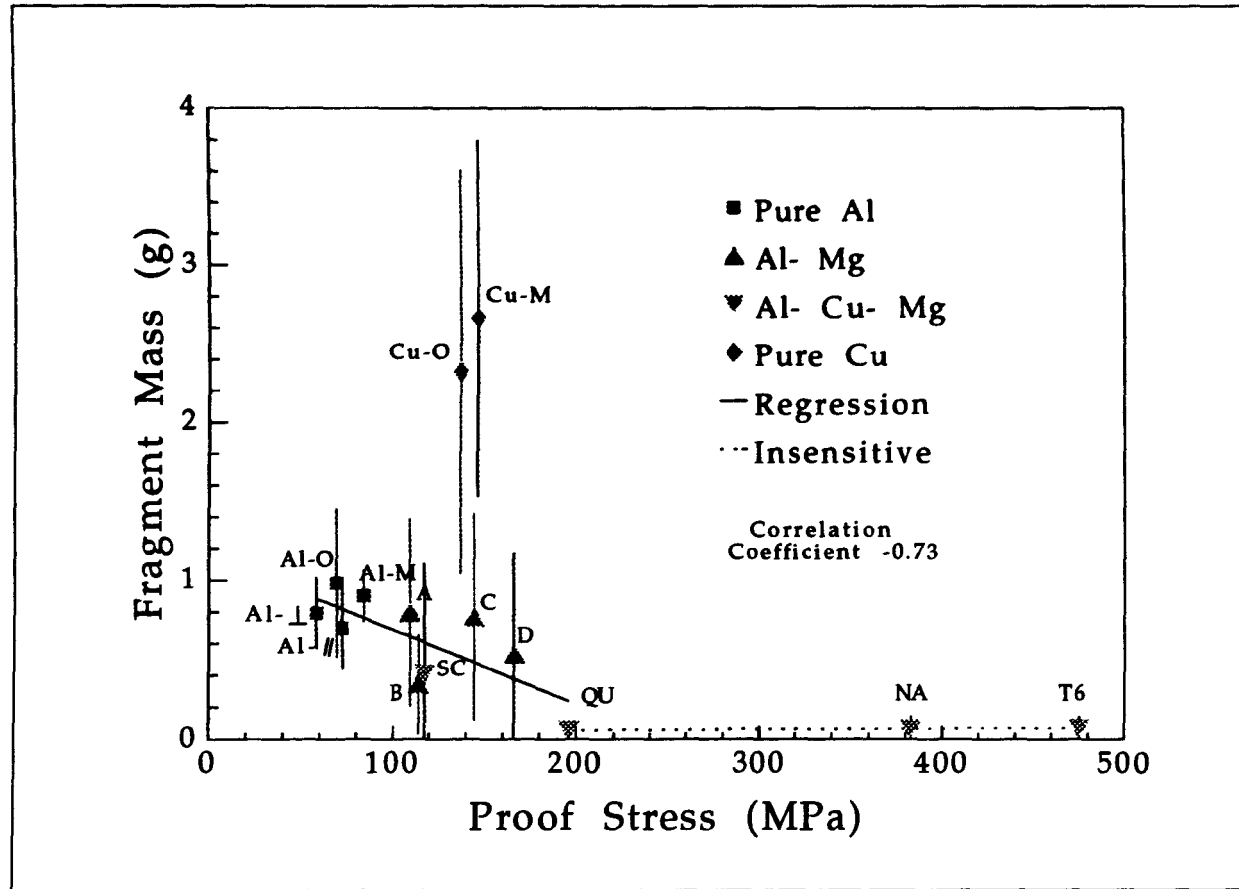


Figure 9.2: Fragment mass versus proof stress

### 9.2.3 Work Hardening

Certain work hardening characteristics allow a metal to sustain large uniform elongations. The relationship between true stress, true strain and the coefficient of work hardening,  $n$ , is expressed by Equation 9.1. The value of  $\sigma_0$  is obtained simultaneously with the value of  $n$  by taking logs of Equation 9.1 -  $n$  is the gradient and  $\sigma_0$  is the intercept at  $\ln \epsilon_t = 0$  on the log/log plot, i.e. at a high strain value of  $\epsilon_t = 1$ .  $\sigma_0$  is representative of the materials resistance to deformation and is expressed as the stress at a constant value of strain which would usually exceed the true fracture stress. It is conditional that  $n$  is less than one and greater than zero.

$$\sigma_t = \sigma_0 \epsilon_t^n \quad (9.1)$$

The nominal stress versus strain curves presented in Chapter 4 can be converted to true stress - true strain curves for data which does not exceed the UTS by Equations 9.2 and 9.3 - note that  $\sigma_n$  is the nominal stress and  $\epsilon_n$  is the nominal strain. The only assumption required for these expressions is that for deformation prior to the UTS, constant volume is maintained.

$$\epsilon_t = \ln(\epsilon_n + 1) \quad (9.2)$$

$$\begin{aligned} \sigma_t &= \sigma_n \times \exp(\epsilon_t) \\ &= \sigma_n (\epsilon_n + 1) \end{aligned} \quad (9.3)$$

Values of the coefficient of work hardening have been calculated from true stress - true strain data derived for the relevant materials. True strains at UTS are tabulated along with these values for the coefficient of work hardening and  $\sigma_0$  in Table 9.1

The rate of work hardening is found by differentiating Equation 9.1, this yields

$$\frac{d\sigma}{d\epsilon} = \sigma_0 n \epsilon_t^{n-1} \quad (9.4)$$

Firing reference	Coefficient of work hardening, $n$	True strain at UTS <sup>(1)</sup> $\epsilon_{t(UTS)}$	$\sigma_0$ (MPa)	Rate of work hardening at UTS <sup>(2)</sup>
Pure aluminium				
Al - O	0.184	0.189	145.9	104.5
Al - M	0.124	0.134	140.4	101.3
Al - $\perp$	0.242	0.181	141.3	124.9
Al - $\parallel$	0.199	0.180	173.4	136.3
Aluminium - magnesium				
A	0.217	0.151	345.9	329.8
B	0.253	0.112	482.0	625.8
C	0.264	0.127	613.2	739.3
D	0.212	0.117	576.8	663.2
Aluminium - copper - magnesium				
T6	0.089	0.095	759.8	577.3
NA	0.209	0.178	1035.8	847.9
SC	0.255	0.127	482.4	572.3
QU	0.325	0.173	970.1	1030.4
Pure copper				
Cu - O	0.359	0.297	492.6	385.1
Cu - M	0.365	0.320	529.7	398.6

(1) True strain at UTS or at failure, which ever occurred first

(2) Calculated using Equation 9.4

Table 9.1: Coefficient of work hardening and true strain values

### 9.2.3.1 Effect of the Coefficient of Work Hardening

An analysis has been carried out to consider the effect of  $n$ , the coefficient of work hardening on the shape of the stress versus strain plots. Some model curves of true stress versus true strain with different values of  $n$  are shown in Figure 9.3. These illustrate the effect of the coefficient of work hardening at a constant value of  $\sigma_0$ . The values of  $\sigma_0$  presented in Table 9.1 are in the range  $\sim 100 \rightarrow \sim 1000$ MPa, therefore for the purposes of this illustration an intermediate value of 500 MPa has been used.

From the relationships of stress and strain it is possible to show that

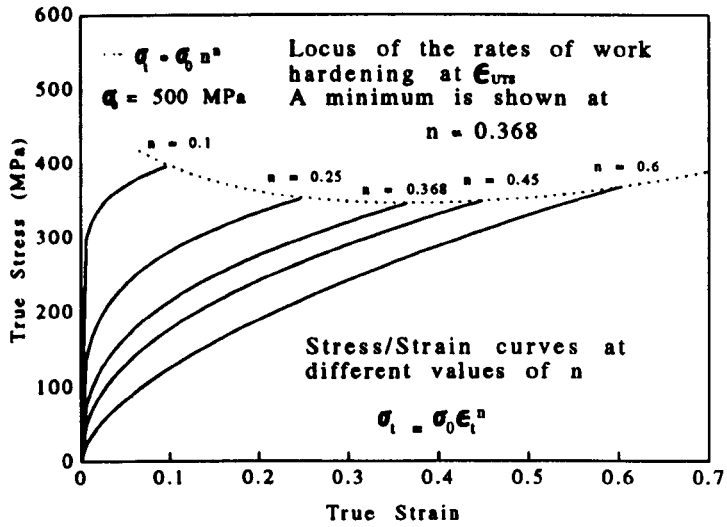


Figure 9.3: Model true stress versus true strain curves with different values of work hardening coefficient

the strain at the UTS is numerically equal to the value of the coefficient of work hardening. First though, it is necessary to recognise that at the UTS Equation 9.5 can be used to describe the rate of work hardening. Uniform deformation can only occur while the rate of work hardening is greater than the applied stress. At the UTS the rate of work hardening becomes insufficient to resist the increase in applied stress due to geometric softening and necking is initiated.

$$\frac{d\sigma}{d\epsilon} = \sigma_{t(UTS)} \quad (9.5)$$

The value for true strain at the UTS can then be found by substituting Equation 9.5 into Equation 9.1 and then substituting the resulting expression into Equation 9.4. This strain,  $\epsilon_{UTS}$  represents the maximum uniform elongation which can occur prior to the onset of necking.

$$\epsilon_{UTS} = n \quad (9.6)$$

For a constant value of  $n$  the rate of work hardening decreases with increasing strain. This is represented by Equation 9.4 and in Figure 9.3

by the decreasing gradients of the stress/strain curves. However, the maximum uniform elongation occurs at the UTS and therefore the rate of work hardening is limited at this point. Hence, in Figure 9.3 the line describing the rates of work hardening intercepts each stress/strain curve at its UTS value. Substituting Equation 9.6 into Equation 9.5 and 9.1 yields the following relationship

$$\left(\frac{d\sigma}{d\epsilon}\right)\bigg|_{\epsilon=\epsilon_{UTS}} = \sigma_0 n^n \quad (9.7)$$

Taking natural logs and differentiating Equation 9.7 yields an expression which has a minimum in the range  $0 \leq n \leq 1$ , Equation 9.8. It is assumed that  $\sigma_0$  is a constant.

$$\frac{d \left[ \ln \left( \frac{d\sigma}{d\epsilon} \right) \bigg|_{\epsilon=\epsilon_{UTS}} \right]}{dn} = \ln n + 1 \quad (9.8)$$

Thus, solving Equation 9.8 gives a value for  $n^*$  the coefficient of work hardening which results in the minimum rate of work hardening at the UTS for a constant value of  $\sigma_0$ .

$$\begin{aligned} \ln n^* + 1 &= 0 \\ \ln n^* &= -1 \\ n^* &= e^{-1} \\ &\simeq 0.368 \end{aligned}$$

This phenomenon is graphically represented in Figure 9.3. A dotted line curve shows the locus of rate of work hardening values - defined by Equation 9.7. It can be seen that the minimum rate of work hardening at the UTS strain occurs when  $n \simeq 0.368$ . It is interesting to note that none of the values for  $n$  given in Table 9.1 are greater than 0.368.

### 9.2.3.2 Relationships between Work Hardening Characteristics and Jet Break-Up

For the materials under investigation, their coefficients of work hardening are plotted versus fragment mass in Figure 9.4. This shows a regression line which indicates that the fragment mass increases as the coefficient of work hardening decreases. However, this is seen to be a very weak relationship. As was seen in the plot of fragment mass versus proof stress, the fragment mass of the aluminium - copper - magnesium alloys when in the T6511 and naturally aged conditions are insensitive to their values of work hardening coefficient. This is attributable to early break-up where the experimental UTS occurs prior to the theoretical UTS. As a result the strain at the experimental UTS is also much lower.

A possible reason for the difference between the calculated coefficient of work hardening and the measured true strain at the experimental UTS may be explained by the appearance of the resultant fracture surface. When the difference in values of  $n$  and  $\epsilon_{UTS}$  was small the fracture of tensile specimens exhibited large reductions in cross sectional area and a ductile fracture surface which has resulted from void coalescence, *ie.* classical necking. This was the case for the pure aluminium and pure copper. When the difference in values of  $n$  and  $\epsilon_{UTS}$  increased, less ductile fractures occurred. The fracture surfaces of the tensile specimens now contained fewer voids and became increasingly faceted. The faceted surfaces were at approximately  $45^\circ$  to the tensile axis which indicated failure through shear. The reduction in area of these specimens was limited in comparison to that associated with the pure metals. In the most extreme cases, *eg.* the aluminium - magnesium alloy containing  $\sim 4.5wt\%$  Mg, the fracture surfaces were reduced to one single flat plane at  $45^\circ$  to the tensile axis - see Figure 4.13. These materials also showed the least amount of elongation prior to fracture in jet formation and also appeared to fail through shear at  $45^\circ$  to the jet axis.

The values of  $\sigma_0$  are plotted versus fragment mass in Figure 9.5, where  $\sigma_0$  is representative of the materials resistance to deformation. This shows that as the materials resistance to deformation increases so their fragment mass decreases.  $\sigma_0$  determines the stresses acting along the length of the jet. As the stresses acting on the jet increase, break-up will occur after reduced amounts of elongation and with greater frequency

along the length of the jet.

With both values for  $n$  and  $\sigma_0$  calculated from the derived true stress true strain data, the rates of work hardening can be found from Equation 9.4 and these are shown in Figure 9.6. For the aluminium and aluminium alloys there is a relationship between fragment mass and the rate of work hardening at the experimental UTS. As the rate of work hardening increases the fragment mass decreases. Thus, the rate of work hardening may provide the most accurate description of the relationship between materials properties and jet break-up.

It was observed in Figure 9.4 that the value of  $n$  for any of the pure aluminium samples is significantly lower than 0.368. The elongation to UTS for aluminium is also low in comparison to those for pure copper. This is as a natural consequence of Equation 9.6. The values of  $\sigma_0$  for these aluminium specimens are also very low as are their rates of work hardening. However, the relationship expressed by Equation 9.7 suggests that if the value of  $n$  could be increased towards 0.368 then the rate of work hardening would decrease and consequently the elongation to UTS of these materials could be increased. This is evidently not the case for the copper, as both results for the work hardening coefficient are already very close to 0.368. This results in the minimum contribution by the value of  $n$  to the value for the rate of work hardening.

It is postulated that these effects may result from differences in purity between the copper and the aluminium samples. The copper samples used were phosphor deoxidised non arsenical grade with a minimum of  $\approx 99.85\%$  copper. Therefore, the most likely impurities will be copper phosphides. The maximum solubility of phosphorus in copper is approximately  $2\text{wt}\%$  at  $715^\circ\text{C}$  this gradually decreases to less than  $0.5\text{wt}\%$  at  $300^\circ\text{C}$ . Therefore, on freezing from the melt most copper phosphide will remain in solid solution. Any remaining copper phosphide will be forced to precipitate onto grain boundaries due to segregation. With very few precipitate strengthening mechanisms present the work hardening rate in pure copper is low and the coefficient of work hardening approaches 0.368. Conversely "pure" aluminium often contains a dispersion of precipitates throughout its bulk. The minimum required purity of the 1050 grade material was  $99.5\%$  aluminium. The major impurity in this form of aluminium is usually iron which forms an intermetallic with very low

solubility - 0.052wt% at 655°C which very rapidly decreases to virtually nil at 400°C Hansen [68]. Due to their limited solubility these intermetallic particles are formed throughout the grains and causes a high rate of work hardening. The reduction in uniform elongation which occurs as a result of the presence of these inclusions and impurities is indicated by a decrease in the values for  $n$ , see Table 9.1.

### 9.2.3.3 Stacking Fault Energy

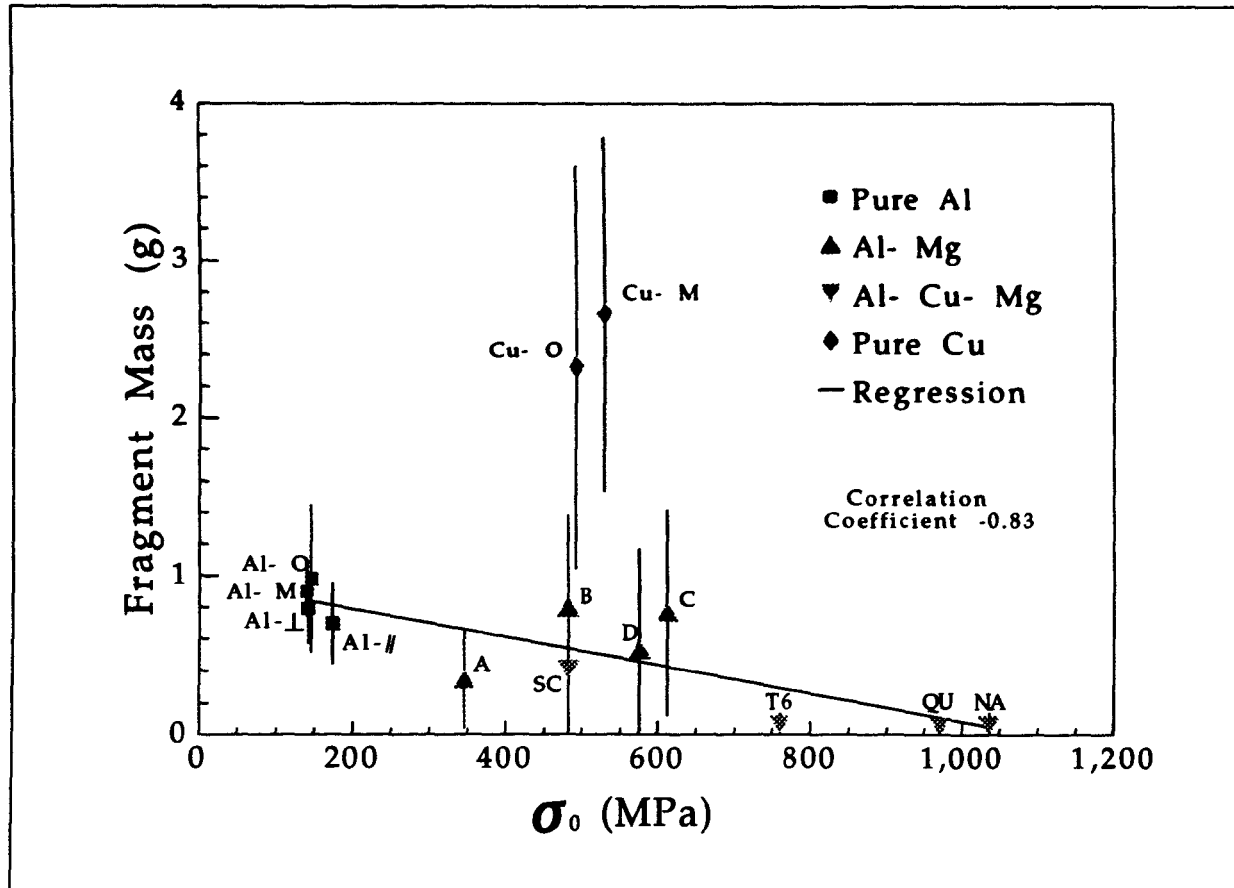
Considering high purity metals where impurities and inclusions are small in number, there is little opportunity for them to act as physical obstacles to dislocation motion. Some dislocation - dislocation interactions are governed by the stacking fault energy of the metal concerned. This value represents the energy per unit area of the plane between two partial dislocations created by the disassociation of one whole dislocation. As the stacking fault energy decreases the separation of the partial dislocations increases and it becomes harder for the partial dislocations to re-associate. Stacking fault energies for some pure metals are given in Table 2.3.

The movement of a coupled pair of partial dislocations occurs only on one specific slip plane. In order for the dislocation to change slip direction and move on any other slip plane in the slip system, *eg.* to cross slip, the two partial dislocations must re-associate. The whole dislocation is then free to change its slip direction after which it may once again disassociate. Therefore, in materials with a low stacking fault energy cross slip is difficult to achieve due to the large separation of partial dislocations. A reduced ability to cross slip results in greater work hardening, *ie.* the coefficient of work hardening,  $n$ , is increased. These effects are clearly demonstrated by aluminium and copper. Aluminium has a high stacking fault energy, its partial dislocations have a small separation, cross slip occurs easily and there is little work hardening effect. The average value of  $n$  calculated for aluminium was 0.187. Copper has a lower stacking fault energy and this results in a high value for the coefficient of work hardening, the average calculated value of  $n$  for copper was 0.362.

It has been shown that the rate of work hardening has a minimum at the UTS when the coefficient of work hardening is 0.368 and that the greatest fragment mass results from materials with the lowest rate

of work hardening. Therefore, it is proposed that the metals with the lowest stacking fault energies are those which will result in jets with the greatest elongation.



Figure 9.5: Fragment mass versus  $\sigma_0$

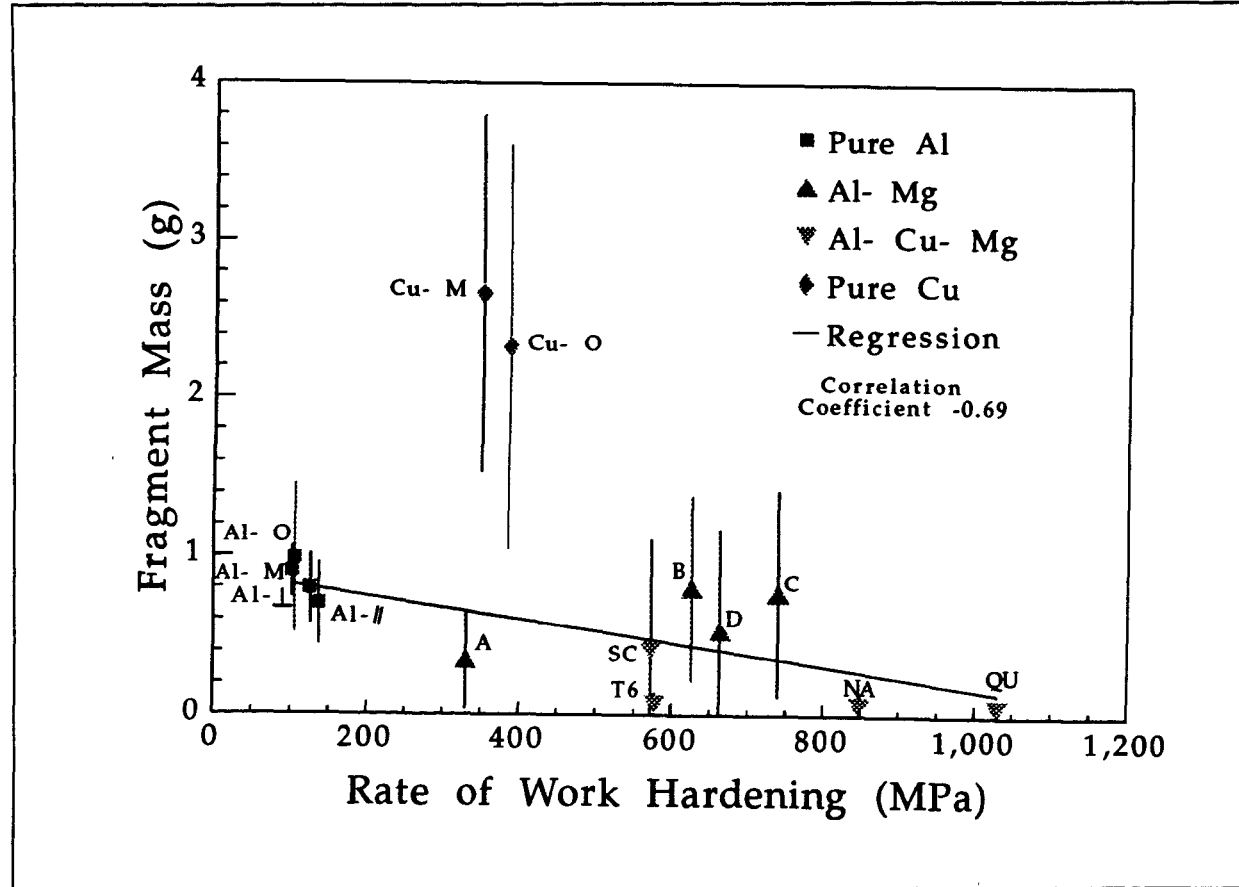


Figure 9.6: Fragment mass versus rate of work hardening

## 9.2.4 Elongation

Absolute values of elongation are influenced by the geometry of the tensile specimens from which the measurements were taken. This effect is particularly important when the relative values of uniform elongation to the UTS and total elongation to failure are considered. As the gauge length of the tensile specimens increases the relative proportion of the uniform elongation becomes greater. This is because fracture under laboratory conditions is a localised effect. For a constant cross - sectional geometry, the elongation which occurs between the UTS and failure is approximately constant. Meanwhile, the amount of uniform elongation is directly proportional to the specimens gauge length. Other geometric factors are also important. Elongation measurements taken from sheet specimens with rectangular cross section may yield different results to those from specimens with circular cross section. All the tensile testing conducted on aluminium and aluminium alloys used specimens of similar geometry, details are given in Appendix B. The most significant difference between laboratory tensile tests and the break-up of shaped charge jets is that the jets suffer multiple fractures. This greatly increases the relative importance of elongation which occurs between the UTS and the final failure.

A materials strain to failure is the sum of two parts; the uniform elongation prior to necking and the unstable deformation during the development of a neck. Figure 9.7 shows the strain at failure, this is the sum of the strain at UTS - Figure 9.8 - and the strain between UTS and failure - Figure 9.9. These indicate that the ductility of the material is directly related to its jetting characteristics. It is evident that these materials properties which have been evaluated at intermediate strain rates under laboratory conditions are related to their jetting characteristics despite very large differences in strain rate. Tensile testing at very high rates of strain relies on Hopkinson bar techniques in torsion or compression modes (see Blazynski [44]). It is therefore not possible to make comparisons of elongation and necking behaviour at intermediate and very high strain rates.

Up until the UTS - or the experimental UTS if catastrophic failure occurs - deformation is insensitive to the materials failure mode. The high purity aluminium and aluminium alloys are seen to have similar

values of **strain at UTS**. It might be expected that the strain at UTS would be increased in aluminium - magnesium alloys relative to high purity aluminium as a result of the effect of magnesium in solid solution. However, the three high magnesium alloys have retained cold work which has not been removed by annealing. This has reduced their potential for uniform elongation. It is also noticeable that the strain at UTS for copper is very high compared with that found for high purity aluminium, *ie.* 50% compared with 30%. The difference between copper and aluminium here comes about from differences in their dislocation deformation mechanisms. A lower stacking fault energy increases the rate of work hardening in copper together with the associated values of  $\sigma_0$  and  $n$ . These observations indicate that the materials ductility after the initiation of necking is important to break-up in addition to the ductility prior to the UTS.

The strain between UTS and failure is an indicator of failure mode. The change in mode from low to high ductility fracture is clearly exhibited. The precipitate strengthened aluminium - copper - magnesium alloys and the solid solution strengthened aluminium - magnesium alloys show limited ductility. The degree of ductility can be seen to increase through the aluminium alloys to the pure metal. Unlike a laboratory tensile test, jets continue to elongate after the first occurrence of fracture. This process continues until all the fragments are sufficiently small that the stress required to eliminate the velocity gradient between their ends does not result in further fracture of the material. When many necks have been initiated the proportion of unstable deformation may become very important to the total elongation of the jet material. Low ductility fractures will inevitably result in a very small proportion of unstable deformation. However, as the fracture becomes more ductile the proportion of unstable deformation resulting from multiple neck formation will increase.

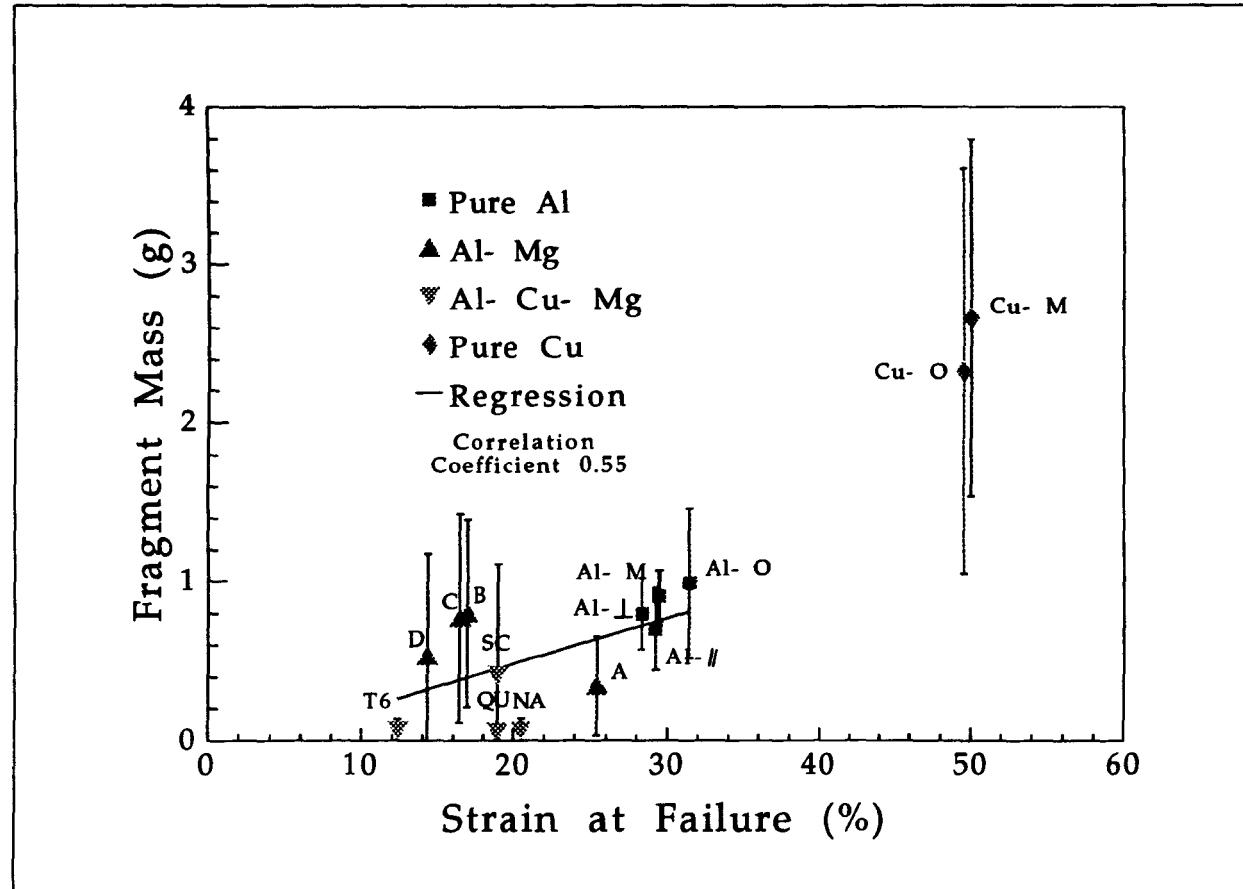


Figure 9.7: Fragment mass versus strain to failure

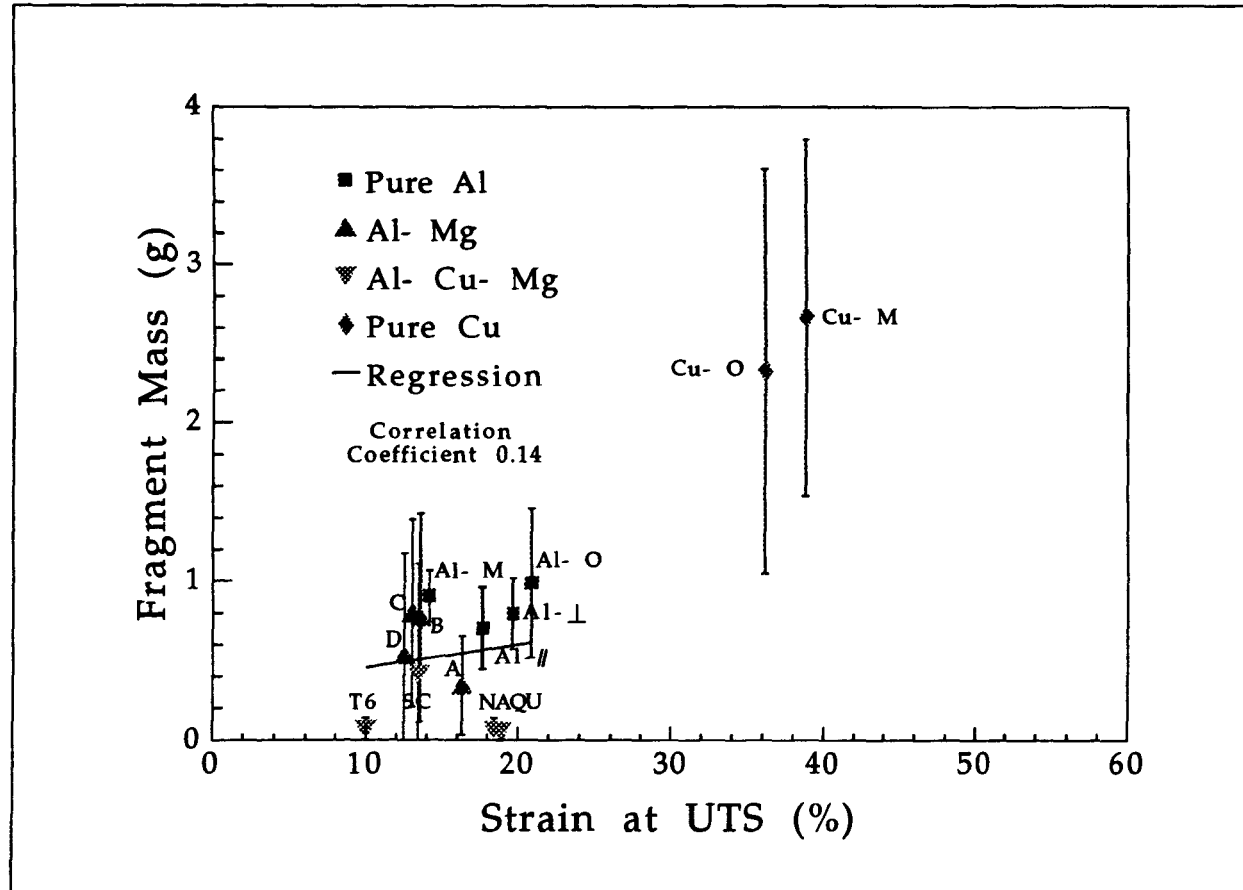


Figure 9.8: Fragment mass versus strain to ultimate tensile stress

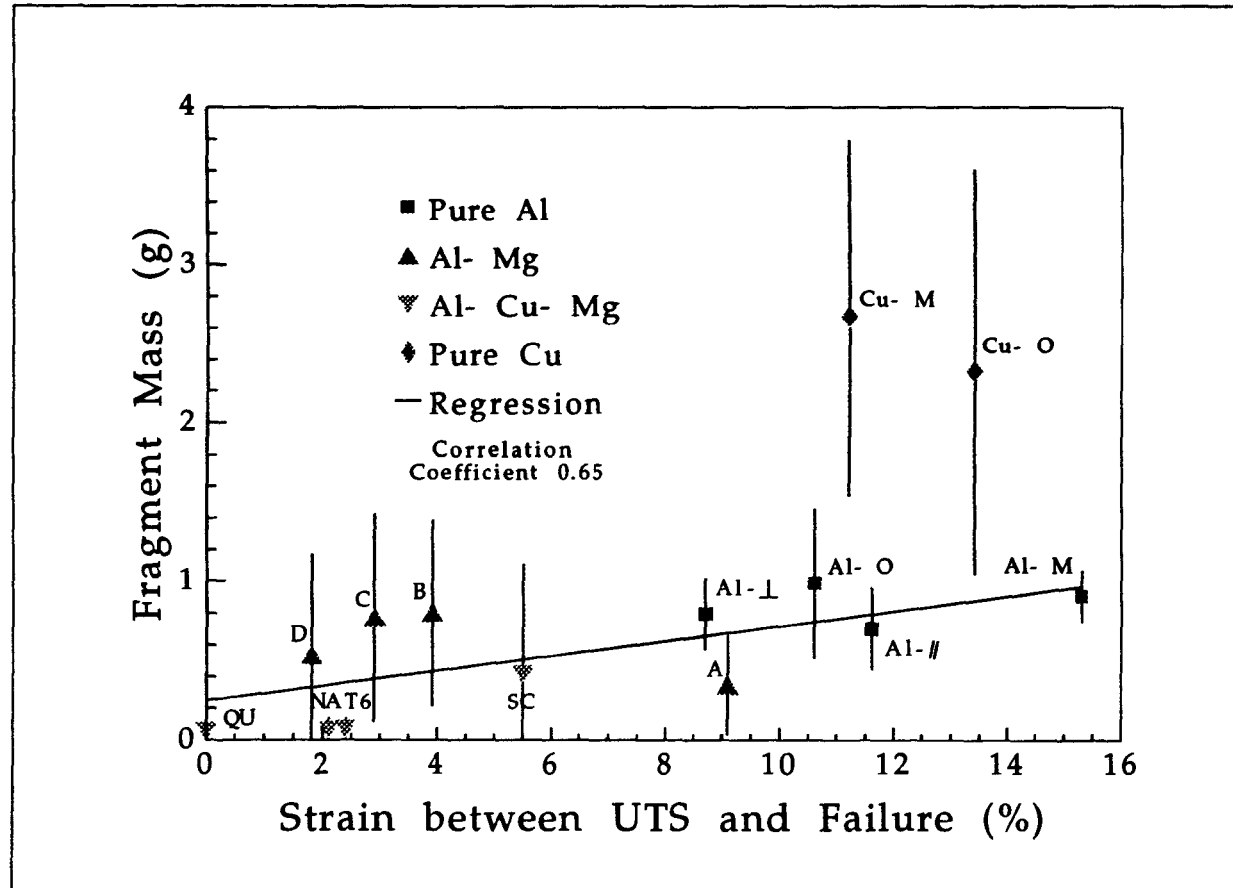


Figure 9.9: Fragment mass versus the difference between the strain to the UTS and the strain to failure

### 9.2.5 Deformation Energy

To investigate the potential relationship between the sum effect of all the tensile mechanical properties which have been deformed at intermediate strain rates under laboratory conditions and the resulting jetting characteristics, the total deformation energy per unit mass was calculated. This term was derived from the materials energy density divided by its physical density (mass per unit volume). Energy density is the energy per unit volume which has been required to deform the material. This is represented by the area under the stress - strain curve. The expression for energy density  $E$ , is usually given as

$$E = \frac{\sigma \epsilon_e}{2} \quad (9.9)$$

This applies only to the area of the elastic region under the stress - strain curve where the relationship is linear. From  $\epsilon_0$  - zero strain at the start of the test to  $\epsilon_e$  the limit of elastic strain.

To calculate the area under the whole curve the following expression is required

$$E = \frac{\sigma \epsilon_e}{2} + \sum_{\epsilon=\epsilon_e}^{\epsilon=\epsilon_f} \sigma \epsilon_p \quad (9.10)$$

This is, the elastic deformation energy plus the plastic deformation energy. The plastic deformation energy is given by the sum of the stress multiplied by the strain in increments from the limit of elastic strain to the materials failure,  $\epsilon_f$ . As the proportion of elastic to plastic deformation energy is very small this approximates to

$$E = \sum_{\epsilon=\epsilon_0}^{\epsilon=\epsilon_f} \sigma \epsilon \quad (9.11)$$

Dividing by the materials physical density gives the energy per unit mass. The reason for using a mass related term over a volume term has previously been discussed.

Deformation energy per unit mass values are plotted versus fragment mass in Figure 9.10. This analysis indicates a general trend for the fragment mass to decrease as the deformation energy per unit mass increases. Once again the aluminium - copper - magnesium alloys and in particular

those in the naturally aged and T6511 conditions were seen to be insensitive. The observed relationship shows that the absorption of energy by the jet material is related to its break-up characteristics. The deformation energy parameter is determined by the values of stress and strain. These determine the break-up characteristics through various complex relationships some of which have been discussed previously. Neither the deformation energy per unit length of fragment nor the deformation energy per fragment result in a constant value for the materials tested.

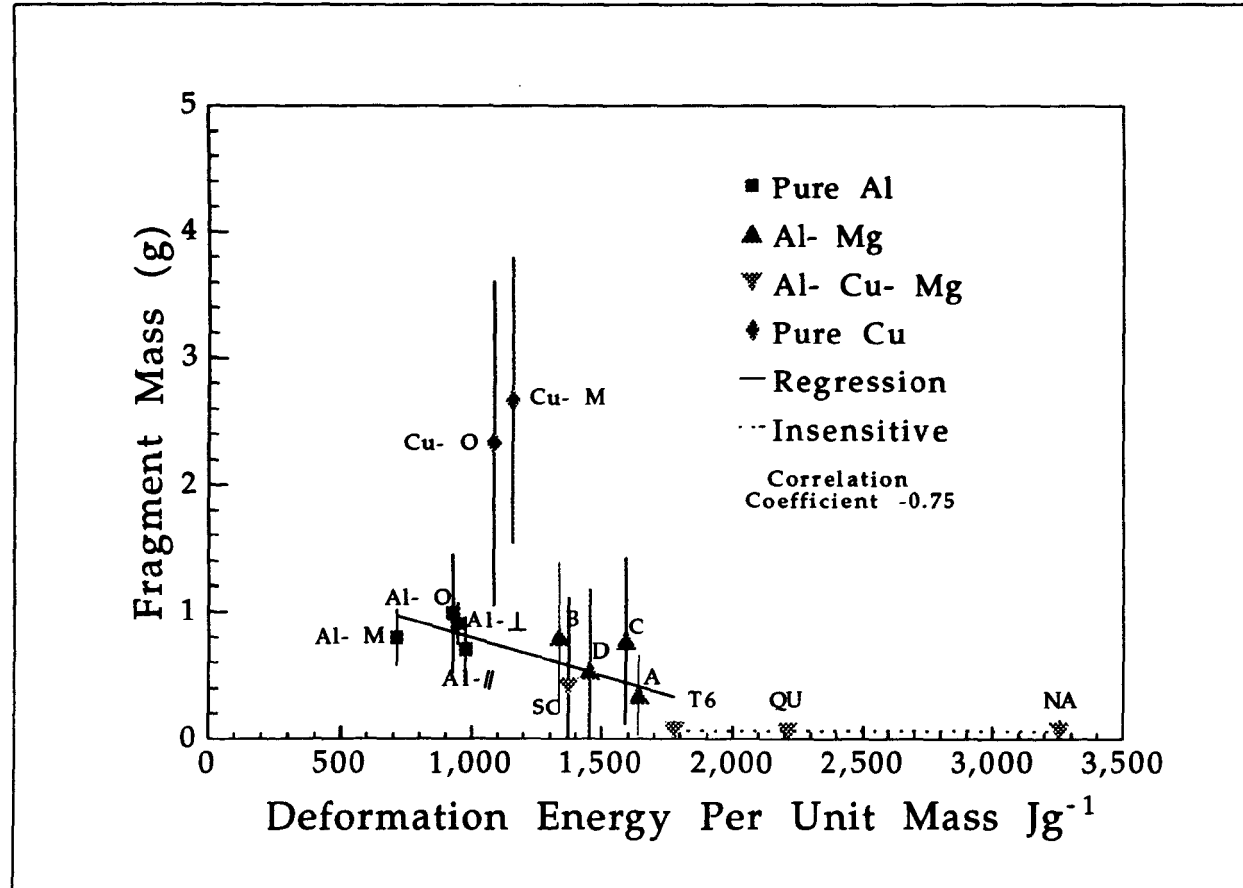


Figure 9.10: Fragment mass versus deformation energy per unity mass

## 9.3 Break-Up Mechanisms

When loaded by an explosive shock wave a shaped charge liner may experience stresses in the region of  $10^4$  MPa. Compared to the value for the yield strength of most metals, which is of the order  $10^2$  MPa, this force is so great that the metal has in some instances been considered to have insignificant strength. Under these conditions it has been suggested that the microstructural properties of the liner would not have a significant effect on the jets. In this project it has been shown that these metallurgical features of shaped charge liners may have a profound effect.

In order to understand the relationship between mechanical properties and jet behaviour it is necessary to consider the mechanisms by which such properties could act upon the jet. This means that the mechanism of deformation and break-up under jetting conditions needs to be examined. In the literature survey the basic principals of all currently established deformation mechanisms in metals have been discussed, Section 2.3. Of these only deformation by dislocation based mechanisms and twinning appear to offer a reasonable basis for understanding and when large strains are required dislocation based mechanisms may offer the only solution.

This does not imply that other deformation mechanisms do not operate but that they are much less significant in terms of their contribution to the total strain. Twinning for example was found to be prevalent in shock loaded materials, see Section 6.2.4. However, the total resultant strain due to twinning is limited. Diffusion based mechanisms in traditional large grained metals are not considered as their diffusion rates are usually too low to produce any significant strain in the time scale of the jetting process.

### 9.3.1 Validation of Deformation by Dislocation Motion at Very High Rates of Strain

To deform a crystalline material without causing long range disruption of the lattice structure requires that adjacent planes of atoms are sheared passed one another. To shear an entire lattice plane would require a very high stress. Dislocation theory describes a mechanism for

high strain deformation at low stresses by incremental shearing. The increment of shear produced by one dislocation is the Burgers vector, this has a similar magnitude to the separation of atoms in the lattice plane: this is of the order  $3 \times 10^{-10}m$ , 0.3 nm.

The limiting velocity of a dislocation through a crystal lattice is the velocity of sound through that material. At velocities approaching the sonic velocity, dislocations suffer relativistic effects. To move a dislocation at this speed would require an infinite driving force. The sonic velocity in most metals is very similar at approximately  $5000ms^{-1}$ .

The dislocation density of a material is measured in terms of the number of dislocations intersecting a plane of unit area. A typical density for a heavily cold worked metal would be of the order  $10^{16}m^{-2}$ . This figure represents the total dislocation density, only the proportion of these that are free to move can contribute to the deformation.

The rate at which a material is deformed, the strain rate  $\dot{\epsilon}$ , can be defined as the increment of deformation, Burgers vector  $\underline{b}$ , times the mobile dislocation density  $\rho$ , times the average dislocation velocity,  $\bar{V}$ .

$$\dot{\epsilon} = \underline{b}\rho\bar{V} \quad (9.12)$$

Given that the highest estimate of strain rate in the deformation of a collapsing shaped charge liner is of the order  $10^7s^{-1}$  and that under these conditions the dislocations may be assumed to be travelling fast enough to approximate to the sonic velocity in metals, then the required dislocation density for this very severe deformation can be estimated. Substituting the following values into a rearranged version of Equation 9.12 yields the required mobile dislocation density;  $\dot{\epsilon} = 10^7s^{-1}$ ,  $\bar{V} \simeq 5000ms^{-1}$ ,  $\underline{b} = 3 \times 10^{-10}m$

$$\begin{aligned} \rho &= \frac{\dot{\epsilon}}{\underline{b}\bar{V}} \\ &\simeq 6.7 \times 10^{12}m^{-2} \end{aligned}$$

This analysis predicts a mobile dislocation density about an order of magnitude greater than a typical total dislocation density.

To test the plausibility of this model it is necessary to consider how closely packed dislocations would be at this density and the theoretical limit to their packing. To force two dislocations with repelling stress fields into close proximity would require very large amounts of energy. However, the intensity of a dislocation stress field decays very rapidly with distance and therefore the effect of proximity should not become significant until the dislocations are within a few Burgers vectors of each other.

At the calculated density the mean spacing between dislocations would be 390 nm,

$$\frac{1}{\sqrt{\rho}} \simeq 3.9 \times 10^{-7} m$$

With a mean dislocation spacing approximately three orders of magnitude greater than the Burgers vector it is reasonable to assume that this dislocation density could be achieved.

Using the previous argument in reverse, if it may be assumed that a mean dislocation separation of 40 times the Burgers vector is not unreasonable, then a dislocation density as high as  $10^{16} m^{-2}$  could exist. This figure is an arbitrary value used as an illustration, its actual value is not important. Rearranging Equation 9.12 (values for strain rate,  $\dot{\epsilon}$ , and Burgers vector,  $\underline{b}$  remain the same) yields an average dislocation velocity of approximately  $5ms^{-1}$ .

The numerical values used in the two previous cases are for the most extreme conditions. Strain rates of  $10^7 s^{-1}$  are only likely to be transitory and will very rapidly decrease. Almost immediately after break-up the jet fragments cease to elongate, therefore their strain rate has reached zero after only  $\sim 100\mu s$ . Thus the calculated values for mobile dislocation density need only represent the maximum value required for dislocation deformation mechanisms to be considered acceptable at very high strain rates.

Possible evidence of rapid recrystallisation has been found in material recovered from shaped charge jets, see Chapter 5. This is the type of response that would be expected if a large mobile dislocation density were to have existed. It is postulated that there might have been sufficient driving force provided in these circumstances for recrystallisation to occur without thermal activation. Rapid dynamic recrystallisation would result

in a material with a fine equiaxed grain structure. Subsequent annealing of the material which might cause grain growth may have been prevented by the quenching effect of the fragment capture medium.

It is therefore suggested that the deformation and break-up of shaped charge jets - at least for pure, face centre cubic metals - is by "ordinary" dislocation mechanisms. The very high strain and strain rates involved being accommodated by a high mobile dislocation density and high dislocation velocities.

### 9.3.2 A Hypothesis for Shaped Charge Jet Break-Up

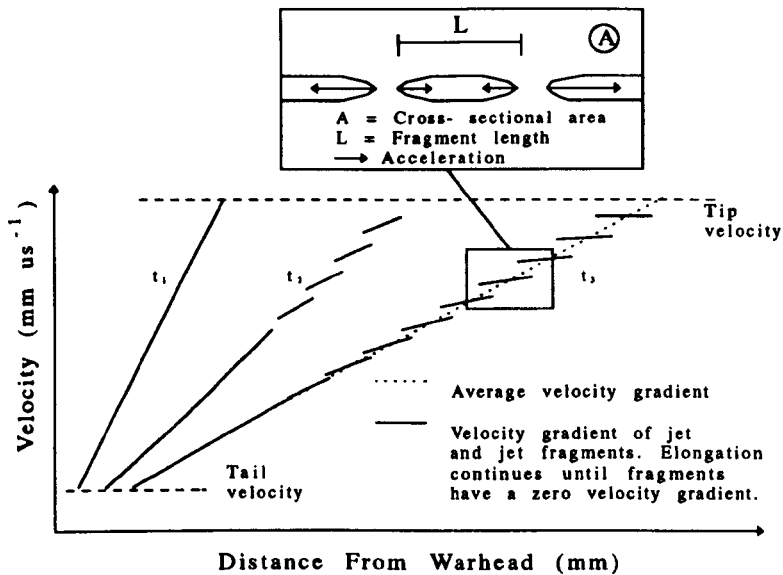
A typical elongating jet has a tip velocity of  $5000\text{ms}^{-1}$  and a typical tail velocity of  $2000\text{ms}^{-1}$  - see Figure 7.4. The  $3000\text{ms}^{-1}$  velocity difference along the length of the jet is, to a reasonable approximation, distributed in a linear velocity gradient. Neglecting air resistance - similar results are obtained in a vacuum - the jet is an independent system; no external forces act upon it.

After a short time in free flight (typically  $\sim 100 \times 10^{-6}$  seconds for a pure metal) the elongating jet is seen to break-up into fragments. Once a fragment has broken away from the main part of the jet no further elongation is observed. Therefore, the tail of the fragment must have been accelerated and the tip of the fragment decelerated until the velocity of the fragment is equal to its mean velocity while still elongating. Acceleration of the tip (or deceleration of the tail) of a fragment requires that a force acts on that material. As no external forces are able to act upon the jet the force must be internal, *ie.* resistance to deformation. The acceleration and deceleration of elongating jet material can be considered using the Newtonian equation

$$F = ma \quad (9.13)$$

Note that the acceleration and deceleration is localised and results in the formation of discrete fragments. The average velocity profile of the whole jet is unaffected. Figure 9.11 schematically represents these conditions.

A jet is considered with constant cross sectional area,  $A$  and with a



The velocity gradient of a hypothetical jet is shown at three times;  $t_1$  shows a jet at an early time prior to break-up,  $t_2$  shows the initiation of break-up and  $t_3$  shows break-up at an advanced stage. Break-up is shown to occur sequentially from the jet tip towards the tail. This is anticipated under "ideal" conditions. The insert indicates the effect of acceleration acting on jet fragments. This causes the velocity gradient of individual fragments to be reduced to zero.

Figure 9.11: Schematic diagram of the effect of break-up on the jets velocity gradient

density,  $\rho$ . The length of the fragments into which the jet will break is  $L$ , this represents the maximum length of jet which can support the forces acting on it without fracturing. The force,  $F$ , is that which acts at the fracture site prior to the break-up of each jet fragment.

$$\begin{aligned} F &= \sigma A \\ m &= \rho LA \\ a &= \frac{dV}{dt} \end{aligned}$$

Substituting these expressions into Equation 9.13 yields the following

$$L = \left[ \frac{\sigma}{\rho \left( \frac{dV}{dt} \right)} \right] \quad (9.14)$$

Equation 9.14 can be considered in two parts. Firstly, the fragment length is inversely proportional to the density of the material. This effect was postulated in Section 7.5.2. It indicates that for materials of different density but similar mechanical properties the mass of the fragments should be equal. Therefore the volume of fragments from such materials is different by a factor which is dependent on the materials density.

Equation 9.14 also shows the fragment length to be proportional to the strength of the material and inversely proportional to the acceleration acting on the material as a result of resistance to deformation. The  $\sigma$  and  $\frac{dV}{dt}$  terms represent the balance between the materials strength required to support deformation without fracture and the resistance to deformation which changes the velocity gradient of the jet. As the maximum value of  $L$  is usually required, then it would appear that the maximum value of  $\sigma$  should also be required. This suggests that materials with high strengths would result in long jet fragments. However, the acceleration term in Equation 9.14 is determined by the materials resistance to deformation, *ie.* the flow stress. This is dependent upon the materials strength and its ability to work harden. Increasing the  $\sigma$  term simultaneously increases the  $\frac{dV}{dt}$  term. The net result is a decrease in  $L$  as  $\sigma$  increases.

The effect of work hardening stabilises uniform deformation. As was seen in Figure 9.8 the uniform elongation of pure aluminium and the aluminium alloys was of a similar magnitude. However, only the pure

aluminium was able to maintain its high strength for large strains after the initiation of necking. The strength of the aluminium alloys was of a much higher magnitude at the initiation of necking but this could not be sustained due to phenomena which initiate early fracture. These phenomena include the formation of voids which cause exaggerated geometric softening by reducing the load bearing cross sectional area or more particularly cracks which may result in catastrophic failure due to the formation of adiabatic shear bands.

**Jets of the ductile metals aluminium and copper are able to undergo considerable elongation prior to break-up.** The primary deformation mechanism is through dislocation glide and the strain rates are achieved by a very high mobile dislocation density. The strength of the material and its resistance to deformation is initially low and the material is able to plastically deform. Work hardening will increase the strength and hence the resistance to deformation of the material. When the work hardening is no longer able to maintain uniform deformation, necking is initiated and the material will subsequently undergo ductile fracture provided other fracture mechanisms do not intercede.

**Jets of the aluminium alloys are not seen to elongate greatly prior to break-up.** The primary deformation mechanism is still likely to be dislocation glide and the mobile dislocation density is likely to be very high. However, these materials contain large numbers of precipitates which act as a strengthening mechanism by blocking the glide of dislocations. Under quasi-static conditions there are several mechanisms by which the dislocations can move, for example by cutting through the precipitate or looping around them - see Section 2.3.2. At high strain rates, though, these may be unable to operate, the result would be large dislocation concentrations around the precipitates. A large concentration of precipitates is likely to initiate a brittle fracture and therefore lead to premature jet break-up.

## CHAPTER 10

# Conclusions and Recommendations for Further Work

This section presents the conclusions drawn from the observations made and discussed in the previous two chapters. There are two parts: Firstly, to assess the validity of treating the jet as a solid it has been necessary to confirm that the material is indeed solid. Once this was established the viability of the proposed mechanisms for deformation could be considered. Secondly, relationships between the measured mechanical properties of liner materials and the observed break-up characteristics of their resultant jets are described.

Using the knowledge gained through the investigations described in this thesis, some recommendations for further work are made.

### 10.1 Shaped Charge Jets in the Solid State

The mechanisms of deformation and break-up of the shaped charge jets proposed in this thesis are dependent upon the movement of dislocations through a solid crystalline material. The "solid jet" can be justified by several observations.

Firstly, X-ray diffractions of jets while in flight have indicated the existence of a crystalline structure in the jet material. Although the available data is very limited, this is conclusive proof that at least a proportion of the jet is comprised of a crystalline solid.

Metallurgical characteristics of the liner material could only effect the break-up of jets which remain in the solid state. History effects of the

liners microstructure cannot be transmitted via a liquid phase and subtle changes in microstructure have been shown to have a dramatic effect on the jets break-up.

The break-up mechanism is characteristic of solid materials. Fracture has been seen to occur by failure with varying degrees of ductility. The fracture of jets is seen to be similar to the fracture of its liner material tested under laboratory conditions.

Finally, it has been shown quantitatively that dislocation deformation mechanisms are viable even at the highest strain rates encountered in the jetting process.

## 10.2 Jet Break-Up in Relation to the Quasi-Static Properties of Liner Materials

All the relationships investigated are for the mass of fragments resulting from aluminium and aluminium alloy jets versus the materials mechanical properties. It has been postulated that the results for copper or other materials may be described by similar relationships. If this were the case fragment volume could be used as the parameter for jetting characteristics. It is anticipated that by using fragment volume a single relationship to particular mechanical properties would be found. This hypothesis cannot at present be tested because there is insufficient data available for materials other than aluminium.

The ultimate elongation of a shaped charge jet is determined by two parameters: its ductility and its propensity towards low ductility fractures which result in the premature cessation of ductile deformation. It has been found that the high strain rate deformation and break-up of shaped charge jets can be related to the quasi-static tensile properties of their liner material. However, the quasi-static test conditions need to be in a strain rate range such that the proportion of deformation due to diffusion mechanisms is insignificant. At excessively low strain rates some materials may exhibit superplastic properties which are dependent upon diffusion and therefore are unrepresentative of jetting conditions.

The deformation energy per unit mass is believed to be an accurate indicator of a materials jetting characteristics. As the deformation en-

ergy per unit mass increases the resulting jet fragment mass decreases. This embodies the concept that materials which generate the greatest resistance to deformation will result in the least amount of jet elongation. However, this parameter describes the compound effect of many other materials properties. In order that the deformation and break-up of jets is best understood it is necessary to consider the effect of specific materials properties on jetting characteristics.

The materials ductility is mainly dependent on mechanical properties which can be measured during the initial, uniform stage of deformation. Of these measurable properties, the work hardening characteristics are most critical in determining the materials ductility. Large ductilities result from materials which have low rates of work hardening. The lowest rates of work hardening and hence the highest ductilities occur in high purity metals which have low stacking fault energies.

It appears that the difference between the measured coefficient of work hardening and the measured strain at the UTS may be useful in predicting the materials failure mode. Materials with a high propensity towards low ductility fracture are unlikely to exhibit large strains between their UTS and failure. Such behaviour can be anticipated if the measured strain at UTS is significantly less than the measured coefficient of work hardening. Conversely, ductile fracture and therefore large necking strains can be anticipated, though not guaranteed, if these values are similar.

The energy of a jet is sufficient to overcome any resistance to deformation resulting from its own elongation. However, the jet material is not able to support unlimited stress and will at some point fail through some mode of fracture. Therefore it is not high values of UTS which result in early jet break-up but that the rate of work hardening required to reach the high UTS results in low strains to failure. This effect is exaggerated by the tendency for strengthening mechanisms which result in high rates of work hardening to cause local stress concentrations which cause low ductility fractures. Therefore, the UTS value can be used as a reasonably accurate indicator to a materials potential jetting characteristics. It cannot, however, be used to anticipate differences in work hardening characteristics or in the materials failure mode. Low ductility failures in particular could dramatically reduce the potential for jet elongation

regardless of the UTS value.

The correlation between proof stress and jetting characteristics is that increasing proof stress is associated with decreasing fragment mass. Proof stress is an approximation to the stress at which plastic deformation occurs in preference to elastic deformation. However, the proof stress is also indicative of a materials strain history. If a proportion of the materials total plastic elongation has been used by cold work, this is indicated by an increase in the proof stress. This effect though, is strongest in those materials which have high rates of work hardening and as a result are unlikely to produce jets which elongate greatly.

## **10.3 Recommendations for Further Work**

### **10.3.1 Additional Materials**

The work conducted for this thesis concentrated mainly on aluminium and aluminium alloys. The first aim of further work should therefore be to establish whether or not other materials can be described by the same relationships. There is no reason to suspect that this should not be the case for all plastically deformable materials. It is suggested that if materials of different densities are examined, the criteria for assessment of break-up is made using fragment volume rather than fragment mass. This will normalise the results with respect to the materials density. It is anticipated that materials of any density will then fit a single relationship for jetting characteristics versus mechanical properties. It would be beneficial if the initial further work was as far as possible comparable with existing results. The obvious candidate material is copper. In common with aluminium, copper is a face centre cubic ductile metal which is easily alloyed. Pure copper and a copper - zinc alloy (brass) are suggested as suitable candidates for such an analysis.

Expanding the investigation to cover a wider range of materials requires a structured approach. Two areas which require further investigation have been identified. Firstly, further detailed investigation into the effects of materials properties would require carefully selected materials. These would require careful metallurgical characterisation and control of their properties. It would be anticipated that pure or low alloy, face centre cubic metals would be most suited to this purpose. Copper and

copper - zinc alloys as described previously are the materials suggested for this type of investigation.

Secondly, the scope of the investigation could be widened to include other metals with different crystal structures. Body centre cubic (*eg.* iron or tantalum) and hexagonal close packed (*eg.* zinc) crystal structures have different deformation characteristics to face centre cubic metals. A limited number of experiments using these materials would be useful as they may reveal more information about the deformation mechanisms. It is not anticipated that these would be advantageous to jetting performance as their work hardening rates can be very high. Of particular interest would be the effect of the yield stress in body centre cubic metals - which can be significantly higher than the flow stress. It would be interesting to investigate the effect of orientation in hexagonal close packed materials because of their highly anisotropic nature. The large difference in rate of work hardening when tested in parallel to and perpendicular to the basal plane suggests two experiments. However, the complex flow path required for shaped charge jet formation may make interpretation of the results difficult.

### **10.3.2 Experimental Technique**

The greatest difficulty in these investigations has been to characterise the fractured jets. The established method of estimating fragment volume and hence mass from measurement of their length and breadth is susceptible to large errors. It would be anticipated that with the available imaging techniques it will be impossible to make accurate measurements of fragment volume. However, with the aid of more sophisticated image analysis and with the addition of image enhancement, it may be possible to reduce the magnitude of error. The most effective method employed for improving the image quality and therefore improving the accuracy of image analysis was to generate images with the highest possible contrast.

## APPENDIX A

# Design of the Warhead Assembly

The unfilled warheads were assembled as follows: The boat tail case, Figure A.1 was machined as a single component from aluminium alloy bar. A copper liner dummy, Figure A.2, was inserted and held in place by a locking ring, Figure A.3.

These assemblies were then sent to RARDE (Royal Armament Research and Development Establishment) for explosive filling. The EDC1S explosive was cast into the cases. After filling the liner dummy was removed, the resulting cavity could then accept a finished liner and the locking ring be reused to secure the assembly.

The detonation train consisted of an RP 80 high voltage detonator and a DEBRIX booster pellet which were centrally mounted on the rear of the boat tailed case. The detonator holder assembly contained an access point for a probe to be placed between the detonator and the booster pellet.

Complete assembly of the warheads was carried out immediately prior to firing. An assembled warhead, showing a non specific liner, is shown in Figure A.6.

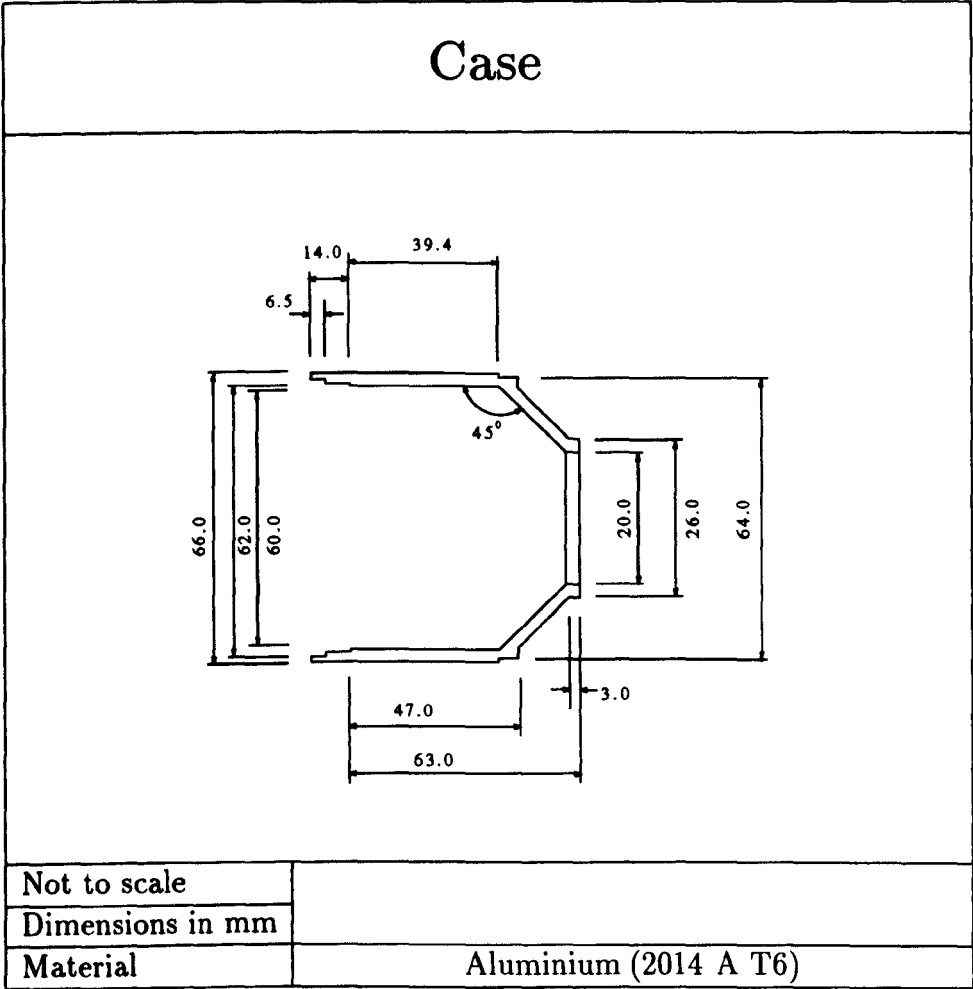


Figure A.1: Case for explosive warhead

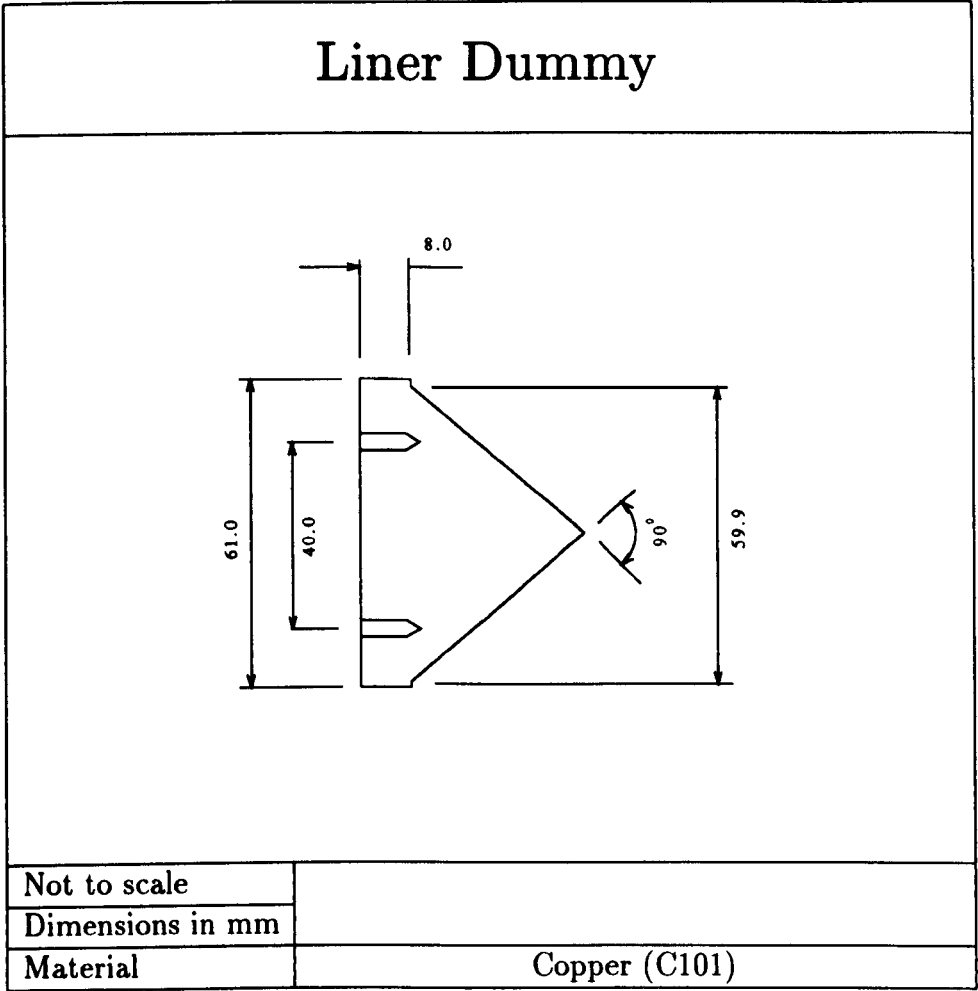
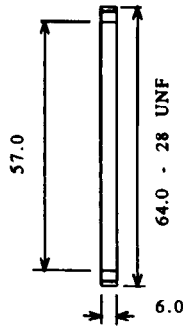


Figure A.2: Liner dummy, for casting of explosives

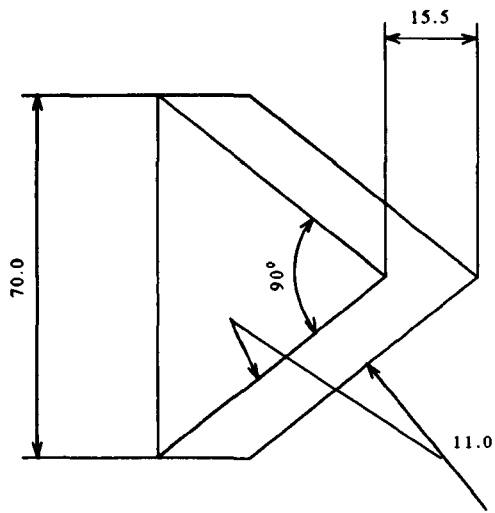
# Locking Ring



Not to scale	
Dimensions in mm	
Material	Aluminium (HE 30 TF)

Figure A.3: Locking ring for aluminium liners

# Liner Blank



Not to scale	
Dimensions in mm	
Material	as supplied

Figure A.4: Liner blank used for heat treating aluminium alloys.

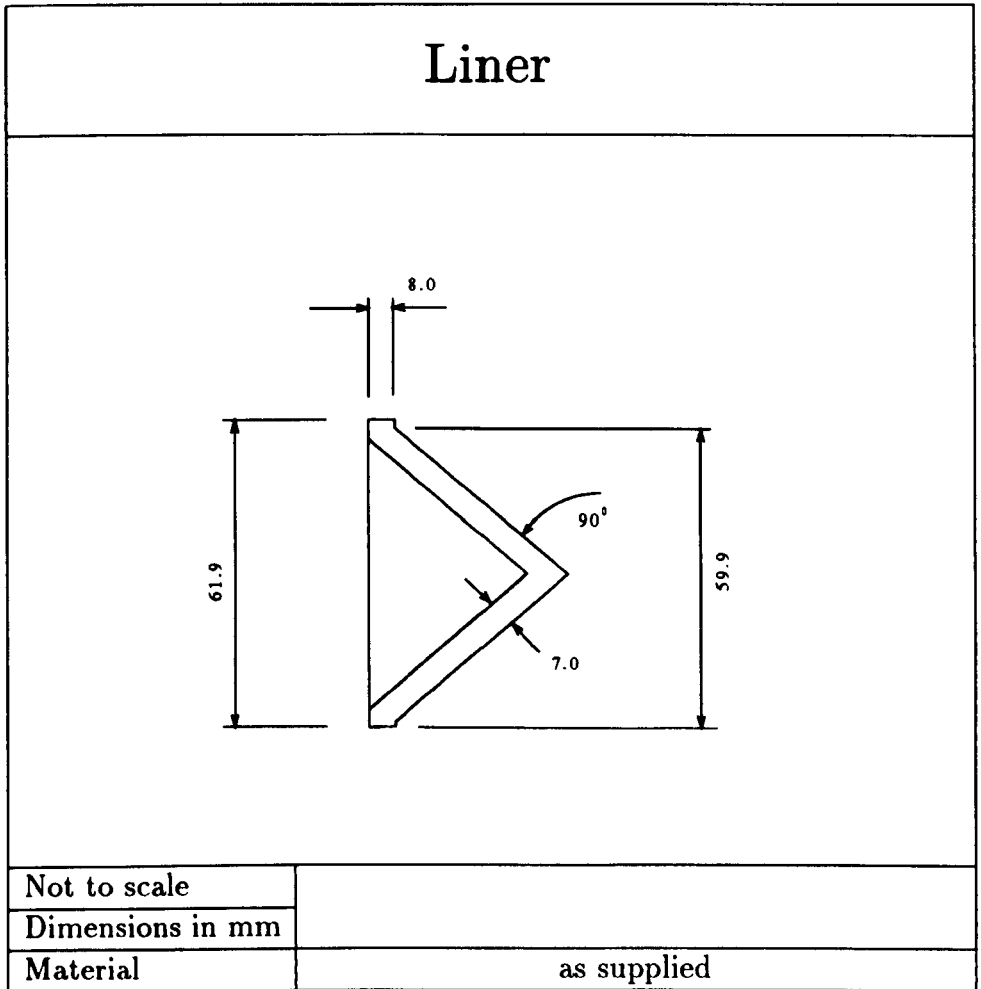
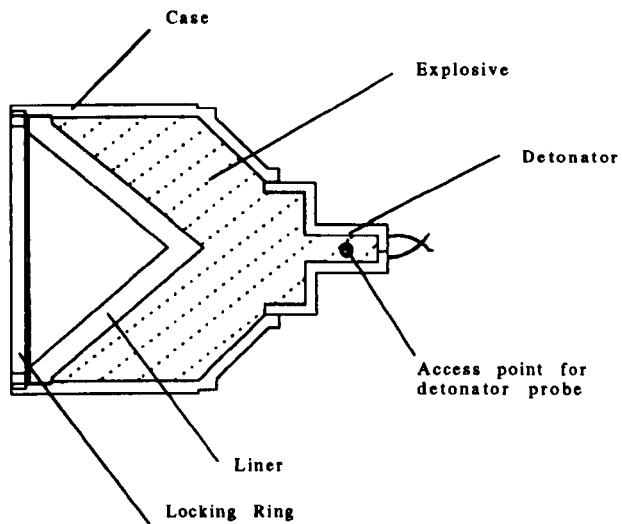


Figure A.5: Liner, final machined and heat treated form

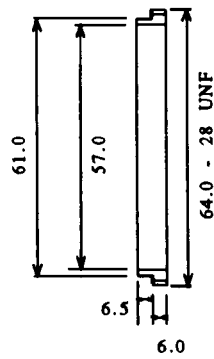
## Firing Condition



Not to scale

Figure A.6: Firing condition, the assembled warhead ready for firing.

# Modified Locking Ring



Not to scale	
Dimensions in mm	
Material	Aluminium (HE 30 TF)

Figure A.7: Modified locking ring for copper liners

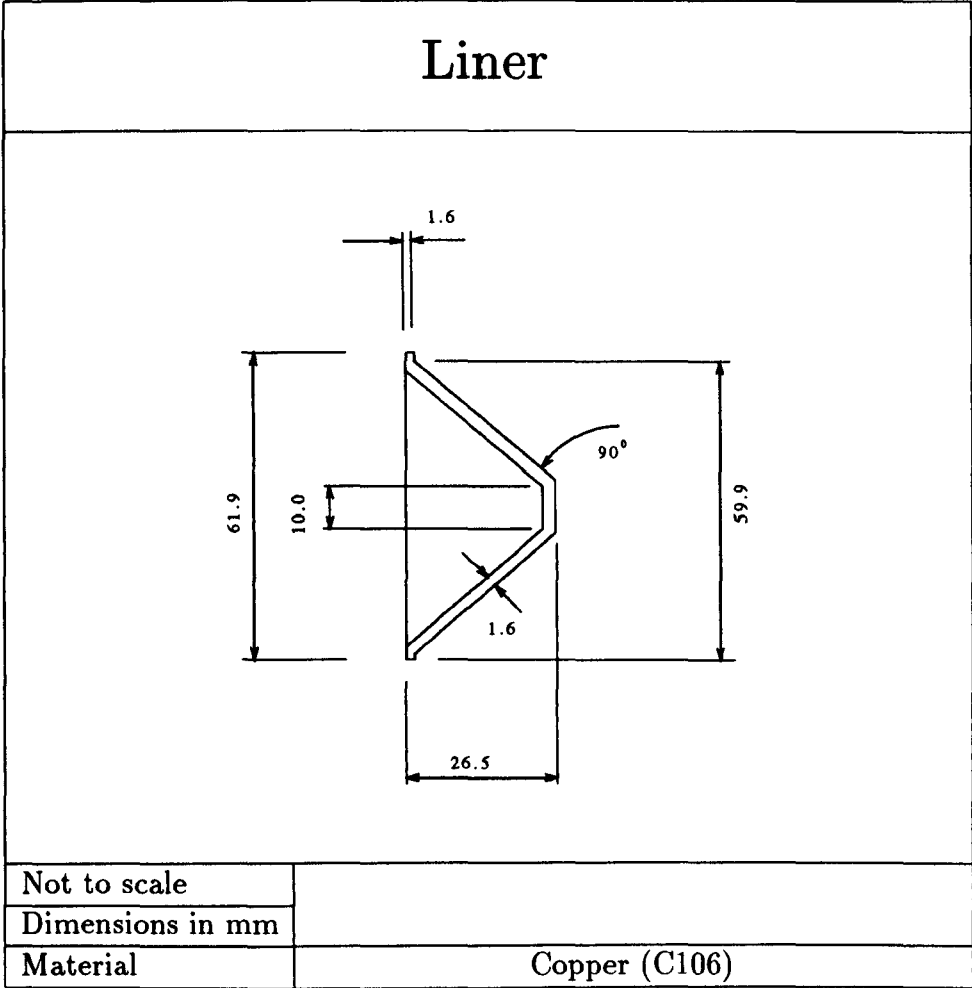


Figure A.8: Copper liner, final machined and heat treated form

## APPENDIX B

# Laboratory Testing of Liner Material

### B.1 Tensile Testing

#### B.1.1 Specimen Dimensions

For aluminium and aluminium alloys, specimens with a circular cross section were used. These had a gauge length of  $37.0\text{mm}$  and were  $5.7\text{mm}$  in diameter. The copper specimens were punched from flat sheet in the “dog bone” configuration. The specimens had a gauge length of  $20.0\text{mm}$  and their rectangular cross section had dimensions  $5.0 \times 2.1\text{ mm}$ .

#### B.1.2 Commercially Pure Aluminium

From the stock of material used for firing reference numbers 527/5 and 527/6, tensile specimens were made with their axes parallel to the extrusion direction. From the stock of material used for firing reference numbers 570/6 and 570/7, three batches of tensile specimens were made. One batch of specimens was manufactured with their axes parallel to the extrusion direction. The other two batches were made with their axes perpendicular to the extrusion direction: they were also perpendicular to each other.

#### B.1.3 Aluminium Alloys

All tensile specimens were made with their axes parallel to the extrusion direction.

### **B.1.4 Commercially Pure Copper**

A test liner was manufactured from the annealed 3 mm thick C106 sheet. This was sectioned and hardness tested: it was found to have a hardness value of 96 (Vickers hardness at 5 Kg load). This material was fully annealed at  $505 \pm 5^\circ\text{C}$  for 3 hours, then hardness tested: it was found to have a hardness value of 51 (Vickers hardness at 5 Kg load). An annealing process was then developed which would produce a half hard condition. It was found that annealing at  $400 \pm 5^\circ\text{C}$  for 3 hours would produce a material with a hardness of 74 (Vickers hardness at 5 Kg load).

From the annealed 3 mm thick C106 sheet, two strips were cut and rolled to 2.3 mm thickness: this was the thickness of the material in the test liner used for hardness testing. One strip was annealed to the half hard condition, 74 Vickers hardness at 5 Kg load by heating at  $400 \pm 5^\circ\text{C}$  for three hours. From each of these strips of material tensile specimens were manufactured.

### **B.1.5 Data Collection and Analysis**

Tensile testing was carried out using a Lloyd Instruments M30K tensile testing machine. An internal extensometer recorded cross-head displacement. The analogue output from this device was recorded by Lloyd Instruments "DAPMAT" software. This software performed some data analysis for the basic tensile properties *ie.* the UTS, the strain at the UTS, the strain at failure. For further analysis, such as derivation of the work hardening coefficient, the data was exported into spreadsheet software and manipulated appropriately.

## **B.2 Metallography**

Three specimens were made from each material. The face of one specimen was normal to the extrusion direction while the other two were perpendicular to the extrusion direction and to each other. These were ground and polished to less than  $1\mu\text{m}$  grit and then electrolytically etched.

Pure aluminium was etched in 0.5%  $\text{HF}_{(aq)}$ , aqueous hydro - fluoric

acid, by immersion for approximately 120 seconds. The etchant solution for aluminium alloys was 2%  $\text{HBF}_4(\text{aq})$ , aqueous hydro - boro - fluoric acid. Anodic electrical contact was made with the specimens through a hole drilled and tapped into the back of their mounts. The cathode was an annulus of 1050 pure aluminium sheet, covered by the electrolyte. The specimens were placed in the electrolyte at the centre of the cathodic annulus and 25 to 30 volts applied for 60 to 180 seconds. Pure copper was etched using acidic ferric chloride - 125g  $\text{FeCl}_3$ , 50 ml HCL, 2.5 litres methanol - or acidic potassium dichromate - 2g  $\text{K}_2\text{Cr}_2\text{O}_7$ , 8 ml  $\text{H}_2\text{SO}_4$ , 1 ml HCL, 200 ml  $\text{H}_2\text{O}$ .

### **B.2.1 Grainsize Analysis**

Grain size analysis was carried out by the linear intercept method; the number of grain boundaries which intercept a line of known length are counted. By dividing the number of intercepts by the length of the line, the grain size is found - for the direction of the line over which the measurements were made.

# Acknowledgments

It is with regret that only written thanks can be expressed to the late Professor JSL Leach who as supervisor and as head of the Department of Metallurgy made an enormous contribution towards this work.

The author wishes to thank John Nicholson of the Warheads and Terminal Effects Department, Hunting Engineering Limited for initiating and supporting this project. Special thank are extended to Mike Rogers for the supervision and guidance he has given. Many other Hunting's staff have contributed their help and advice but John Easton and all those based at Porton Down require special mention.

Thanks are extended to Professor J Wood, head of the Department of Materials Engineering and Materials Design, for the provision of laboratory facilities. Thanks also go to Professor S Harris who has taken on the supervision of this project and made many valuable contributions. The author is especially grateful for the efforts and patience of Doctor Bob Moon.

Special thanks are extended to the technical and workshop staff at Nottingham for their fast and very efficient help.

Finally, special thanks and lots of love to Mum, Dad and Karen.

## References

- [1] C.E. Munroe. Modern Explosives. *Schribners Magazine*, **3** : pp 563–576, 1888.
- [2] M.A Cook. *The Science of High Explosives*. Krieger Publishing Co., 1985.
- [3] P.C. Chou and W.J. Flis. Recent Developments in Shaped Charge Technology. *Propellants, Explosives and Pyrotechnics*, **11** : pp 99–114, 1986.
- [4] W.P. Walters and J.A. Zukas. *Fundamentals of Shaped Charges*. Wiley-Interscience, 1989.
- [5] R.W. Wood. Optical and Physical Effects of High Explosives. *Proceedings of the Royal Society (London)*, **157A** : pp 249–261, 1936.
- [6] G.I. Taylor. Analysis of the Explosion of a Long Cylindrical Bomb Detonated at One End. In *The Scientific Papers of Sir G.I. Taylor*, volume **3**, pages 277–286. Cambridge University Press, 1963.
- [7] R.W. Gurney. The Initial Velocities of Fragments from Bombs, Shells and Grenades. Technical report, Ballistics Research Laboratory, 1943. Report 405.
- [8] G. Birkhoff, D.P. MacDougall, E.M. Pugh, and G.I. Taylor. Explosives with Lined Cavities. *Journal of Applied Physics*, **19** : pp 563–582, 1948.
- [9] E.M. Pugh, R.J. Eichelberger, and N. Rostoker. Theory of Jet Formation by Charges with Lined Conical Cavities. *Journal of Applied Physics*, **23** : pp 532–536, 1952.

- [10] J.E. Kennedy. Gurney Equation of Explosives: Estimation of the Velocity and Impulse Imparted to Driven Metal. Technical Report SC-RR-70-790, Scandia Laboratories, Albuquerque, New-Mexico, 1970.
- [11] P.Y. Chantéret. An Analytical Model for Metal Acceleration by Grazing Detonation. In *Proceedings 1<sup>st</sup> International Symposium on Ballistics*, 1983.
- [12] R.J. Eichelberger. Re-examination of the Non-steady Theory of Jet Formation by Lined Cavity Charges. *Journal of Applied Physics*, **26** : pp 398–402, 1955.
- [13] P.C. Chou, J. Carleone, W.S. Flis, R.D. Ciccarelli, and E. Hirsch. Improved Formulae for Velocity, Acceleration and Projection Angle of Explosively Driven Liners. *Propellants, Explosives and Pyrotechnics*, **8** : pp 175–183, 1983.
- [14] J.M. Walsh, R.G. Shreffler, and F.J. Willig. Limiting Conditions for Jet Formation in High Velocity Collisions. *Journal of Applied Physics*, **24** : pp 349–359, 1953.
- [15] J. Carleone and P.C. Chou. A One Dimensional Theory to Predict the Strain and Radius of Shaped Charge Jets. In *Proceedings 1<sup>st</sup> International Symposium on Ballistics*, pages 1–27, November 1983.
- [16] A. Lichtenberger, M. Scharf, and A Bohmann. Influence of the Structural and Metallurgical State of a Liner on the Performance of a Shaped Charge. In *Proceedings 6<sup>th</sup> International Symposium on Ballistics*, pages 213–219, 1981.
- [17] F. Jamet. Investigation of Shaped Charge Jets Using X-ray Diffraction. In *8<sup>th</sup> International Symposium on Ballistics*, 1984.
- [18] P.C. Chou, J. Carleone, and R.R. Karpp. Criteria for Jet Formation from Impinging Shells and Plates. *Journal of Applied Physics*, **47** : pp 2975–2981, 1976.
- [19] N.F. Mott. Fragmentation of Shell Cases. *Proceedings of the Royal Society, London, Series A*, **189** : pp 300–308, 1947.

- [20] E. Hirsch. A Formula for the Shaped Charge Jet Break-up Time. *Propellants, Explosives and Pyrotechnics*, **4** : pp 89–94, 1979.
- [21] E. Hirsch. A Model Explaining the Rule for Calculating the Break-up Time of Homogeneous Ductile Metals. *Propellants, Explosives and Pyrotechnics*, **6** : pp 11–14, 1981.
- [22] B. Haudstad. On the Break-up of Shaped Charge Jets. *Propellants, Explosives and Pyrotechnics*, **8** : pp 119–120, 1983.
- [23] J. Brown, P.A.F. Callow, M.C. Rogers, and G.C. Merritt. The Modelling of Crater Geometry Caused by Shaped Charge Jet Penetration into a Homogeneous Target. In *10<sup>th</sup> International Symposium on Ballistics*, 1988.
- [24] D.C. Pack and W.M. Evans. Penetration of High Velocity Jets. *Proceedings of the Royal Society, London, Series B*, **64** : pp 298–310, 1951.
- [25] R.J. Eichelberger. Experimental Test of the Theory of Penetration by Metallic Jets. *Journal of Applied Physics*, **27** : pp 63–68, 1956.
- [26] C.E. Anderson. An Overview of the Theory of Hydrocodes. *International Journal of Impact Engineering*, **5** : pp 33–59, 1987.
- [27] J.H. Hollomon. The Mechanical Equation of State. *Transactions AIME*, pages 535–545, 1946.
- [28] G.R. Johnson and W.H. Cook. A Constitutive Model and Data for Metals Subject to Large Strain Rates and High Temperatures. In *Proceedings 7<sup>th</sup> International Symposium on Ballistics*, pages 541–547, 1983.
- [29] H.R. Lips, H.P. Weisshaupt, and T.W. Niemeyer. Dynamic Behaviour and Properties of Heavy Metals. Rheinmetall GmbH.
- [30] P.C. Chou, J. Carleone, C.A. Tanzio, and R.D. Ciccarelli. Shaped Charge Break-up Studies Using Radiograph Measurements and Surface Instability Calculations. Technical report, Ballistics Research Laboratory, 1977. Report 337, AD A040444.
- [31] P.C. Chou and J. Carleone. The Stability of Shaped Charge Jets. *Journal of Applied Physics*, **48** : pp 4187–4195, 1977.

- [32] P.C. Chou and J. Carleone. The Effect of Compressibility on the Formation of Shaped Charge Jets. In *1<sup>st</sup> International Symposium on Ballistics*, 1983.
- [33] C.W. Miller. A new Approach to the Numerical Analysis of Shaped Charge Jets. In *Proceedings 6<sup>th</sup> International Symposium on Ballistics*, 1983.
- [34] M.F. Ashby. Fracture Mechanism Maps. *Acta Metallurgica*, **20** : pp 887–897, 1972.
- [35] A.H. Chokshi and M.A. Meyers. The Prospects for Superplasticity at High Strain Rates: Preliminary Considerations and an Example. *Scripta Metallurgica et Materialia*, **24** : pp 605–610, 1990.
- [36] J. Pilling and N. Ridley. *Superplasticity in Crystalline Solids*. The Institute of Metals, 1989.
- [37] K.S. Vecchio and R.W. Hertzberg. The Influence of Stacking Fault Energy on Ductile Fracture Micromorphology. *Journal of Materials Research*, **6** : pp 2220–2224, 1988.
- [38] G.E. Dieter. *Mechanical Metallurgy*, chapter 4, page 137. McGraw Hill, 1988.
- [39] G.E. Dieter. Metallurgical Effects of High Intensity Shock Waves in Metals. In P.G. Shewmon and V.F. Zackay, editors, *Response of Metals to High Velocity Deformation*, pages 409–443. Interscience Publications N.Y, 1960.
- [40] A.H. Holtzman and G.R. Cowan. The Strengthening of Austenitic Manganese Steel by Plane Shock Waves. In P.G. Sherwood and V.F. Zackay, editors, *Response of Metals to High Velocity Deformation*, pages 447–483. Interscience Publications N.Y, 1960.
- [41] B. Derby and M.F. Ashby. On Dynamic Recrystallisation. *Scripta Metallurgica*, **21** : pp 879–884, 1987.
- [42] H. Kolsky. An Investigation of the Mechanical Properties of Metals at Very High Rates of Loading. *Proceedings of the Physical Society*, **62B** : pp 676–700, 1949.

- [43] J.E. Field, G.M. Swallowe, and S.N. Heavens. Ignition Mechanisms of Explosives During Mechanical Deformation. *Proceedings of the Royal Society, London, Series A*, **382** : pp 231–244, 1982.
- [44] T.Z. Blazinski. *Materials at High Strain Rates*. Elsevier Applied Science, 1987.
- [45] J. Harding. *The Effect of High Strain Rate on Material Properties*, chapter 4, pages 133–186. Elsevier Applied Science, 1987.
- [46] C.S. Smith and C.M. Fowler. Further Metallographic Studies on Metals After Explosive Shock. In P.G. Sherwood and V.F. Zackay, editors, *Response of Metals to High Velocity Deformation*. Interscience Publications N.Y, 1960.
- [47] Q. Johnson and A.C. Mitchell. First X-ray Diffraction Evidence for a Phase Transition During Shock Wave Compression. *Physical Review*, **29** : pp 1369–1371, 1971.
- [48] G.A. Hayes and T.L. Herling. Optical Metallography of Linear Shaped Charge Fragments. Technical Report Report AD 878 080, Naval Weapons Centre, China Lake, California, 1970.
- [49] L. Zernow. Recovery of Shaped Charge Jet Samples for X-ray Diffraction Studies. In *Proceedings 10<sup>th</sup> International Symposium on Ballistics*, 1987. Zernow Technical Services Inc. 425, Bonita Avenue, San Dimas, CA91773.
- [50] L. Zernow. New Results from the Examination of Shaped Charge Jet Particles Captured by Soft Recovery, III. In *Proceedings 11<sup>th</sup> International Symposium on Ballistics*, 1989. Zernow Technical Services Inc. 425, Bonita Avenue, San Dimas, CA91773.
- [51] L. Zernow. Metallurgical, X-ray Diffraction and SEM Studies of Individual Shaped Charge Jet Particles Captured by Soft Recovery. II. In *International Conference on Ballistics, Nanjing, Peoples Republic of China*, 1988. Zernow Technical Services Inc. 425, Bonita Avenue, San Dimas, CA91773.
- [52] R.E. Green. First X-ray Diffraction Photograph of a Shaped Charge Jet. *Review of Scientific Instruments*, **46** (Nö 9) : pp 1257–1261, 1975.

- [53] R.E. Green. Portable Flash X-ray Diffraction System. *Review of Scientific Instruments*, **48** (Nö 4) : pp 425–426, 1977.
- [54] F.M. Charbonnier. Flash X-ray System for X-ray Diffraction with Submicrosecond Exposure Time. *Advances in X-ray Analysis*, **15** : pp 446–461, 1973.
- [55] J.A. Danzig and R.E. Green. Flash X-ray Diffraction Systems. In *Advances in X-Ray Analysis*, pages 229–241. Plenum Press, 1973.
- [56] K. Riefsnider and R.E. Green. Image Intensifier System for Dynamic X-ray Diffraction Studies. *Review of Scientific Instruments*, **39** : pp 1651–1655, 1968.
- [57] R.E. Green. Electro - Optical Systems for Dynamic Display of X-ray Diffraction Images. *Advances in X-ray Analysis*, **14** : pp 311–337, 1971.
- [58] F. Jamet and G. Thomer. X-ray Powder Patterns of Shaped Charge Jets. *CR. ACAD. Science, Paris, Series B*, **279** : pp 501–547, 1974.
- [59] S.K. Schiferl. Texture and Textural Evolution in Explosively Formed Jets. *Journal of Applied Physics*, **66** (Nö 6) : pp 2637–2650, 1989.
- [60] J. Wisotzki. Funnel Shaped or Shell Shaped Insert for Hollow Charges and a Process and a Mould for Producing it, 1989. Certificate of Grant of Patent.
- [61] A. Lichtenberger. Some Criteria for the Choice of Shaped Charge Copper Lines. In *Proceedings 11<sup>th</sup> International Symposium on Ballistics*, volume **2**, 1989.
- [62] British Standards Institution. BS L168, Bars and Extruded Sections of Aluminium - Copper - Magnesium - silicon - manganese alloy, 1978.
- [63] L.F. Mondolfo. *Aluminium Alloys: Structure and Properties*, page 316. Butterworths, 1976.
- [64] R.W.K. Honeycombe. *The Plastic Deformation of Metals*. Arnold, 1984.

- [65] B. Bourne. Liner Microstructure; its Effect on Shaped Charge Penetration Performance. Technical report, RARDE, 1988.
- [66] G.E. Dieter. *Ductility*, chapter 1, page 20. American Society for Metals, 1967.
- [67] R.P. Carreker and W.R. Hibbard. Tensile Deformation of Aluminium as a Function of Temperature, Strain Rate, and Grain Size. *Transactions AIME*, pages 1157–1163, 1957.
- [68] M Hansen. *Constitution of Binary Alloys 2<sup>nd</sup> Edition*. McGraw Hill, 1958.